

Diss. ETH No. 16521

# **Multidimensional Modeling and Simulation of Wavelength-Tunable Semiconductor Lasers**

A dissertation submitted to the  
SWISS FEDERAL INSTITUTE OF TECHNOLOGY  
ZURICH

for the degree of  
Doctor of Sciences

presented by  
LUTZ SCHNEIDER

Dipl.-Phys. ETH  
born 20.04.1974  
citizen of Germany

accepted on the recommendation of  
Prof. Dr. B. Witzigmann, examiner  
Prof. Dr. M.-C. Amann, co-examiner

2006

Seite Leer /  
Blank leaf

Seite Leer /  
Blank leaf

Seite Leer /  
Blank leaf



# Contents

<b>Acknowledgments</b>	<b>xiii</b>
<b>Abstract</b>	<b>xv</b>
<b>Zusammenfassung</b>	<b>xvii</b>
<b>1 Introduction</b>	<b>1</b>
1.1 Applications and Device Designs . . . . .	3
1.2 Scope . . . . .	10
1.3 Contents . . . . .	11
<b>2 Physical Model Equations</b>	<b>13</b>
2.1 Introduction . . . . .	13
2.2 Electrothermal Model . . . . .	14
2.3 Optical Model . . . . .	18
2.4 Opportunities and Limitations of 3D Model . . . . .	27
<b>3 Numerical Implementation</b>	<b>31</b>
3.1 Introduction . . . . .	31
3.2 Discretization and Solution Methods . . . . .	32

3.2.1	Electrothermal System . . . . .	32
3.2.2	Optics . . . . .	37
3.3	Coupling Scheme . . . . .	43
3.4	Problem-Specific Adjustments . . . . .	46
<b>4</b>	<b>Simulation Examples and Calibration</b>	<b>51</b>
4.1	Overview . . . . .	51
4.2	Tunable Twin-Guide DFB Laser . . . . .	52
4.2.1	Introduction . . . . .	53
4.2.2	Tuning Range versus Output Power . . . . .	54
4.2.3	Power Optimization . . . . .	56
4.2.4	Discussion . . . . .	58
4.2.5	Simulation Statistics . . . . .	63
4.3	Three-Section DBR Laser . . . . .	64
4.3.1	Introduction . . . . .	64
4.3.2	Calibrated Electrothermo-Optical Simulation . . . . .	64
4.3.3	Wavelength Tuning and Thermal Analysis in 3D . . . . .	66
4.3.4	Simulation Statistics . . . . .	77
4.4	Widely Tunable Sampled-Grating DBR Laser . . . . .	86
4.4.1	Introduction . . . . .	86
4.4.2	Three-Dimensional Simulation of Wavelength Tuning Characteristics . . . . .	89
4.4.3	Simulation Statistics . . . . .	99
4.5	A Guide to 3D Laser Simulation . . . . .	101
<b>5</b>	<b>Conclusion and Outlook</b>	<b>107</b>
5.1	Major Achievements . . . . .	107
5.2	Further Opportunities and Outlook . . . . .	108
<b>A</b>	<b>Command File Excerpts</b>	<b>109</b>

<i>CONTENTS</i>	vii
<b>List of Abbreviations</b>	<b>115</b>
<b>Bibliography</b>	<b>118</b>
<b>Curriculum Vitæ</b>	<b>131</b>

Seite Leer /  
Blank leaf

# List of Figures

1.1	Illustration of Basic Tuning Mechanism . . . . .	5
1.2	SEM of TTG DFB Laser . . . . .	7
1.3	SEM of SGDBR and DSDBR Laser . . . . .	8
2.1	Schematic of an Integrated SOA and SGDBR Laser . . . . .	21
2.2	Illustration of Separation Ansatz for 3D Optics . . . . .	23
2.3	3D Optical Intensity Distribution of a PBH SGDBR Laser . . . . .	24
3.1	Simulation Time of Iterative Linear Solver . . . . .	38
3.2	Iteration Analysis of Iterative Linear Solver . . . . .	39
3.3	Flowchart of 3D Optics Solver . . . . .	44
3.4	Simulation Flow for a Self-Consistent 3D Simulation . . . . .	45
4.1	Schematic Cross-Section of TTG Laser . . . . .	53
4.2	Output Power vs. Current Characteristics of TTG Laser . . . . .	56
4.3	Wavelength Tuning Characteristics of TTG Laser . . . . .	57
4.4	Current Streamtraces for two Different TTG Lasers . . . . .	59
4.5	LI Characteristics of BBR TTG Lasers . . . . .	60
4.6	Optical Near-Field of BBR TTG Laser . . . . .	61
4.7	Optical Far-Field of BBR TTG Laser . . . . .	62
4.8	Auger Recombination along Vertical Cut through TTG Laser . . . . .	62
4.9	Simulation Mesh of BBR TTG Laser . . . . .	63
4.10	Cross-Sectional Views of Three-Section DBR Laser. . . . .	65
4.11	Simulated versus Measured LI Characteristic . . . . .	67
4.12	LI Characteristics at Different Ambient Temperatures . . . . .	68
4.13	VI and LI Characteristics from 3D Simulation of DBR Laser . . . . .	71
4.14	Discontinuous Wavelength Tuning Behavior of DBR Laser . . . . .	72

4.15	Continuous Tuning Scheme of Three-Section DBR Laser . . .	73
4.16	Optical Intensity and Current Density of DBR Laser (Zoom)	74
4.17	Optical Intensity and Current Density of DBR Laser . . . . .	78
4.18	Temperature Distribution of DBR Laser . . . . .	79
4.19	Longitudinal Temperature Profile of DBR Laser . . . . .	80
4.20	Recombination Heat of DBR Laser . . . . .	81
4.21	Transverse Temperature Profile of DBR Laser . . . . .	82
4.22	2D Simulation Mesh of DBR Laser . . . . .	83
4.23	Extended 2D Simulation Mesh of DBR Laser . . . . .	84
4.24	Statistics for 3D Simulation Mesh of DBR Laser . . . . .	85
4.25	Schematic Illustration of SGDBR Laser Integrated with SOA .	87
4.26	Mode Pattern of SGDBR Laser Integrated with SOA . . . . .	87
4.27	Reflectivity Spectra of an SGDBR Laser . . . . .	90
4.28	Reflectivity and Resonance Spectra of an SGDBR Laser . . .	91
4.29	Simulated VI and LI Characteristics of SGDBR Laser . . . . .	92
4.30	Simulated Wavelength Tuning Map of SGDBR Laser . . . . .	93
4.31	Measured Wavelength Tuning Map of SGDBR Laser . . . . .	94
4.32	Facet Output Power of SGDBR Laser . . . . .	96
4.33	Optical Mode Loss of SGDBR Laser . . . . .	97
4.34	Active Section Voltage of SGDBR Laser . . . . .	98
4.35	Longitudinal Spatial Hole-Burning of SGDBR Laser . . . . .	98
4.36	Lateral Spatial Hole Burning of SGDBR Laser . . . . .	99
4.37	3D Simulation Mesh of SGDBR Laser . . . . .	100
4.38	3D Simulation Tool Flow . . . . .	105

# List of Tables

1.1	Comparison of Tunable Laser Diodes . . . . .	10
4.1	Simulation Parameters of TTG DFB Laser . . . . .	55
4.2	Simulation Statistics of Three-Section DBR Laser . . . . .	82
4.3	Epitaxial Layer Structure of SGDBR Laser . . . . .	88
4.4	Grating Specification of SGDBR Laser . . . . .	88

Seite Leer /  
Blank leaf



# Acknowledgments

First of all, I would like to thank Prof. B. Witzigmann for taking over the supervision of this work at an advanced stage and for supporting me during this crucial time. Furthermore, I am indebted to Prof. W. Fichtner for having given me the opportunity to carry out this thesis at his institute. His guidance and encouragement for a research visit to the University of California in Santa Barbara (UCSB) have been invaluable. Much appreciation to both of them for a smooth transition after Prof. Fichtner took up his position at Synopsys, Inc. Special thanks go to Prof. M.-C. Amann for accepting to be the co-examiner of this thesis and for carefully reviewing the manuscript.

I would like to thank Ch. Schuster for introducing me to the Integrated Systems Laboratory (IIS) and A. Witzig, whose enthusiasm and great spirit have been very motivating, for leading the optoelectronics modeling group. I am also particularly thankful to M. Pfeiffer and M. Streiff for their continuous support and friendship over the years.

The opto group has been a truly special team to work with. Special mention to B. Jacob, V. Laino, M. Luisier, S. Odermatt, and F. Geelhaar, all of who joined the team later on, for their valuable input and for contributing to its pleasant working atmosphere. Thanks also to S. Brugger for sharing his office and the good vibes during endless hours of thesis writing.

Furthermore, I am indebted to S. Rölli, B. Schmithüsen, J. Krause, G. Kiralyfalvi, and P. Regli for providing me with essential features regarding linear solvers and 3D meshing and interpolation. Great thanks to D. Polimeni for her meticulous proofreading of the manuscript.

I would like to thank Prof. J. Piprek for inviting me to St. Barbara for a research visit to the University of California. This stay has been very important to me both academically and personally. Thanks to all of the people who have supported me during this period.

Last but not least, I wish to thank the administrative, computer, and technical staff of IIS for having provided an excellent and friendly working environment.

# Abstract

Wavelength-tunable semiconductor lasers play an important role in agile optical networks, which offer unrivaled reconfigurability, scalability and robustness at the optical layer. This dissertation presents a multidimensional simulation approach for tunable edge-emitting lasers with a focus on modeling in full three dimensions.

Most monolithic tunable lasers are multisection devices. Taking into account their three-dimensional nature and their increasingly complex operation, the state-of-the-art commercial device simulator DESSIS has been extended to accommodate the simulation of these lasers. To this end, an efficient three-dimensional optical mode solver has been implemented. Optical field and lasing wavelength are obtained by a parametric separation ansatz, which requires the calculation of several local normal modes along the waveguide and the solution of a longitudinal cavity problem. A thermodynamic model accounting for device self-heating describes carrier transport in bulk semiconductor regions, including longitudinal current flux in full three dimensions. For transport across heterointerfaces, thermionic emission processes are assumed, whereas active quantum-well regions are represented as scattering centers for electrons and holes. Following a rate equation approach, self-consistent coupling between the electrothermal system and optics is achieved. The resulting system of nonlinear equations is solved using a Newton–Raphson scheme.

This thesis discusses three different types of tunable laser in detail: A twin-guide DFB laser, a three-section buried-heterostructure DBR laser and a ridge-waveguide sampled-grating DBR laser are simulated and compared to measurements. The latter, belonging to the new generation of widely tunable lasers, necessitated a modified numerical coupling approach to handle the characteristic discrete mode jumps observed in their tuning maps.

Further implementations concern performance improvements showing that fully coupled, electrothermo-optical simulations in three dimensions meet the requirements of device engineers. All necessary steps for performing a successful simulation, including structure generation and advanced meshing, are covered in this work.

The general formulation of the model and its implementation in the simulator make it suitable for a wide range of other monolithically integrated tunable lasers. In addition, the capabilities of the simulator can be extended by using advanced models recently developed at the Integrated Systems Laboratory (IIS) of the Swiss Federal Institute of Technology (ETH) in Zürich. These include  $k \cdot p$  band structure and manybody gain calculation as well as the extraction of dynamic and noise properties.

# Zusammenfassung

Wellenlängen-abstimbare Halbleiterlaser spielen eine wichtige Rolle in wellenlängen-dynamischen optischen Netzwerken, welche eine unvergleichliche Rekonfigurierbarkeit, Skalierbarkeit und Robustheit auf optischer Ebene bieten. Die vorliegende Doktorarbeit präsentiert eine multidimensionale Herangehensweise zur Simulation von abstimbaren, kantenemittierenden Lasern und konzentriert sich dabei auf die Modellierung in drei räumlichen Dimensionen.

Die meisten monolithischen, abstimbaren Laser sind Bauelemente mit mehreren Abschnitten. Um die Simulation solcher Laser zu ermöglichen, wurde unter Berücksichtigung deren dreidimensionaler Natur sowie deren zunehmend komplizierteren Betriebsweise der kommerzielle Halbleiterbauelement-Simulator DESSIS erweitert. Dies bedurfte der Entwicklung und Implementation eines Verfahrens zur Berechnung der dreidimensionalen optischen Moden. Das optische Feld und die Wellenlänge des Laser werden über einen Separationsansatz ermittelt, der die Berechnung mehrerer lokaler, normierter Moden entlang des Wellenleiters und die Lösung eines longitudinalen Kavitätsproblems bedingt. Ein thermodynamisches Modell, welches Selbsterwärmung des Bauteils mit einbezieht, beschreibt den Ladungsträgertransport im Halbleiter einschliesslich des longitudinalen Stromflusses in drei Dimensionen. An Heteroübergängen wird der Transport mittels eines thermionischen Emissionsmodells abgebildet, während aktive Quantumwell-Regionen als Streuzentren für Elektronen und Löcher behandelt werden. Die selbstkonsistente Kopplung zwischen dem elektrothermischen System und der Optik wird durch einen Ratengleichungsansatz hergestellt. Das daraus folgende numerische System nichtlinearer Gleichungen wird mit einer Newton–Raphson Methode gelöst.

In dieser Arbeit werden drei verschiedene abstimmbare Lasertypen ausführlich behandelt: Dies beinhaltet die Simulation eines twin-guide DFB Laser, eines buried-heterostructure DBR Laser und eines sampled-grating DBR Laser mit einem Stegwellenleiter, und den Vergleich mit Messdaten. Der sampled-grating DBR Laser gehört zur neuen Generation der weit abstimmbaren Laser und bedurfte einer speziellen Herangehensweise. Ein abgewandeltes numerisches Kopplungsschema wurde entwickelt, um die Simulation der charakteristischen diskreten Modensprünge im Abstimmverhalten zu ermöglichen. Darüber hinaus wurden Entwicklungen vorgenommen, welche die Rechenleistung verbessern und so voll gekoppelte elektrothermo-optische Simulationen im industriellen Umfeld erlauben. Schliesslich werden auch noch die nötigen Schritte aufgezeigt, die bei der Durchführung einer erfolgreichen Simulation anfallen. Dazu zählen die Erstellung der Simulationsstruktur und die anspruchsvolle Gittergeneration.

Die allgemein ausgelegte Formulierung des Modells und dessen Implementierung im Simulator erlauben die Behandlung eines weiten Spektrums an monolithisch integrierten, abstimmbaren Lasern. Zusätzlich ist es möglich, die vorgenommenen Entwicklungen mit fortgeschrittenen Modellen zu kombinieren, welche kürzlich am Institut für Integrierte Systeme an der Eidgenössischen Technischen Hochschule in Zürich entstanden sind. Dazu gehören die  $k \cdot p$  Bandstrukturberechnung, die Berücksichtigung von Vielteilcheneffekten bei der Verstärkungsberechnung und die Möglichkeit, dynamische Eigenschaften sowie das Rauschverhalten eines Laser zu extrahieren.

# Chapter 1

## Introduction

Wavelength-tunable (WT) lasers have an immense impact on science, technology and industry. They boast a wide range of applications in fundamental research and applied fields that extend from atom cooling in Bose-Einstein condensation experiments over wavelength-division multiplexing systems to materials processing. However, no single WT laser can match every application's specific demands on performance. As a consequence there are numerous embodiments of this type of laser with respect to both the underlying gain medium and the tuning mechanism [1].

From a commercial perspective, semiconductor lasers—invented in the early 1960s—have come to play a dominant role today: They hold the biggest share of the total US\$70 billion world market for lasers and laser systems<sup>1</sup>. Due to a number of attractive features such as compact size, wallplug efficiency, wavelength range, reliability, and low cost, laser diodes have replaced other types of laser as well as sparked new applications. One of the most prominent examples of the latter is the compact disc player.

The large gain bandwidth of most laser diodes makes them ideal candidates for applications demanding wavelength tunability. Furthermore, they allow for monolithic integration not only of the tuning mechanism but also of other functions such as amplification, modulation and optical mode tapering. This integration effort has led to one of the first commercially available, small-scale photonic integrated circuits (PICs) [2, 3, 4] and has been a mile-

---

<sup>1</sup>Source: Optech Consulting, Laser Market Data, March 2005, <http://www.optech-consulting.com>.

stone on the way to large-scale PICs [5]. However, increasing functionality often comes at the expense of more complex fabrication and characterization methods. Laboratory prototypes of distributed Bragg reflector (DBR) lasers, which form the foundation of many present monolithic tunable laser diodes, were demonstrated in the early 1980s [6, 7], but it took more than a decade before they were commercially deployed.<sup>2</sup>

Several challenges in the fields of performance, manufacturing, packaging, control systems and testing have to be overcome before a specific device structure can go into volume manufacturing. This is a time-consuming and costly process, which plays an important role in the competitiveness of tunable laser diode manufacturers. As the optical telecommunications industry—the main driving force behind the development of tunable lasers in need of higher transmission capacity—has suffered from an economic downturn in the past few years (after the height of the telecommunications boom in 2000), increasing the efficiency of the development cycle has become even more crucial.

Technology computer-aided design (TCAD), a standard in the design and optimization of silicon-based microelectronics for many years, has the potential to play a similar role in III–V optoelectronics. Predictive modeling tools can replace expensive design trials in the laboratory and, hence, can speed up the time-to-market of new products while reducing overall development cost. This is an important factor for the new generation of widely tunable semiconductor lasers in particular, whose complex device structure compared to Fabry–Perot (FP) lasers gives rise to more degrees of freedom in the design and requires sophisticated device management. Economic reasons are also responsible for the move to an outsourced manufacturing model in the past few years, since the amount of revenue available to individual companies will often not allow for profitable support of an internal fabrication facility. For many specialized devices, there is no high-volume market available, in which economies of scale could apply.

The concept of a fabless design-house is starting to gain momentum also in the III–V optoelectronics industry as progress has been made in two important areas: maturing fabrication processes and technology in well-established material systems such as InGaAsP/InP and better simulation software. The latter is crucial not only in the design of an initial prototype promising to fulfill the set performance goals, but also in the investigation

---

<sup>2</sup>For a good review of the history of monolithic tunable laser diodes, see [8].



of fabrication tolerances, device lifetime and reliability. Traditionally, the focus of academic and commercial software development has been on the prototype design. However, the other factors are, at least, as important in determining the commercial success of a specific device. A promising approach in this field consists of integrating a predictive, physics-based device simulator into a statistical analysis environment [9]. The result is the need for a calibrated and efficient (fast) simulator, which can reliably span the high-dimensional parameter space.

## 1.1 Applications and Device Designs

### Applications

Wavelength-tunable (WT) laser diodes can be grouped into three major application areas [10]: optical communications, sensing and measurement. Among these, optical communications plays a prominent role, even though the economic slowdown in this area has prompted WT laser companies to increasingly target applications in the other two areas as well. Examples of the former are wavelength-division multiplexing (WDM), coherent optical communication and wavelength reference.

In a WDM system, incoming optical signals are assigned to specific wavelengths of light within a certain wavelength range, usually the ITU C-band and L-band (1530–1565nm and 1565–1625nm), and are sent simultaneously through a singlemode fiber. On the receiving end, the signals are demultiplexed. Thus, the transmission capacity of a fiber can be increased by a factor depending on the wavelength channel spacing. Dense wavelength-division multiplexing (DWDM)—a further development of WDM—spaces the wavelengths more closely and, consequently, reaches a greater capacity in addition to having other attractive features.

WT lasers can be a cost-effective alternative to single-wavelength lasers in WDM systems. In a DWDM network with 50GHz channel spacing, corresponding to a wavelength spacing of 0.4nm, 100 channels within a waveband of 40nm width are designated by the standard ITU wavelength grid. A growing channel count, for example, by a factor of five compared to coarse wavelength-division multiplexing (CWDM) networks also comes with an increase of cost for buying, storing, and managing spares for the system. Hence, the potential savings when employing WT lasers covering several

channels, instead of fixed-wavelength lasers, are evident. On the other hand, besides their tunability, WT lasers are required to meet the stringent demands of standard DFB lasers, which generally results in greater unit cost. Among these are wavelength stability to within  $\pm 5\%$  of the channel spacing, side-mode suppression ratio (SMSR), and output power uniformity across the entire tuning range.

Whereas cost advantages from reducing inventory are an important selling factor in the telecom area in the short-term and mid-term, the more exciting potential applications lie in the future: They extend from one-time and dynamic provisioning over reconfigurable optical add/drop multiplexers (ROADMs) and optical cross-connects to dynamic restoration, wavelength routing and optical packet switching. In a wavelength-routed network using fixed cross-connects, for example, each wavelength connects to a unique network destination, thereby replacing complicated and costly all-optical switches. Wavelength routing is widely assumed to be the future of optical networking.

## Basic Tuning Mechanisms

The wavelength of a semiconductor laser can be tuned either electronically, thermally, micro-electro-mechanically,<sup>3</sup> or by a combination of these three mechanisms. Although electronic and thermal tuning are both based on changing the effective index of refraction seen by the cavity mode, the former is in general preferred due its inherent faster response by at least several orders of magnitude. Micromechanical tuning is characteristic of external cavity lasers (ECLs), in which external elements such as diffraction gratings or etalons are used as wavelength filters.

Tunable ECLs separate the wavelength selection and tuning from the gain medium. In this aspect, they represent the ideal WT laser, whose laser characteristics, especially output power, should not suffer from tuning operation. Another desired and sometimes essential feature is continuous or at least quasi-continuous singlemode tunability across a maximum wavelength interval using a minimum number of control currents. However, in practice, there is always a trade-off among these properties.

---

<sup>3</sup>In this enumeration, it is referred to the primary tuning characteristic/dependence. In practical applications, all wavelength filters are in some way controlled electronically and unwanted thermal effects can influence the tuning behavior.

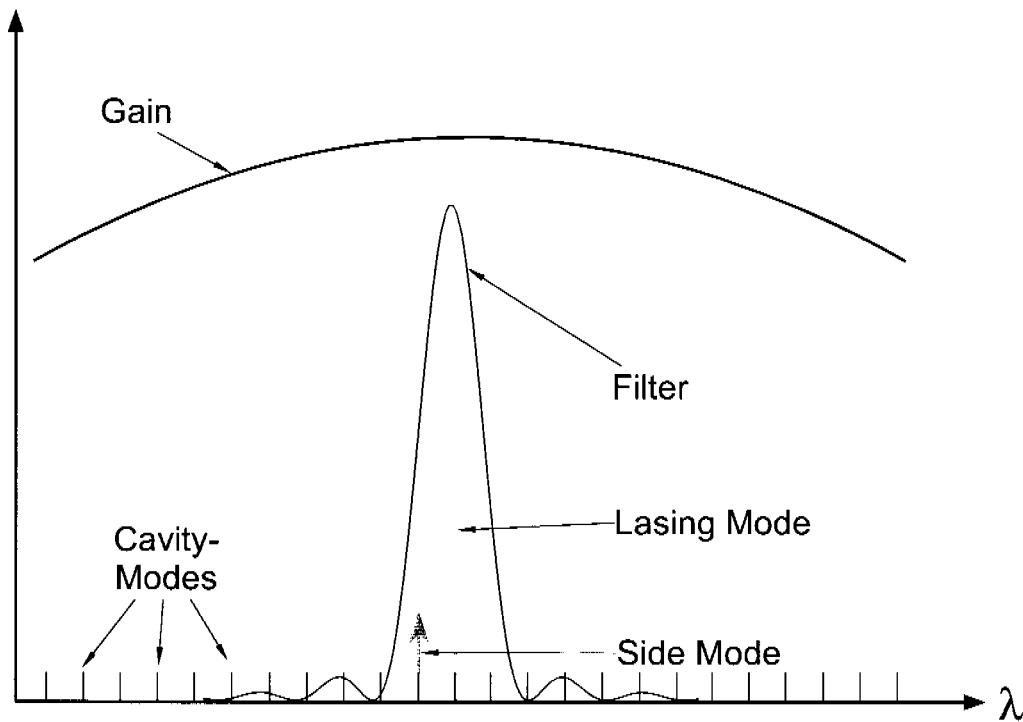


**Figure 1.1:** Illustration of the interplay among the various spectra governing the tuning behavior of a laser.

The tuning behavior is determined by the interplay of the cavity-mode and gain spectra, and the mode-selection filter spectrum as illustrated in Fig. 1.1. The comb-like cavity-mode spectrum is given by the effective cavity length and often a separately controllable element is used to fine-tune the positions of the cavity modes with respect to the main maximum of the filter spectrum. In monolithically integrated WT lasers, the filter usually consists of a grating structure, which can be located either in a single section, as in DFB or three-section DBR lasers, or in two sections, as in sampled-grating distributed Bragg reflector (SGDBR) or grating-coupled sampled-reflector (GCSR) lasers. An electronically or a thermally induced change in the effective refractive index moves the filter spectrum along the wavelength axis. If two grating sections are present, the product of the spectra that are shifted relative to each other characterizes the filter function. Simultaneously shifting the different spectra, it is possible to achieve continuous tunability. In all other cases, mode jumps can occur, which lead to quasi-continuous or discontinuous tuning regimes. In the picture of a FP laser, the

grating regions can be seen as wavelength-selective effective mirrors.

Another approach for realizing a tunable laser source in the broader sense is the concept of laser arrays: Several narrow-band tunable lasers are arranged side-by-side, where each laser addresses a small wavelength range within a wider total band. Together with an integrated combiner element, it is also possible to have a single output channel.

## Overview of Device Designs

In the following, an overview of monolithically integrated WT laser diodes is given. The focus is on laser devices that have a medium to wide tuning range of 10nm—100nm. For an exhaustive treatment of tunable laser diodes, the reader is referred to the literature [10, 11].

The **tunable twin-guide (TTG) DFB laser** represents a transversely integrated structure, in which the active and tuning region are separated by a thin layer as shown in Fig. 1.2. A DFB grating formed in the tuning region ensures single-longitudinal-mode operation, and a common lateral contact allows for independent control of laser and tuning current [12]. Whereas DFB lasers are in general narrow-band sources, the specific design of the TTG DFB, along with several optimizations [13, 14], have led to a maximum continuous tuning range and output power of  $\sim 10$ nm and  $\sim 20$ mW, respectively. This structure is discussed in detail in Section 4.2.

By combining the TTG design with the advantages of sampled gratings, the authors of [15] have shown that it is possible to extend the tuning range by a factor of up to three. At the same time, the tuning control is simplified compared with other sampled-grating or superstructure-grating DBR lasers to be discussed here.

The **vertically integrated Mach–Zehnder (VMZ) laser** is a further example of a widely tunable source that contains two vertically separated waveguides, yet, of different length. In contrast to the TTG, the thickness of the spacer layer is of the same order of magnitude as the waveguide layers, and the tuning behavior is determined by the interference between two modes, of which one has most of its power in the top waveguide and the other in the bottom waveguide [16, 17].

The **distributed Bragg reflector (DBR) laser** is the simplest, longitudinally integrated structure with a maximum tuning range of  $\sim 15$ nm [7, 18]. It is also the basis for more sophisticated wide-band tunable lasers, which have been developed in the last decade [19]. A typical DBR laser that al-

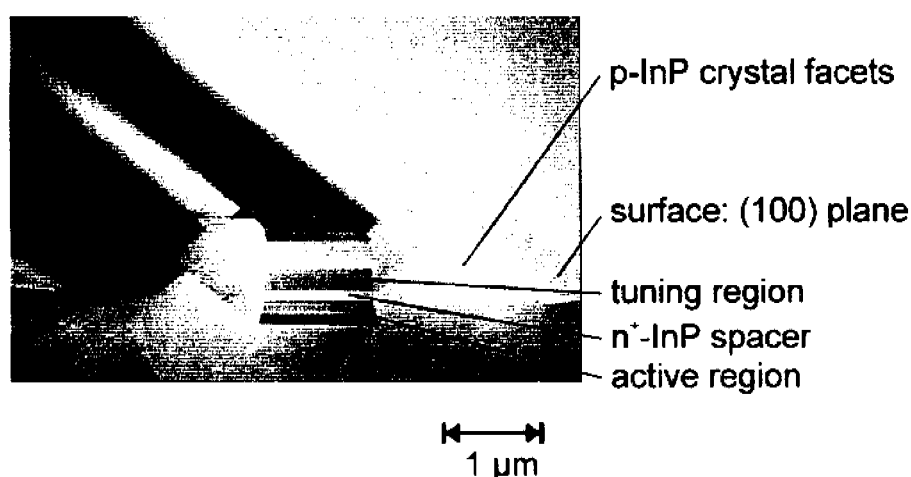


**Figure 1.2:** Scanning electron micrograph of the TTG ridge structure indicating the vertical separation of the active and tuning region [13].

lows for quasi-continuous tuning consists of three sections: a gain region at the front, a phase-control region and a DBR grating region at the rear. By injecting current into the phase region, the effective cavity length changes. In this way, it is possible to align a cavity mode with the Bragg peak while the Bragg spectrum is shifted. This tuning scheme requires a calibrated control system and its accessible wavelength range is limited by the maximum change in carrier density in the grating section, which saturates at increasing injection current. The three-section DBR laser is discussed in Section 4.3.

The **sampled-grating distributed Bragg reflector (SGDBR) laser** is a representative of the class of widely tunable lasers [20]. It overcomes the limitation to the tuning range, which results from the maximum possible index change in any one section, by employing a so-called sampled grating (SG) at each end of the cavity. SGs are different from DBR gratings in that the grating is blanked periodically along its axis, leading to several equally spaced reflection peaks. The product of two mirror reflection combs, with slightly different mirror peak spacing, determines the filter properties. As these reflection combs can be tuned independently, a wavelength interval of 50-100nm can be accessed [21]. It should be noted that with this technique a relatively small index change in one section can lead to a comparatively large wavelength jump<sup>4</sup>.

Similar to the DBR laser, a phase-control section is required to achieve

<sup>4</sup>In the literature, this is often associated with the vernier effect.

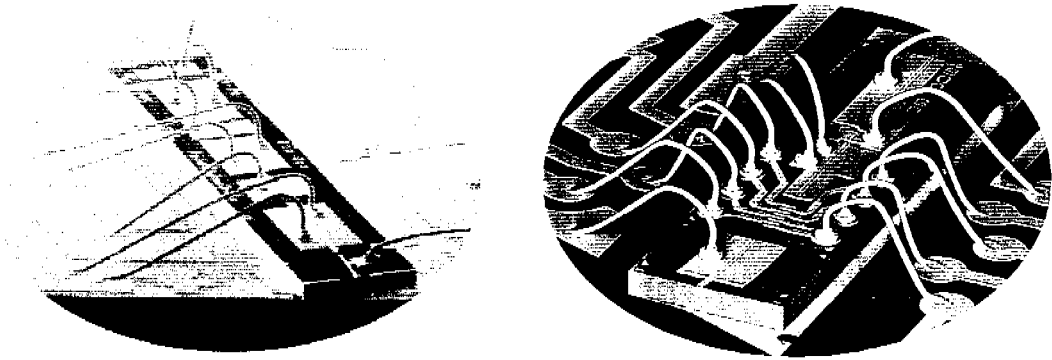


**Figure 1.3:** Scanning electron micrograph of SGDBR laser (left) and DSDBR laser(right) both integrated monolithically with a semiconductor optical amplifier [19, 22]. The difference in design between these devices is illustrated by the single-contacted sampled grating on the left and the multi-contacted front mirror grating on the right.

quasi-continuous tuning across the whole band. The output power of a SGDBR laser, which suffers from the grating mirror in front of the gain section, can be boosted by integrating it with a semiconductor optical amplifier (SOA) [21] as shown in Fig. 1.3. The SGDBR laser is investigated in Section 4.4.

**Superstructure-grating distributed Bragg reflector (SSGDBR) lasers** work on the same principle as SGDBR lasers, but generalize the concept of sampled gratings. An SSG is composed of several superperiods of, for example, a linearly or piecewise-constantly chirped grating and is intended to improve uniformity of the reflection peaks. As a result, the output power can, in principle, be kept at a similarly high level across the entire tuning range. Values from 40nm to 100nm have been reported for SSGDBR lasers [23, 24].

Replacing the front mirror grating of the SSGDBR laser with a multi-grating structure yields the **digital-supermode distributed Bragg reflector (DSDBR) laser**. A series of very short gratings of linearly varying pitches leads to a broad overall reflection spectrum composed of the corresponding Bragg peaks. Since each subgrating has its own electrical contact (see Fig. 1.3), two neighboring peaks can be aligned—a carrier-induced index change in a subgrating shifts the Bragg wavelength towards its shorter wavelength neighbor—to give a pronounced reflection peak. The filter wavelength is then determined by the narrow rear-mirror peak that coincides with

the front-mirror peak. With this design, the carrier induced loss in the front mirror can be reduced and kept nearly constant over the entire tuning range of  $\sim 50\text{nm}$  [25, 22] because the total injected current is independent of the selected subband.

Despite a different realization, the **grating-coupled sampled-reflector (GCSR) laser** is also based on the concept of a coarse tuner selecting one of the narrow rear-mirror reflection peaks only [26]. In this four-section device, a gain block in the front end is followed by a grating-assisted codirectional coupler, a phase-control section and sampled reflector, which can be either a sampled or superstructure grating. The coupler transfers power vertically between a waveguide ending with a sampled reflector and a waveguide extending through the gain block. Only at the coupling wavelength, whose tuning is proportional to the ratio of the index change and index difference of the coupled waveguides, the quality factor of the resonator that is formed between the facets is high enough to support laser action. A maximum tuning range of over  $100\text{nm}$  [27] and high output powers above  $20\text{mW}$  [28] have been reported for the GCSR laser.

The **modulated-grating Y-branch (MG-Y) laser** is another structure that relies on a coupler and does not require a grating section at the front, hence enabling output powers in excess of  $20\text{mW}$  over a tuning range of  $\sim 40\text{nm}$  [29]. Each of the two branches of the Y contains a modulated grating, whose comb-reflection spectra have a slightly different peak spacing. The maximum of the sum of these spectra—and not that of the product as in SGDBR or SSGDBR lasers—determines the filter wavelength. Again, a small index change in one of the branches can cause a large wavelength shift. To align the filter wavelength with a cavity mode, a phase-control section is placed between the gain section and the multimode interference coupler [30] that joins the separate waveguides.

A common configuration of a tunable **vertical-cavity surface-emitting laser (VCSEL)** uses an adjustable MEMS mirror on top of the device to change the effective cavity length [31]. Although the top mirror can be monolithically integrated in a single epitaxial growth process, such tunable VCSELs are sometimes also associated with the class of external cavity lasers. The output power and tuning range of such devices, if pumped electrically, are somewhat limited, especially for the  $1550\text{nm}$  wavelength range.

Table 1.1 compares several semiconductor laser types having a medium to wide tuning range with a focus on monolithically integrated structures. The TTG DFB laser, the three-section DBR laser and the SGDBR laser are

Laser type	Power >10mW	Maximum tuning range [nm]	Tuning speed	Monolithic integration
TTG DFB	yes	$\sim 10$	ns	yes
SG TTG	yes	$\sim 30$	ns	yes
DBR	yes	$\sim 15$	ns	yes
SGDBR	with SOA	50–100	ns	yes
SSGDBR	yes	40–100	ns	yes
DSDBR	with SOA	$\sim 50$	ns	yes
GCSR	yes	50–100	ns	yes
VMZ	yes <sup>5</sup>	$\sim 30$	ns	yes
MG-Y	yes	$> 40$	ns	yes
VCSEL	no <sup>6</sup>	30–50	$\sim 200\mu s$	yes
Ext. cavity	yes	$> 100$	$\geq 10ms$	no
DFB array	yes	15–30	$\sim 10ms$	no

**Table 1.1:** Comparison of several semiconductor laser structures having a medium to wide tuning range. The red laser types are discussed in detail in this work. Data is taken from [10] and other references of this section.

discussed in detail in this work.

## 1.2 Scope

The numerical modeling of multisection laser diodes has so far been restricted to one-dimensional longitudinal models or different two-dimensional transverse models, which either analyze the different cross sections separately or couple them in a circuit-like manner. Valuable information can be drawn from these models and their computational efficiency has been a strong argument for their use as a practical design tool [32, 33, 34]. Yet, with the advent of more sophisticated designs such as widely tunable semiconductor lasers with sampled or superstructure gratings, it is no longer possible to understand the device characteristics fully when reducing the

<sup>5</sup>Output power  $> 10mW$  is assumed but could not be verified with published results.

<sup>6</sup>Tunable VCSEL designs using optical instead of electrical pumping can reach output powers and tuning ranges greater than 10mW and 50nm, respectively.



system to one or two dimensions. The influence of leakage currents, spatial hole burning, thermal behavior and crosstalk effects, for example, cannot be accounted for accurately. Despite the fact that full three-dimensional simulations are still computationally expensive, their significance is bound to increase as the design-for-manufacturing (DFM) paradigm is gaining momentum in the optoelectronics industry. Eventually, process and device simulations will be closely linked and only three-dimensional simulations are able to account for the influence of arbitrary changes in the device geometry and doping profile.

The goal of this thesis is to extend the device simulator DESSIS to accommodate the efficient simulation of complex tunable lasers in full three dimensions with the same physical rigor that has been established in two dimensions. An approach is chosen that allows the user to apply the simulator to the widest possible range of tunable lasers and to make use of all other advanced features and models both present and future. Following a multidimensional simulation approach, several examples are given that demonstrate both the power and limitations of one-dimensional and two-dimensional laser simulation, hence, motivating the need to embark on advanced three-dimensional modeling.

A fully calibrated simulation in three dimensions is beyond the scope of this thesis; however, comparison with measurements is given to demonstrate the applicability of the implemented models and to verify the resulting characteristics. Since the corresponding simulation setup, including structure generation and meshing, as well as the numerics are considerably more involved than in lower dimensions, attention is also given to practical aspects of performing a successful simulation.

## 1.3 Contents

The thesis is organized as follows:

**Chapter 1: Introduction.** Physics-based device simulation in the context of tunable laser applications is motivated. The basic wavelength-tuning mechanisms are introduced along with an overview of the various device designs that have evolved from them. An outline of the goals sets the scope of this thesis.

**Chapter 2: Physical Model Equations.** The physical models underlying the presented laser device simulator are summarized. Special emphasis is given to the extension of the optical model to fulfill the requirements of full three-dimensional simulation of multisection tunable lasers. Electro-thermal transport and quantum-well physics are explained briefly. Opportunities and limitations of the 3D model in the area of tunable semiconductor lasers are discussed.

**Chapter 3: Numerical Implementation.** The numerical methods for solving the electrothermal and optical equations are presented. First, the solution methods for the electrothermal equations are presented including a performance analysis of the iterative linear solver used in three-dimensional simulations. Then, the constituents of the 3D optics solver and its coupling to the electrothermal system are highlighted. Finally, numerical challenges inherent to the simulation of tunable lasers are addressed.

**Chapter 4: Simulation Examples and Calibration.** Simulation results for three different types of tunable laser are compared to experimental data. The first example deals with the device optimization of a tunable twin-guide DFB laser, while the focus of the second is on the wavelength-tuning and thermal analysis of a three-section DBR laser in full three dimensions. An investigation of a widely tunable sampled-grating DBR laser concludes the series of examples. The remainder of the chapter is dedicated to practical aspects of 3D simulation of tunable lasers.

**Chapter 5: Conclusion and Outlook.** This thesis concludes with a summary of major achievements and suggests future developments by highlighting areas of further interest.

# Chapter 2

## Physical Model Equations

### 2.1 Introduction

The ideal optoelectronic device simulator would be able to describe the interaction between light and semiconductor materials within the framework of quantum electrodynamics in all three spatial dimensions and would require a typical simulation time of less than one day for a single device. This would allow not only the analysis and optimization of present-day devices, but also the prediction of new physical effects not yet observed in experiments. The study of a single quantum dot in a photonic crystal microcavity, for example, has been a step in this direction [35].

However, for most optoelectronic devices such an approach is neither necessary nor feasible. Consequently, several levels of approximation have been applied by researchers and developers of commercial simulation software. They extend from microscopic modeling of important subproblems over comprehensive device simulation to compact models of photonic integrated circuits (PICs).

#### **Tightrope Walk**

Taking into account the specific device geometry, the operating regime of interest and its dominant physical effects, a considerable reduction of model complexity with minimal loss of accuracy can be achieved. This is the tightrope walk that has to be faced when developing a physics-based and

accurate, yet, robust and fast device simulator that can serve the optoelectronics industry [36].

### **Model Extensions**

Wavelength-tunable (WT) semiconductor lasers are almost exclusively multisection devices or longitudinally varying structures (see Section 1.1). In contrast, the initial optoelectronic simulation capabilities of DESSIS [37]—a computer program originally designed for silicon device simulation [38, 39]—focused on the requirements of a Fabry–Perot (FP) edge-emitting laser (EEL) [40, 41]. However, the work of [42, 43] has shown the powerful concept of extending the simulator by building on a common base, despite the structural differences of a new class of device such as vertical-cavity surface-emitting lasers (VCSELs). This concept will also be adopted for the abovementioned class of tunable laser.

### **Outline**

In this chapter, the fundamental physical models are discussed that account for the increased complexity of a new class of device, as compared with standard FP lasers: multi-electrode laser diodes with various types of grating structures in the longitudinal direction. The challenge consists of finding a formulation that can treat physical effects on the nanoscale, such as quantum-well or quantum-dot active regions, and submicron spatial inhomogeneities on a millimeter-length scale in the same framework.

After a short review of the thermodynamic model implemented in DESSIS, a description will be given of how the optical model has been extended in this work to accommodate the analysis of the wavelength-tuning behavior in full 3D simulations. The chapter concludes with an assessment of the opportunities and limitations of this model in terms of applicability to different embodiments of tunable semiconductor lasers.

## **2.2 Electrothermal Model**

The electrothermal simulation models are only summarized briefly. They are based on the thermodynamic model derived in [44] and its implementation for silicon device simulation as given in [39]. Detailed descriptions of

the necessary extensions for the simulation of optoelectronic devices can be found in [45] and [36].

The basic equations of the thermodynamic model comprise the Poisson equation for the electrostatic potential  $\phi$ , the continuity equations for the electron and hole densities  $n$  and  $p$ , and the local heat flux  $\mathbf{S}$ ,

$$\nabla \cdot \epsilon \nabla \phi = -q (p - n + N_D^+ - N_A^-) \quad (2.1)$$

$$\nabla \cdot \mathbf{j}_n = q (R + \partial_t n) \quad (2.2)$$

$$-\nabla \cdot \mathbf{j}_p = q (R + \partial_t p) \quad (2.3)$$

$$\nabla \cdot \mathbf{S} = -c_{tot} \partial_t T - \nabla \cdot (\mathbf{j}_n (P_n T + \Phi_n) + \mathbf{j}_p (P_p T + \Phi_p)). \quad (2.4)$$

The electron and hole quasi-Fermi potentials  $\Phi_n$  and  $\Phi_p$  can be directly calculated from the electron and hole densities [45]. The variables  $N_D^+$  and  $N_A^-$  are the ionized donor and acceptor concentrations, respectively, and the recombination rate  $R$  is the sum of radiative and nonradiative recombination. The absolute thermoelectric powers for electrons and holes,  $P_n$  and  $P_p$ , are given by

$$P_n = -\frac{k_B}{q} \left( \frac{3}{2} + \ln \frac{N_C}{n} \right) \quad (2.5)$$

$$P_p = \frac{k_B}{q} \left( \frac{3}{2} + \ln \frac{N_V}{p} \right), \quad (2.6)$$

where  $N_C$  and  $N_V$  are the respective effective densities-of-states in the conduction and valence band. These are written as

$$N_C = 2 \left( \frac{k_B T m_e}{2\pi \hbar^2} \right)^{3/2} \quad (2.7)$$

$$N_V = 2 \left( \frac{k_B T m_h}{2\pi \hbar^2} \right)^{3/2}, \quad (2.8)$$

with the relative effective masses of electrons and holes denoted by  $m_e$  and  $m_h$ , respectively.

Further equations define the electric displacement  $\mathbf{D}$ , the current densi-

ties  $j_n$ ,  $j_p$ , and the heat flux  $S$

$$\mathbf{D} = \varepsilon \nabla \phi \quad (2.9)$$

$$\mathbf{j}_n = -q (\mu_n n \nabla \phi - D_n \nabla n + \mu_n n P_n \nabla T) \quad (2.10)$$

$$\mathbf{j}_p = -q (\mu_p p \nabla \phi + D_p \nabla p + \mu_p p P_p \nabla T) \quad (2.11)$$

$$\mathbf{S} = -\kappa_{th} \nabla T, \quad (2.12)$$

where  $T$  is the local temperature,  $\mu_n$  and  $\mu_p$  are the mobilities and  $D_n$ ,  $D_p$  are the diffusion constants.

The various contributions to the total carrier recombination rate  $R$  in Eqs. (2.2) and (2.3) are the spontaneous emission rate

$$R^{sp} = C_{sp}(np - n_i^2), \quad (2.13)$$

the Auger recombination rate

$$R^A = (C_n n + C_p p) (np - n_i^2), \quad (2.14)$$

and the Shockley–Read–Hall (SRH) recombination rate

$$R^{SRH} = \frac{np - n_i^2}{\tau_p(n + n_i) + \tau_n(p + n_i)}, \quad (2.15)$$

where  $n_i$  is the material-dependent intrinsic carrier density. More details on the models for the minority carrier lifetimes  $\tau_{n,p}$ , the Auger coefficients  $C_{n,p}$ , the spontaneous emission coefficient  $C_{sp}$  and in particular their temperature dependence can be found in [37].

For carrier transport across heterointerfaces due to concentration discontinuities, a thermionic emission model is used, which follows [46].

### Carrier Transport in Quantum-Well Active Regions

Since the majority of laser devices simulated in this work contains quantum-confined structures in its active region, the modeling of carrier transport in the presence of quantum wells is briefly addressed here. It is based on the distinction between so-called *mobile* three-dimensional charge carriers and *bound* charge carriers. The former species is assumed to traverse the wells ballistically, whereas the latter is confined to the surroundings of the well. At the edges of the quantum wells, boundary conditions for the electron and

hole current density components perpendicular to the quantum-well plane are applied according to [47]. The parallel components are assumed to be negligible.

The distribution of the bound charge carriers along the direction of quantization is given by the solution of Schrödinger's equation subject to the approximation of an effective-mass band-structure. In general, a more rigorous treatment based on the  $k \cdot p$  method is also possible [36]. Since it is not the focus of this thesis, it has been omitted due to its additional computational cost. Transport of bound carriers parallel to the quantum-well plane is governed by the thermodynamic model, albeit with reduced values for mobility and diffusion constants stemming from shorter scattering times as compared with bulk regions.

The exchange rate between the two carrier reservoirs is described by a capture and emission model, where carrier-carrier scattering as the underlying physical process is assumed to dominate. The model also takes into account a reduced capture rate as the bound states fill up when the laser is operated well above threshold. This effect is especially important in shallow electron-well devices such as InGaAsP-based lasers, which are the subject of this work. For these quantum-well lasers, the net capture rate given by [48]

$$C = \left( \frac{F_{3/2}(\eta_{3D})}{F_{1/2}(\eta_{3D})} - \frac{F_{3/2}(\eta_{2D})}{F_{1/2}(\eta_{2D})} \right) \frac{n_{3D}}{\tau}, \quad (2.16)$$

is used, where  $F_x$  represents the Fermi integral of order  $x$ . Here,  $\eta_{3D}$  and  $\eta_{2D}$  contain the quasi-Fermi level information for the mobile and bound carriers, respectively,

$$\eta_{3D} = (F_3 - E_C) / k_B T \quad \eta_{2D} = (F_2 - E_C) / k_B T, \quad (2.17)$$

and  $n_{3D}$  is the corresponding density of the former carriers. The capture time parameter  $\tau$  is considered to be a fitting parameter. The net capture rate enters the continuity equations for the current densities (2.2)–(2.3) as an additional recombination/generation term, and the total net recombination rate in the quantum-well regions can be written as

$$R^{tot} = R^{rad} + R^{nr} \pm C, \quad (2.18)$$

where the capture rate has the opposite sign for mobile and bound carriers due to their exchange process. The nonradiative recombination term  $R^{nr}$  is

the sum of the Auger and SRH recombination rates as previously discussed, whereas the radiative recombination term  $R^{rad}$  is the sum of the spontaneous and stimulated emission rates. For carriers confined to the quantum wells, the two constituents of the radiative recombination rate are calculated based on the solution of the Schrödinger equation for each well; otherwise, formula (2.13) is used.

The Newton method using the well-known box discretization is applied for the numerical solution of the coupled nonlinear partial differential equations (PDEs) [49]. As shown above, (2.1)–(2.4), the semiconductor equations can be written in divergence form equaling the divergence plus a scalar source term.

## 2.3 Optical Model

### Rate Equation Approach

The optical model is based on a rate equation approach. For each optical mode, a separate rate equation describes the temporal evolution of the mean electromagnetic energy. This approach is known as the adiabatic approximation [50] and is based on the assumption that the shape of the optical modes depends on the instantaneous value of the time-dependent dielectric function.

Starting from the time-domain Maxwell equations and employing the mode expansion

$$\mathbf{E}(\mathbf{r}, t) = E_0 \sum_{\nu} \Psi_{\nu}(\mathbf{r}; t) \sqrt{S_{\nu}(t)} e^{-i\omega_{\nu}t} e^{-i\phi_{\nu}(t)} + c.c. \quad (2.19)$$

in order to eliminate the fast timescale, the photon rate equation can be written as [45, 50, 51]

$$\partial_t S_{\nu} = (G_{\nu} - L_{\nu}) S_{\nu} + \beta_{\nu} R_{\nu}^{sp}, \quad (2.20)$$

where  $G_{\nu}$ ,  $L_{\nu}$ ,  $\beta_{\nu}$  and  $R_{\nu}^{sp}$  are the modal gain, effective modal loss, spontaneous emission coupling coefficient and spontaneous emission for mode number  $\nu$ , respectively. The constant  $E_0$  in (2.19) is chosen such



that the energy stored in the optical field inside of the cavity is  $W_{\text{opt}} = \hbar\omega S$ . The definition of the modal quantities is as follows

$$G_\nu(\omega) = \int g^{\text{loc}}(\mathbf{r}, \omega) |\Psi_\nu(\mathbf{r})|^2 d\mathbf{r} \quad (2.21)$$

$$R_\nu^{\text{sp}}(\omega) = \int r^{\text{sp}}(\mathbf{r}, \omega) |\Psi_\nu(\mathbf{r})|^2 d\mathbf{r} \quad (2.22)$$

$$L_\nu(\omega) = \int \alpha(\mathbf{r}, \omega) |\Psi_\nu(\mathbf{r})|^2 d\mathbf{r} + \frac{c}{2L} \ln \left( \frac{1}{r_0(\omega)r_1(\omega)} \right), \quad (2.23)$$

where  $g^{\text{loc}}$  is the local material gain,  $r^{\text{sp}}$  is the local spontaneous emission and  $\alpha$  is the free carrier absorption loss. Adopting semiclassical laser theory and applying Fermi's golden rule, the local material gain and spontaneous emission are given by

$$g^{\text{loc}}(\hbar\omega_\nu, \mathbf{r}) = C_0 \sum_{i,j} \int |M_{ij}|^2(\mathbf{r}) D(\mathbf{r}, E) \cdot (f_i^C(\mathbf{r}, E) + f_j^V(\mathbf{r}, E) - 1) L(\hbar\omega_\nu, E) dE \quad (2.24)$$

$$r^{\text{sp}}(\hbar\omega_\nu, \mathbf{r}) = C_0 \sum_{i,j} \int |M_{ij}|^2(\mathbf{r}) D(\mathbf{r}, E) \cdot f_i^C(\mathbf{r}, E) f_j^V(\mathbf{r}, E) L(\hbar\omega_\nu, E) dE, \quad (2.25)$$

where the integration is over all transition energies between an electron subband  $i$  and a hole subband  $j$ . The subband energies and the corresponding quantum-mechanical wavefunctions are obtained from the solution of Schrödinger's equation in one dimension under the assumption of flat bands<sup>1</sup>. In the above expressions,  $|M_{ij}|^2$  is the optical matrix element,  $D$  is the reduced density-of-states,  $f_i^C$  and  $f_j^V$  are the local Fermi-Dirac distributions for conduction and valence bands, and  $L$  is the linewidth broadening function. For more details on their exact form, refer to [40, 52]. The calculation of the radiative recombination rate that enters the current continuity equations (2.2) and (2.3) is also based on the coefficients  $g^{\text{loc}}$  and  $r^{\text{sp}}$  given above.

---

<sup>1</sup>For the above-threshold analysis of the lasers discussed here, this is a valid approximation.

For bulk active regions, expressions (2.24) and (2.25) are modified to reflect the lack of any quantum-mechanical confinement [40]: The sums over the subbands are reduced to one electron, one heavy-hole and one light-hole subband, whose respective energy offsets from the conduction and valence band are set to zero.

More advanced gain models in combination with a  $k \cdot p$  band structure calculation, which accounts for strain and valence band mixing effects, can also be used. These include a screened Hartree–Fock and a Born model [36, 53], which allow for the analysis of manybody effects. In general, the computational requirements forbid the direct use of such models in efficient full 3D simulations on existing computer hardware and limit their application to the analysis of laser diodes in two dimensions. However, a gain-table approach implemented within the *physical model interface* (PMI) framework of DESSIS as described in [36] is a practical alternative and within the scope of 3D simulations.

### Solution Strategy in 3D

Edge-emitting lasers such as FP, DFB and DBR lasers have an extreme aspect ratio with a device length much longer than the diameter of the cross section. Consequently, the electromagnetic waves propagate mainly along the longitudinal direction and it is a good approximation to consider TE and TM waves only. The optical modes are solutions of the reduced vectorial wave equation [54] for the transverse field<sup>2</sup>

$$\left( \nabla^2 + \frac{\omega_\nu^2}{c^2} \varepsilon(\mathbf{r}, \omega_\nu) \right) \Psi_\nu(\mathbf{r}) = 0, \quad (2.26)$$

where the parametric time-dependence of  $\Psi_\nu$  has been omitted for notational convenience.

Since the direct solution of Eq. (2.26) in three dimensions is too complex for the abovementioned laser types, a solution strategy is motivated, which is based on a separation ansatz. A general multisection laser diode consists of several active and passive sections, which can have an arbitrary grating corrugation. Additionally, a section with a modestly tapered waveguide is

---

<sup>2</sup>In the derivation of Eqs. (2.20) and (2.26), the  $\nabla(\nabla \cdot \mathbf{E})$  term, which arises from the vector identity  $\nabla \wedge \nabla \wedge \mathbf{E} = \nabla(\nabla \cdot \mathbf{E}) - \nabla^2 \mathbf{E}$ , has been neglected [55].

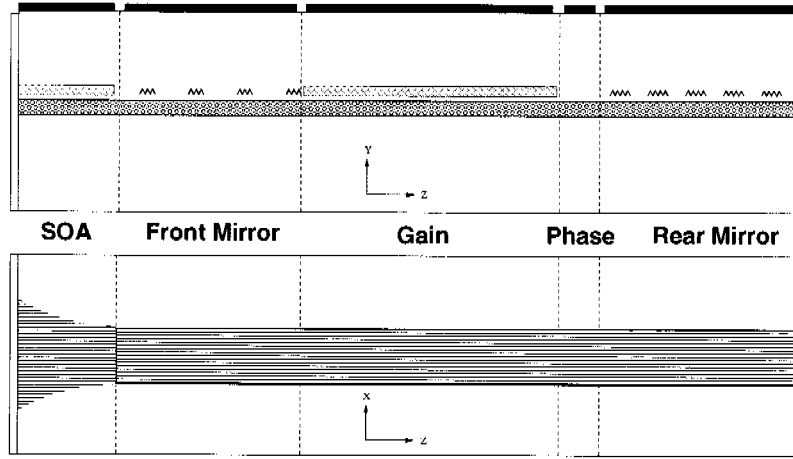


**Figure 2.1:** Schematic representation of the longitudinal side (top) and top (bottom) view of an integrated SOA and SGDBR laser. The top view indicates a tapered waveguide in the SOA section. Active multi quantum-well regions are red and the waveguide core including the grating is blue.

possible. As an example, we mention an SGDBR laser monolithically integrated with a (tapered) semiconductor optical amplifier SOA<sup>3</sup> as depicted in Fig. 2.1. It can be assumed that during operation the relevant laser parameters vary continuously within each section, whereas discrete changes across section interfaces are possible, for example, at active-passive transitions. In this case, the following separation ansatz can be made

$$\Psi_\nu(\mathbf{r}) = \Phi_{\nu\omega}(x, y; z)E_\omega(z). \quad (2.27)$$

To account for the longitudinal dependence of the dielectric constant  $\epsilon(\mathbf{r}, \omega)$  due to the inhomogeneous current and temperature distribution, each section is sampled at several positions along the  $z$ -axis. In this approach, we assume a hypothetical waveguide that coincides locally with the actual waveguide. The so-called local normal modes are not themselves solutions of the Maxwell equations since their parameters are functions of  $z$ . However, they can be superimposed to yield a solution of Maxwell's equations that represents the field of the actual waveguide [56]. The *local* character of the corresponding  $\nu$ -th order transverse mode pattern at oscillation frequency  $\omega$  is indicated by the colon-separated  $z$ -dependence of  $\Phi_{\nu\omega}$ .  $E_\omega(z)$  stands for the longitudinal electric field. The reduced vectorial wave equation (2.26)

<sup>3</sup>Similar devices have been fabricated at the University of Santa Barbara.

then decomposes into a finite number of two-dimensional Helmholtz equations

$$\left( \nabla^2 + \frac{\omega^2}{c^2} [n^2(\mathbf{r}, \omega) - n_{\nu\omega}^2(z)] \right) \Phi_{\nu\omega}(x, y; z) = 0, \quad (2.28)$$

and a one-dimensional longitudinal cavity problem of the form

$$(\nabla^2 + \beta^2(z)) E_\omega(z) = 0, \quad (2.29)$$

where the dielectric constant in Eq. (2.28) has been expressed in terms of the complex refractive index according to the relation  $\varepsilon(\mathbf{r}, \omega) = n^2(\mathbf{r}, \omega)$ . More details on the refractive index model are given later in this section.

In the above Helmholtz equation (2.28), the propagation constant  $\gamma_{\nu\omega} = \frac{\omega}{c} n_{\nu\omega}$  can be identified as the eigenvalue and  $n_{\nu\omega}$ , as the effective mode index of the *local* waveguide whose real part is the effective refractive index, and the imaginary part is related to the net modal gain by  $g_{net} = \frac{\omega}{c} \text{Im}(n_{\nu\omega})$ . In the longitudinal cavity problem,  $\beta$  reads as

$$\beta(z) = \frac{\omega}{c} n_{\nu\omega}(z) + i \frac{\Delta\alpha}{2}, \quad (2.30)$$

where  $\Delta\alpha$  is the net powerloss of the cavity.

Equations (2.28) and (2.29) together with the appropriate boundary conditions, standard Dirichlet / Neumann boundary conditions and Sommerfeld radiation boundary condition [57], respectively, determine the pairs  $(\Psi_\nu, \omega_\nu)$  of resonant modes and frequencies of the laser cavity. In order to suppress a net contribution to the longitudinal and temporal dependence of  $\Psi_\nu(\mathbf{r}; t)$ , the *local* transverse mode pattern  $\Phi_{\nu\omega}$  and the longitudinal field distribution  $E_\omega$  have to be normalized according to [41]

$$\iint |\Phi_{\nu\omega}(x, y; z)|^2 dx dy = 1, \quad \forall z \in [0, L], \quad (2.31)$$

$$\int_0^L |E_\omega(z)|^2 dz = 1, \quad (2.32)$$

where  $L$  is the cavity length.

The separation ansatz discussed in this section is illustrated in Fig. 2.2. It shows the different transverse mode patterns and corresponding effective mode indices for representative cross sections along the waveguide. In the

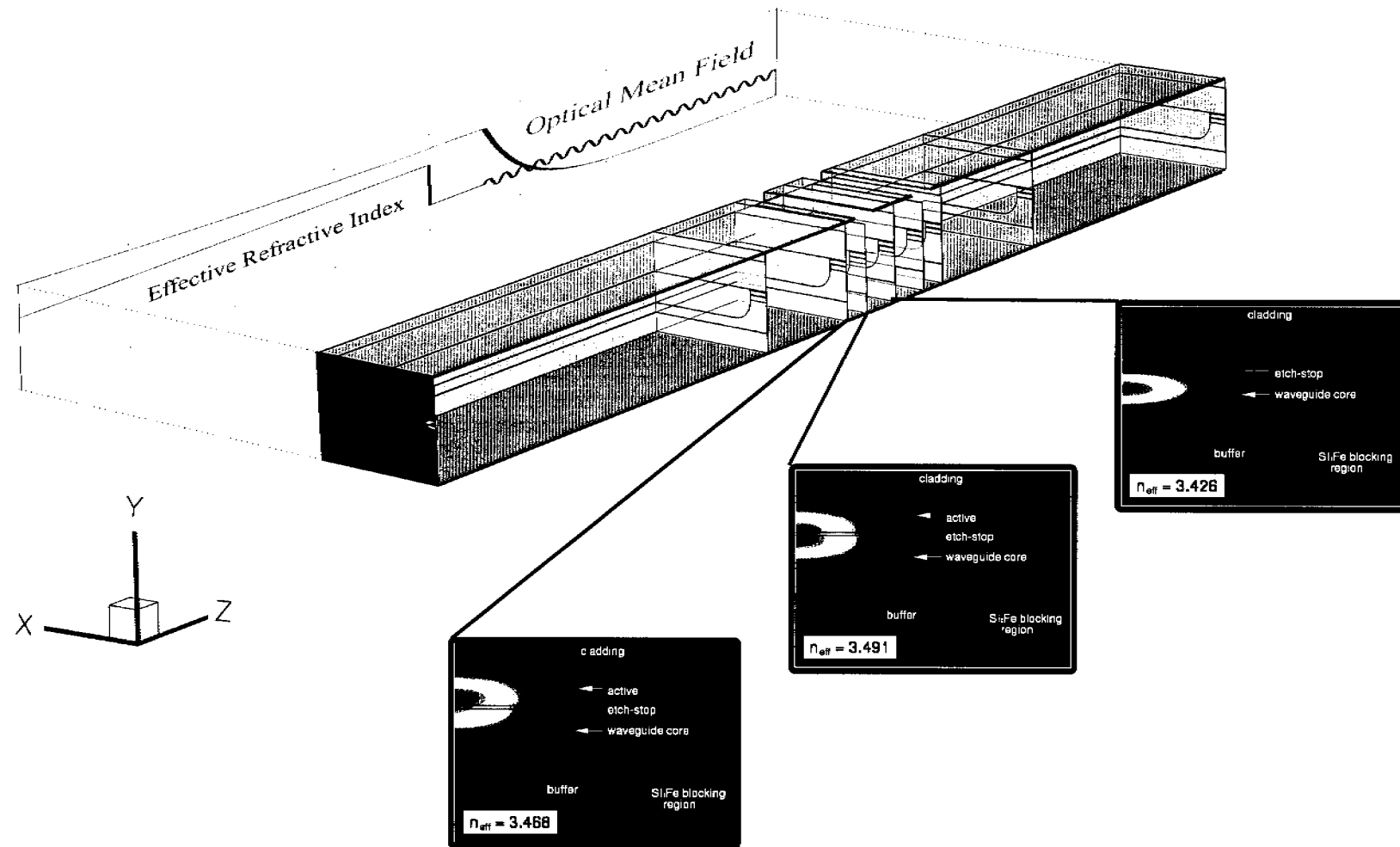


**Figure 2.2:** Illustration of the separation ansatz for the solution of the wave equation in 3D.

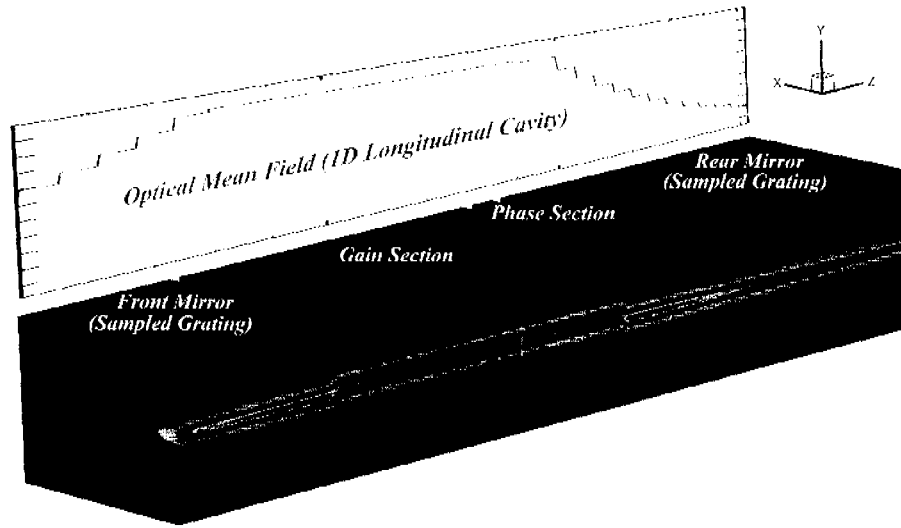


**Figure 2.3:** Optical intensity distribution of a planar buried-heterostructure SGDBR laser resulting from a separation ansatz with parametric  $z$ -dependence of the *local* transverse modes as described in Section 2.3. The longitudinal intensity envelope at transparency is given in the backdrop. The buried-heterostructure-type SGDBR laser has only been used to illustrate the 3D optical model.

backdrop, the solution of the longitudinal cavity problem together with the underlying refractive index distribution are indicated. The actual solution of the optical problem, following the separation ansatz, is depicted in Fig. 2.3 for a planar buried-heterostructure SGDBR laser.

## Optics in 2D

Often, 2D simulations provide sufficient insight into the physics of semiconductor lasers. A typical example is the FP laser but, even for tunable multisection lasers, a 2D analysis can sometimes be the best choice or, at least, a good starting point due to an inherently non-3D effect of interest combined with the computational efficiency.

In this configuration, the transverse mode pattern of only one representative device cross section is calculated. Usually, the laser is reduced to a cut through the active section, but for an analysis of the tuning efficiency  $\eta_t = |d\lambda/dI_t|$ , the grating section is chosen. On the other hand, the longitudinal cavity problem is not solved and the lasing frequency has to be

determined differently.

In contrast with FP lasers, where emission can be assumed to occur at the cavity mode closest to the gain peak, tunable lasers emit at the frequency fixed by their filter element—in the majority of cases, one or more grating sections. For single grating-section devices such as DFB or three-section DBR structures, laser operation at the Bragg frequency  $\omega_B$  can be assumed

$$\omega_\nu = \omega_B = \frac{\pi c}{\Lambda n_{\text{eff}}}, \quad (2.33)$$

where  $n_{\text{eff}}$  is the effective index<sup>4</sup> and  $\Lambda$  is the grating pitch. The situation for multiple grating-section devices is not as simple due to their interplay, and a predefined filter function, which accounts for that, would have to be used.

### Model of Refractive Index Tuning

The optical material properties are described by the complex refractive index,  $n(\mathbf{r}, \omega) = n' + in''$ , which relates the optical equations to the electronic equations. Its imaginary part  $n''$  contains the local material gain  $g^{\text{loc}}(\mathbf{r}, \omega)$  in the active region, which is positive if stimulated emission dominates and negative for direct interband absorption. Other kinds of absorption loss  $\alpha(\mathbf{r}, \omega)$  in non-active regions are also included. Then, the imaginary part of the index of refraction can be written as

$$n'' = \frac{c}{\omega} (g^{\text{loc}} - \alpha), \quad (2.34)$$

with  $g^{\text{loc}}$  and  $\alpha$  generally depending on carrier density, temperature and frequency. The same dependencies also hold for the real part  $n'$  when the Kramers–Kroenig relations [58] are taken into account. In the presented simulations, the dominant spectral dependence of the carrier-induced complex refractive index change is modelled according to [59, 60, 61]

$$\Delta n' = -\frac{e^2}{2n'\epsilon_0\omega^2} \left( \frac{n}{m_e} + \frac{p}{m_h} \right) \quad (2.35)$$

$$\Delta n'' = -\frac{e^3}{2n'\epsilon_0\omega^3} \left( \frac{n}{m_e^2\mu_e} + \frac{p}{m_h^2\mu_h} \right). \quad (2.36)$$

---

<sup>4</sup>The effective index  $n_{\text{eff}}$  is equivalent to the real part of the effective mode index  $n_{\nu\omega}$  defined in (2.28).

As an alternative, a lookup-table approach compiled from microscopic calculations is also possible.

The carrier-induced index change in a semiconductor laser has a negative sign and can be compensated in part by the temperature change due self-heating in the device. The temperature dependence of the refractive index is through the band gap and the high-frequency dielectric constant. For InGaAsP waveguides lattice matched to InP, an analytical molefraction-dependent model has been presented [62] and an extension with a fit to measurements in [63] has been given in [61]. Here, we assume a linear response to the temperature change

$$\Delta n' = \alpha_{th} \cdot \Delta T, \quad (2.37)$$

where  $\alpha_{th} > 0$  is extracted from measurements.

The index change induced by the applied electric field—known as Pockels effect (linear dependence) and Kerr effect (quadratic dependence)—during tuning operation has been neglected because only forward-bias tuning is discussed in this thesis, which exhibits a very low change in electric field.

## Conclusion

An optical model has been presented that allows for efficient EEL simulation in full three dimensions by using a parametric separation ansatz. Its implementation will be described in the following chapter. In addition, the underlying refractive index model has been discussed and a brief outline for an alternative 2D simulation approach has been given. It should be noted that a more rigorous approach would cover the coupling between all local normal modes of neighboring longitudinal positions. In this approach, two approximations are made. First, coupling between neighboring normal modes only of the same order is considered. Second, the one-dimensional wave equation (2.29) essentially describes power coupling of the modes along the  $z$ -direction. These assumptions greatly simplify the analysis, while little accuracy is lost for the earlier mentioned laser structures.

The approach outlined in this section is well suited to the efficient simulation of general active structures such as sampled-grating DBR lasers [64], tapered waveguide lasers [65, 66] and other monolithically integrated optoelectronic devices. A discussion of how the approach can be applied to other tunable lasers is given in Section 2.4.



## 2.4 Opportunities and Limitations of 3D Model

In the previous section, an optical model was presented that takes into account the three-dimensional nature of multisection devices. Based on several assumptions that hold, in principle, for a large number of semiconductor lasers, a solution strategy for Maxwell's equations in three dimensions has been formulated. It was motivated and illustrated by an SGDBR laser.

In this section, let us look beyond the SGDBR structure and assess which of the other types of tunable laser introduced in Section 1.1 and summarized in Table 1.1 are also covered within this framework. The question of what information can be extracted from a 3D model and of how much one gains in accepting an increased computational effort will be addressed in Chapter 4.

Before turning to tunable lasers, it should be noted that **FP lasers** can be viewed as **DFB lasers** in the limit of zero grating coupling coefficient and, as such, they evidently fall within the above framework. However, a 2D simulation often is the optimum choice for device optimization, unless longitudinal inhomogeneities, such as truncated contacts, are introduced to improve performance. For configurations like this, the author of [41] has pointed out the need for a 3D simulation.

The **TTG DFB laser** also satisfies the requirements of the extended optical model. Since its waveguide is longitudinally invariant, except for the DFB grating, the results of 3D simulations would hardly be affected by the approximations mentioned in the previous section. If seeking to model both the transverse cross section including the lateral tuning contact and the longitudinal grating together with the facet coatings accurately, one needs to resort to the 3D model. The same also holds for the widely tunable descendant of the TTG structure: the **SG TTG laser**.

On the other hand, the **VMZ laser** relies on an interferometric tuning mechanism, which would require a modified treatment. Instead of left-propagating and right-propagating modes of the same order, one needs to analyze codirectionally coupled modes of different orders. Given the respective transverse modes at any one position along the waveguide, which are characterized by the corresponding propagation constants, it is possible to solve the longitudinal cavity problem by a transfer matrix formalism.

The **GCSR laser** can be approached in a similar way but, in addition, it is necessary to consider the contradirectional coupling both in the grating-assisted coupler and in the rear sampled reflector. Therefore, sections with two waveguides and incorporated gratings have to be treated as four-port

problems with a corresponding  $4 \times 4$  transfer matrix, whereas single waveguide sections—with or without gratings—can be considered as two-port problems with  $2 \times 2$  transfer matrices [34].

Although the **MG-Y laser**, like the VMZ laser discussed above, is also based on an interferometric structure, its straightforward treatment in the presented framework is not possible due to the Y-branch waveguide. The separation into several local transverse modes and one longitudinal cavity problem is no longer valid. Instead, some type of beam-propagation method (BPM) or full-modal propagation analysis would be necessary to describe accurately the multimode interference (MMI) coupler at the branching point [30].

As an approximation, however, one could perform a separate 3D simulation for each of the two branches containing the modulated grating and compile an effective rear mirror reflectivity table in a preprocessing step: For each combination of branch currents, the corresponding reflectivities would be added and stored together with the phase information. The table could then be used to simulate the remaining FP cavity consisting of a gain and phase section subject to some additional loss incurred by the MMI coupler.

Certain device structures that differ from the SGDBR laser only in their specific grating design in the front- and/or rear-mirror section can be simulated directly—without having to modify the 3D optical model. Among these are the **DBR**, **SSGDBR** and **DSDBR lasers**. Despite the similar concept of forming a cavity with two DBR stacks, **VCSELs** cannot be treated in the same framework due to their different device topology. Instead, the VCSEL simulator in DESSIS has been extended to full 3D using an effective index method (EIM) to solve the optical problem [67]. For an accurate treatment of the tuning behavior of VCSELs based on curved MEMS mirrors, however, the effective index method, which is based on the paraxial approximation, is currently being replaced by a full 3D finite-element Maxwell solver. In contrast to the finite-element approach, it is difficult for an EIM solver to account for the cavity losses that are introduced by the lateral propagation resulting from the curved mirrors. Especially for higher-order modes this issue cannot be neglected.

### **Conclusion**

The discussion in this section has shown that the 3D optical model derived in Section 2.3 can be applied to a wide range of edge-emitting laser diodes. Subject to the outlined modifications for some device structures, all monolithically integrated tunable lasers from Table 1.1 can be treated within the presented framework, except for MG–Y lasers and VCSELs. In addition, beyond the scope of that approach is the rigorous 3D simulation of most external cavity lasers and DFB laser arrays. An optical circuit approach similar to the one proposed in [36], in combination with the comprehensive simulation of individual components, is possibly the best option for the analysis of that group of lasers.

Seite Leer /  
Blank leaf

# Chapter 3

## Numerical Implementation

### 3.1 Introduction

In this chapter, the numerical implementation of the physical models required to describe the wavelength tuning behavior of DFB/DBR lasers is highlighted. Previously, the physics of general edge-emitting-type semiconductor lasers has been summarized along with the resulting governing equations. Different problem classes such as systems of nonlinear partial differential equations (PDEs) and various eigenvalue problems have been identified. The appropriate discretization schemes and numerical solution methods together with the extensions carried out in this thesis will be reviewed in the following section.

To find a self-consistent solution of the thermodynamic transport equations on the one hand and the optical equations on the other hand, a coupling scheme is employed that takes into account the different coupling strengths of the involved subproblems. The coupling scheme and the resulting simulation flow for an electrothermo-optical device simulation of a tunable semiconductor laser are discussed in Section 3.3.

Tunable multisection lasers are complex optoelectronic devices in that specific currents have to be injected into all of their sections simultaneously to access a desired wavelength at a given optical output power. In commercial applications, these lasers are commonly equipped with feedback control circuitry to ensure proper operation. How this issue can be addressed in the

simulator is the subject of the last section of this chapter. Furthermore, an efficient algorithm is presented that can speed up the calculation of the lasing wavelength in the self-consistent iteration scheme.

## 3.2 Discretization and Solution Methods

The spatial discretization of the device geometry plays a crucial role in the solving process of the physical equations. An optimal finite-element type grid should be able to reproduce the real device as closely as possible and to minimize the discretization error by exhibiting a sufficiently fine resolution. On the other hand, the number of grid points has to be kept to a minimum due to limited computational resources. With today's computer hardware, this aspect has become less important for the majority of 2D simulations. Yet, in 3D simulations, the large device size<sup>1</sup> combined with nanoscale features of typical QW multisection lasers can still easily lead to an unmanageable computational task.

### 3.2.1 Electrothermal System<sup>2</sup>

#### Scharfetter–Gummel Box Method Discretization

In DESSIS, the so-called box method [49] is used for the discretization of the PDEs describing the thermodynamic transport. The box method is applied to a boundary Delaunay [68] mesh in order to avert singularities and related numerical convergence problems connected with obtuse angles and *boxes* not completely contained in the simulation domain. The formulation of the box method on mixed-element meshes, which are generated by a modified octree approach [69], allows for an accurate fitting of the geometry, while saving on the number of mesh points wherever possible—the latter being especially important in the context of 3D simulations. The choice of box method coefficients leads to different variants of that method [70]. In 3D, the best results have been achieved by computing these coefficients with an edge-oriented element intersection algorithm<sup>3</sup>. The discretization

---

<sup>1</sup>The simulated device size of a typical tunable multisection laser is of the order of  $10\mu\text{m} \times 10\mu\text{m} \times 1000\mu\text{m}$ .

<sup>2</sup>With electrothermal system it is also referred to the photon rate equation, since it is included in the system of coupled PDEs.

<sup>3</sup>For more details, see [71] and the example of the DESSIS command file in Appendix A.

of the current density equation follows the Scharfetter–Gummel approximation [72, 73], which guarantees the numerical stability of the box method.

The inclusion of the photon rate equation (2.20) into the electrothermal part of the simulator is implemented by means of a "virtual mesh" [40] that links the photon rate of each lasing mode to all spatial vertices on which the calculation of the modal variables depends. Hence, every photon rate equation is assigned to a corresponding virtual photon rate vertex. Since this thesis is restricted to quasistationary simulations, all time derivatives are omitted. For the discretization of the time axis in transient simulations, refer to [38, 74].

In general, mesh generation for 3D device simulations for multisection lasers with large aspect ratios is still an ambitious problem. Due to the three-point model for the discretization of quantum wells in DESSIS [71], further restrictions are imposed on the simulation mesh. Since the quality of the mesh has a strong influence on the convergence behavior—and its size determines the computational task—a discussion of mesh generation is included in the guide for 3D laser simulation in Section 4.5.

### Solving the Coupled PDEs

For the solution of the system of strongly coupled nonlinear PDEs consisting of the discretized thermodynamic transport and photon rate equations, a damped iterative Newton–Raphson scheme developed by Bank and Rose [75, 49] is employed.

The system of equations can be written in vector form as

$$\vec{\mathcal{F}}(\mathbf{x}) = \mathbf{0}, \quad (3.1)$$

where the solution variables are the components of the vector  $\mathbf{x}$ . In consecutive iterations an initial guess  $\mathbf{x}^i$  is improved according to

$$\vec{\mathcal{F}}'(\mathbf{x}^i) \cdot \Delta \mathbf{x}^i = -\vec{\mathcal{F}}(\mathbf{x}^i) \quad (3.2)$$

$$\mathbf{x}^{i+1} = \mathbf{x}^i + \alpha^i \Delta \mathbf{x}^i, \quad (3.3)$$

where the positive damping factor  $\alpha^i \leq 1$  is introduced to prevent overshoot effects if  $\mathbf{x}^i$  is far away from the final solution. In (3.2),  $\vec{\mathcal{F}}'$  denotes the Jacobian matrix of the vector-valued function  $\vec{\mathcal{F}}$  and reads as

$$\left[ \vec{\mathcal{F}}'(\mathbf{x}^i) \right]_{mn} = \left. \frac{\partial \mathcal{F}_m(\mathbf{x})}{\partial x_n} \right|_{\mathbf{x}=\mathbf{x}^i}. \quad (3.4)$$

The Newton iterations are stopped if either of two convergence criteria is met: One imposes an upper limit on the norm of the right hand side  $\|\vec{F}(\mathbf{x}^j)\| < \epsilon_{abs}$ , whereas the other restricts the relative error<sup>4</sup>

$$\frac{\|\alpha^i \Delta \mathbf{x}^i\|}{\|\mathbf{x}^i\|} < \epsilon_{rel}. \quad (3.5)$$

With a sufficiently good initial guess, the above scheme can be expected to converge quadratically. Since the Newton method is based on a Taylor series expansion that neglects terms of second and higher order in  $\Delta \mathbf{x}$ , the set of linear equations (3.2) is obtained. In semiconductor device simulation, normally poorly scaled and highly ill-conditioned linear systems resulting from rapidly varying solution components and large element aspect ratios have to be solved. These systems are characterized by an unsymmetric sparse matrix.

### Choosing the *Right* Linear Solver

Several different linear solvers are available and, in making a choice, one has to consider several factors: accuracy, speed, robustness, memory requirements, capability for parallelization, and the underlying problem, to name but the most important. Most solvers can be grouped in two categories consisting of either so-called direct solvers or iterative solvers.

All direct methods for the solution of sparse systems of linear equations are, in principal, based on the standard Gauss elimination technique. Before the coefficient matrix is decomposed into a form that is easier to solve, several ordering methods can be applied to improve the performance of the factorization. Similar methods are also used in iterative solvers to lower the condition number of the resulting matrix. However, the actual solution process consists of an iterative scheme, which only approximates the solution to a given accuracy in each iteration step and leads to a reduced memory footprint.

It turns out that linear systems arising from small-sized to medium-sized 2D device simulations are generally solved most efficiently by using a direct solver, for example, an LU decomposition method, as implemented in the state-of-the-art parallel solver PARDISO [76, 77]. When memory is not a

---

<sup>4</sup>For very small updates of  $\mathbf{x}^i$ , a modified relative error control, based on the value of a reference variable, is used in DESSIS [71].



limiting factor, the performance of direct solvers is usually superior. Iterative solvers may be the better option both for 2D simulations with very large mesh sizes and for extended 2D<sup>5</sup> simulations—mainly due to significantly lower memory consumption.

In most 3D simulations, however, iterative solvers are unrivaled and often the sole option not only as far as their memory requirements are concerned but also in terms of speed. With system matrices having more than 300 000 unknowns with over 20 million elements, a speedup of factor ten for a full simulation can be reached compared to direct solvers [78]. If only the time for the linear solver is compared, this factor can even be as high as 50. Moreover, memory usage in large 3D simulations can be four times smaller when using an iterative solver, thus enabling simulations that would otherwise go beyond 32GB of memory and not be suitable for most device manufacturers or fabless design-houses. For more details, the reader is referred to the respective sections on simulation statistics in Chapter 4.

DESSIS provides two iterative solver packages [71]: a sequential solver called Slip90 and a parallel solver called ILS. Since the more recently developed ILS is generally superior to Slip90, only the former has been used in this work. A comparison among all linear solvers mentioned in this section along with an exhaustive discussion of ILS can be found in [78]. In the following, only a brief sketch of the algorithms employed by ILS is given.

State-of-the-art iterative solvers like ILS consist of several building blocks<sup>6</sup>. Some linear systems arising in semiconductor device simulation, for example, cannot be solved at all without a suitable preconditioner. Its role is to replace the original linear system with an equivalent one, whose solution requires considerably fewer iteration steps. This solver uses a threshold-based incomplete LU factorization (ILUT) as preconditioner. Several iterative methods are available in ILS. Throughout this work, the biconjugate gradients stabilized method (BiCGStab) is used, which belongs to the class of so-called Krylov subspace methods. Permutations and scalings are yet other building blocks, which play a similar role as preconditioners. Sometimes, for example, a matrix with zeros on the diagonal can cause problems and, therefore, it can be advantageous to reorder it before the pre-

---

<sup>5</sup>What is to be understood by extended 2D is illustrated in Section 4.3.4.

<sup>6</sup>The solver package ILS provides several different algorithms for most building blocks. Here, only the combination of algorithms with the best overall performance in our simulations is summarized.

conditioner is applied. For unsymmetric permutations, the MPS<sup>7</sup> algorithm is used, whereas the nested dissection (ND) algorithm performs a symmetric permutation.

Some of the above algorithms can be fine-tuned by adjusting parameters that control the accuracy or determine a termination criterion. There are situations in which a higher accuracy in the preconditioner may reduce the required number of iterations of BiCGStab and, hence, more than compensates the extra computation time needed by ILUT. Sometimes, only the *right* choice of parameters will lead to a solution of the system at all. Therefore, it may be necessary to modify the default parameters to achieve the best performance for a given problem.

Figure 3.1 shows the strong influence of the solver parameters for a full-3D electrothermo-optical simulation of a three-section DBR laser.<sup>8</sup> In particular, the settings of the preconditioning step have a major impact on the performance of ILS. The ILUT( $\epsilon, q$ ) preconditioner has two parameters [78]:  $\epsilon$  determines up to which magnitude an element is dropped during the factorization and  $q$  limits the number of entries in each row. In Fig. 3.1,  $\epsilon$  is varied over two orders of magnitude, while  $q$  is set to infinity. Three important conclusions can be drawn from the stacked bar chart. First, the total computation time has a minimum with respect to the drop tolerance. Second, the *wrong* choice of  $\epsilon$  can more than double the overall simulation time—where typical computation times are in the order of days, it is essential to choose a near optimal  $\epsilon$ . Third, the best performance of the solver is achieved if the relative time spent in the preconditioner nearly equals that of the iterative method. The decrease of the average number of iterations required per Newton step, due to a higher accuracy of the preconditioner, is shown in Fig. 3.2.

The last conclusion is of practical significance because, in general, it also holds for a single Newton iteration. Hence, a good drop tolerance can be guessed by comparing the relative computation times for only a few bias points with different values for  $\epsilon$ . Moreover, using a parabolic fit with three interpolation points, an optimal value can be determined at little cost compared with the total simulation time. The configuration file for ILS that has served as a good starting point in all of the full-3D simulations is listed at the end of Appendix A.

<sup>7</sup>MPS stands for "Maximize product on diagonal with scalings."

<sup>8</sup>For more details about the laser structure and corresponding simulation results, the reader is referred to Section 4.3.

A further substantial speedup can be achieved by running ILS in parallel mode. However, its excellent parallelization capabilities on shared-memory architectures [78] had not been ported to the fastest available computer architecture at the time of publication. As a consequence, only the sequential mode has been used in this work.

### 3.2.2 Optics

In this section, the numerical implementation of the optical equations outlined in Section 2.3 will be highlighted with respect to modeling the wavelength tuning behavior of multisection DBR lasers. Since the device simulator DESSIS allows for the simulation of different classes of active optoelectronic devices, the corresponding optical mode solvers are integrated in a separate library called LUMI [79, 43], which can also be used in stand-alone mode. The implementation of the 3D optical mode solver has been carried out partly in LUMI and partly in an interface class in DESSIS that has been designed for dual-grid simulations [36]—for certain devices, it can be advantageous to use independent meshes for the electrothermal and optical simulation [43]. How the different parts of the solver are connected is summarized at the end of this section.

In contrast to standard Fabry–Perot laser diodes, the emission wavelength can no longer be assumed to coincide with the modal gain peak. Depending on the amount of current injected into the grating sections of an SGDBR laser, the lasing wavelength can be tuned over a range of up to 100nm. Furthermore, discrete mode jumps are possible and the convergence criteria have to be reviewed. Since the product of the power reflectivities of the front and rear mirror at the resonant wavelength varies during tuning operation, the corresponding mirror loss and threshold gain are subject to change. At last, the influence of the tuning operation on the optical mode pattern should also be mentioned here.

#### Constituents of 3D Optics Solver—2D Solver

Solving Eq. (2.26) by the separation ansatz (2.27) requires the solution of two different classes of eigenvalue problem. For the discretization of the 2D Helmholtz equation (2.28), a finite-element method is employed as presented in detail in [79, 80]. The resulting complex-valued algebraic eigenvalue problem of the form

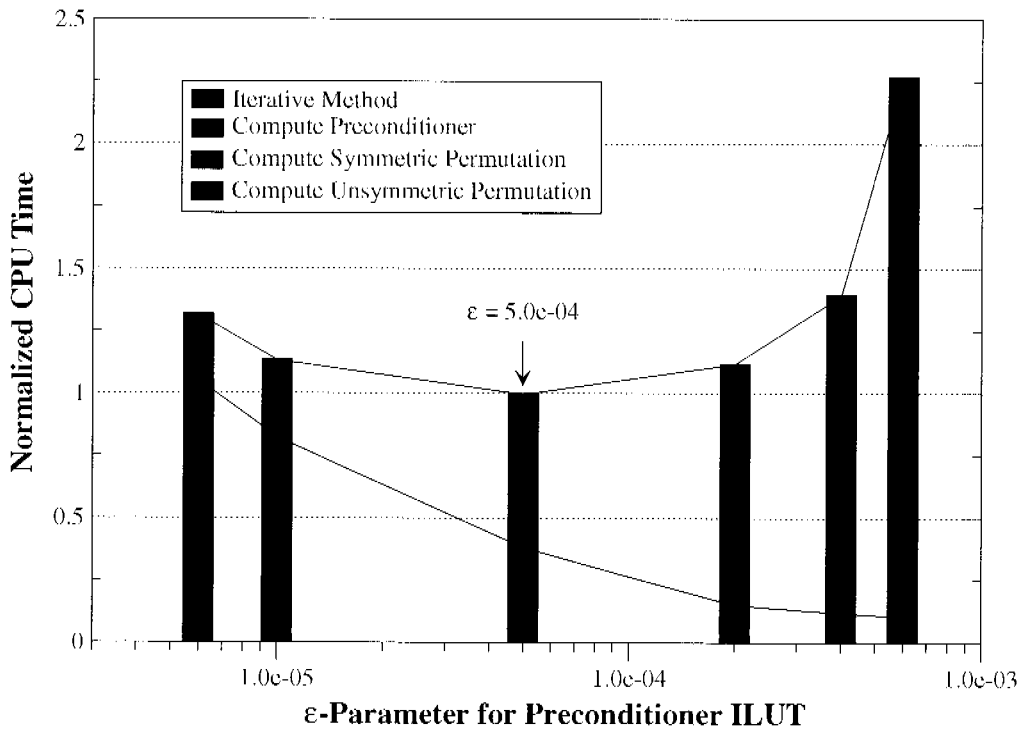


**Figure 3.1:** Simulation time of the iterative linear solver ILS with respect to the drop tolerance  $\epsilon$  of the preconditioner  $\text{ILUT}(\epsilon)$ . The cumulative bars of time spent in different parts of the solver indicate that ILS performs best if the computation time for the preconditioner and the iterative method is balanced. The CPU times are normalized with the total time needed for  $\epsilon = 5.0\text{e-}04$ .

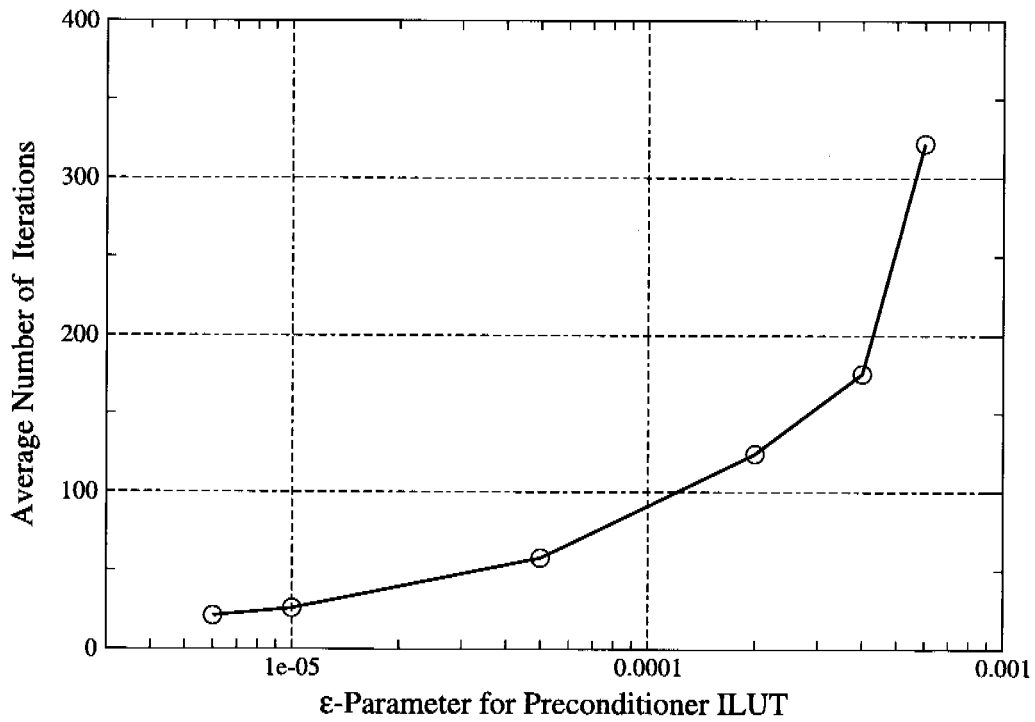


**Figure 3.2:** Average number of ILS iterations per Newton step for different values of the drop tolerance parameter  $\epsilon$  in the preconditioner  $\text{ILUT}(\epsilon, q)$ . A more accurate preconditioner reduces the computational task for the iterative method; however, at a certain point, this advantage is compensated by the increased computation time of the preconditioner.

$$\mathbf{A}x = \lambda \mathbf{M}x, \quad (3.6)$$

$$\mathbf{A}, \mathbf{M} \in \mathbb{C}^{n \times n}, x \in \mathbb{C}^n, \lambda \in \mathbb{C}$$

is solved very efficiently with a Jacobi–Davidson QZ (JDQZ) subspace iteration method [81]. This method also allows to *recycle* a previous solution of a slightly perturbed eigenproblem [82]. Instead of using a random vector to construct the search subspace, the former eigenvector is taken. Similarly, the former eigenvalue can be used as an initial guess for the consecutive problem. In addition, the preconditioner that is applied before JDQZ can also be reused. Since a large number of Helmholtz problems—one for each transverse cross section along the waveguide, typically about 40 or more—have to be solved iteratively for each bias point during a simulation, a substantial overall speedup can be reached.

### Constituents of 3D Optics Solver—1D Solver

On the other hand, the longitudinal equation (2.29) represents a generalized non-hermitian nonlinear eigenvalue problem of the form

$$\mathbf{A}x = \xi \mathbf{B}(\xi)x, \quad (3.7)$$

$$\mathbf{A}, \mathbf{B} \in \mathbb{C}^{n \times n}, x \in \mathbb{C}^n, \xi \in \mathbb{C}$$

with the complex eigenvalue  $\xi = \omega/c + i\Delta\alpha$ .

Although we mostly deal with periodic grating corrugations which can be treated analytically in the framework of coupled mode theory [83, 84, 85], the inhomogeneous carrier and temperature distribution during laser operation demands a numerical solution. To this end, a transfer-matrix formalism has been chosen that relates the right- and left-propagating waves at one point of the structure to the right- and left-propagating waves at a neighboring point [86, 87]

$$\begin{pmatrix} E^r(z_i) \\ E^l(z_i) \end{pmatrix} = \begin{pmatrix} T_{11} & T_{12} \\ T_{21} & T_{22} \end{pmatrix}_i \begin{pmatrix} E^r(z_{i+1}) \\ E^l(z_{i+1}) \end{pmatrix}. \quad (3.8)$$

Cascading all transfer matrices yields a system matrix

$$\mathbf{T}_{sys} = \prod_{i=1}^N \mathbf{T}_i, \quad (3.9)$$

where  $N$  is the number of minisections<sup>9</sup> in each of which the material properties in the longitudinal direction are assumed to be constant. Applying the Sommerfeld radiation condition [57] requires  $\mathbf{T}_{22} = 0$  and, hence, the problem reduces to a complex root search, for which a variant of the nonlinear simplex algorithm developed by Nelder and Mead [88] is employed.

This algorithm is more suitable than derivative-based methods since no analytical derivatives are available. Moreover, it is a very robust method that makes almost no special assumptions about the underlying function, which guarantees its suitability for a wide range of problems. The latter comes at the price of not always being the fastest method. However, for a commercially used general-purpose device simulator such as DESSIS the criterion of robustness outweighs the occasional performance gain.

For the solution of the one-dimensional cavity equation, the effective mode-index distribution is superimposed with the grating corrugation  $\Delta n_{gr}(z)$ . In this way, Eq. (2.29) can be solved for an arbitrary variation in the superimposed effective mode index if the discretization of the  $z$ -axis is chosen small enough so that  $n_{\nu\omega}^{tot}(z) = n_{\nu\omega}(z) + \Delta n_{gr}(z)$  is well approximated by a piecewise constant function. As the effective mode index  $n_{\nu\omega}$  generally is a slowly varying function except at active-passive section interfaces, a coarser sampling of the  $z$ -axis in combination with a linear interpolation is permissible.

### Aspects of Multimode Simulation

In a general multimode simulation, one has to consider several longitudinal modes for each *local* transverse mode. Furthermore, in order to include dispersion, Eq. (2.28) has to be solved at each sampling position for a range of frequencies within which the longitudinal resonant frequencies with lowest threshold gain are expected. In this context, the frequency  $\omega$  can be seen as an input parameter in the Helmholtz equation and a position- and frequency-dependent function  $n_{\nu\omega}(z)$  can be compiled. The actual frequencies of the lasing modes are then obtained from the longitudinal cavity problem. For single longitudinal-mode simulations, dispersion can also be included using a Taylor expansion of the complex refractive index at a target frequency  $\omega_0$

---

<sup>9</sup>Here we refer to minisections in order to avoid confusion with sections of a multi-electrode laser. For the latter, the number of minisections is always greater than the number of functional sections.

in the neighborhood of the resonant frequency

$$n(\mathbf{r}, \omega) = n(\mathbf{r}, \omega_0) + \Delta\omega \left. \frac{\partial n}{\partial \omega} \right|_{\omega_0}. \quad (3.10)$$

In a multi-longitudinal-mode setting, this approximation may no longer be valid if the difference between the target frequency  $\omega_0$  and the side-mode frequency  $\omega_1$  is large as is typically the case in SGDBR lasers.

### Implementation Notes

In the derivation of the photon rate equation (2.20) and the corresponding optical eigenvalue problems (2.28) and (2.29), the imaginary part of the eigenvalue in (2.29) can be identified with the difference term  $(G_\nu - L_\nu)$  in the photon rate equation [89]. However, on numerical grounds, it is advantageous to calculate this term using the integral approximations (2.21) and (2.23) due to the nonlocal nature of the eigenvalue. This allows for the calculation of the local partial derivatives in the Jacobian matrix, which guarantees the convergence properties of the Newton method.

The implementation of the 3D Optics solver in DESSIS is based on a scheme of using separate grids for electrothermal and optical calculations, which arose in the development of the VCSEL simulator [36, 43]. For the 3D simulation of tunable edge-emitting type lasers, this scheme has been extended to allow for as many optical grids as there are user-specified cross sections.

Each cross section is characterized by its location along the waveguide axis and can have its own mesh and 2D mode solver together with a specific target eigenvalue. For cross sections that coincide with an antireflection (AR) or high reflection (HR) coating, which are common in tunable multi-section lasers, the optical mode pattern of the nearest neighbor cross section is copied. In this way, suitably fine meshes for the solution of the 2D problems can be chosen, while the 3D mesh can be optimized with respect to the electrothermal system. The only disadvantage of this approach is that two extra interpolation steps are required: one to map the complex refractive index distribution onto the optical grid of the various cross sections and the other to transfer the 3D optical mode pattern back onto the electronic grid. However, the accuracy of the optical solutions on the finer 2D meshes outweighs the inherent interpolation errors. All interpolation tasks are carried out using the interpolation library DIP [71].



A flowchart of the 3D optics solver is shown in Fig. 3.3. Several steps are necessary to obtain the optical mode pattern and the according lasing frequency. These steps can be divided into tasks that require the solution of an optical equation (red shaded boxes) and others that perform various types of multidimensional interpolations as shown in the gray-shaded boxes.

### 3.3 Coupling Scheme

One of the major difficulties in optoelectronic device simulation is to master the coupling among the different physical equations in a robust, efficient and numerically stable way. While the solving of each subproblem can be straightforward, the mutual dependencies of the solution variables—often highly nonlinear in nature—can make the process of obtaining a global self-consistent solution very difficult. Therefore, the coupling scheme plays a crucial role for the convergence behavior of the full system.

The strong coupling of the optics and electronics, characterized by the several orders-of-magnitude change in optical intensity across threshold, is treated by incorporating the photon rate equation (2.20) into a Newton–Raphson updating scheme [41]. What is usually referred to as weak coupling in Fabry–Perot laser simulations, that is, the dependence of the electro-thermal equations together with the photon rate equations on the optical field distribution and the lasing wavelength, is not strictly true for SGDBR-type lasers. However, experience shows that a *modified* Gummel-type iteration scheme between Eqs. (2.1)–(2.4) and Eq. (2.26) can be employed to obtain a fully self-consistent solution of the whole nonlinear system. The necessity for a *modified* Gummel-type iteration scheme will be explained in the following section.

The simulation flow for a general three-dimensional simulation of a tunable multisection DBR laser is illustrated in Fig. 3.4. At each bias point, the coupled system of PDEs and the optical eigenmodes along with the lasing wavelength are solved self-consistently in a Gummel-type iteration scheme [90]. The solution of the system of PDEs using a Newton–Raphson scheme is followed by the computation of the optical eigenmodes and lasing wavelength. Due to the interaction between optics and electronics, this procedure has to be repeated at least once to ensure overall convergence. This inner loop, which is indicated by the red arrow in Fig. 3.4, is reiterated until convergence is reached. The convergence criteria are based on the solution

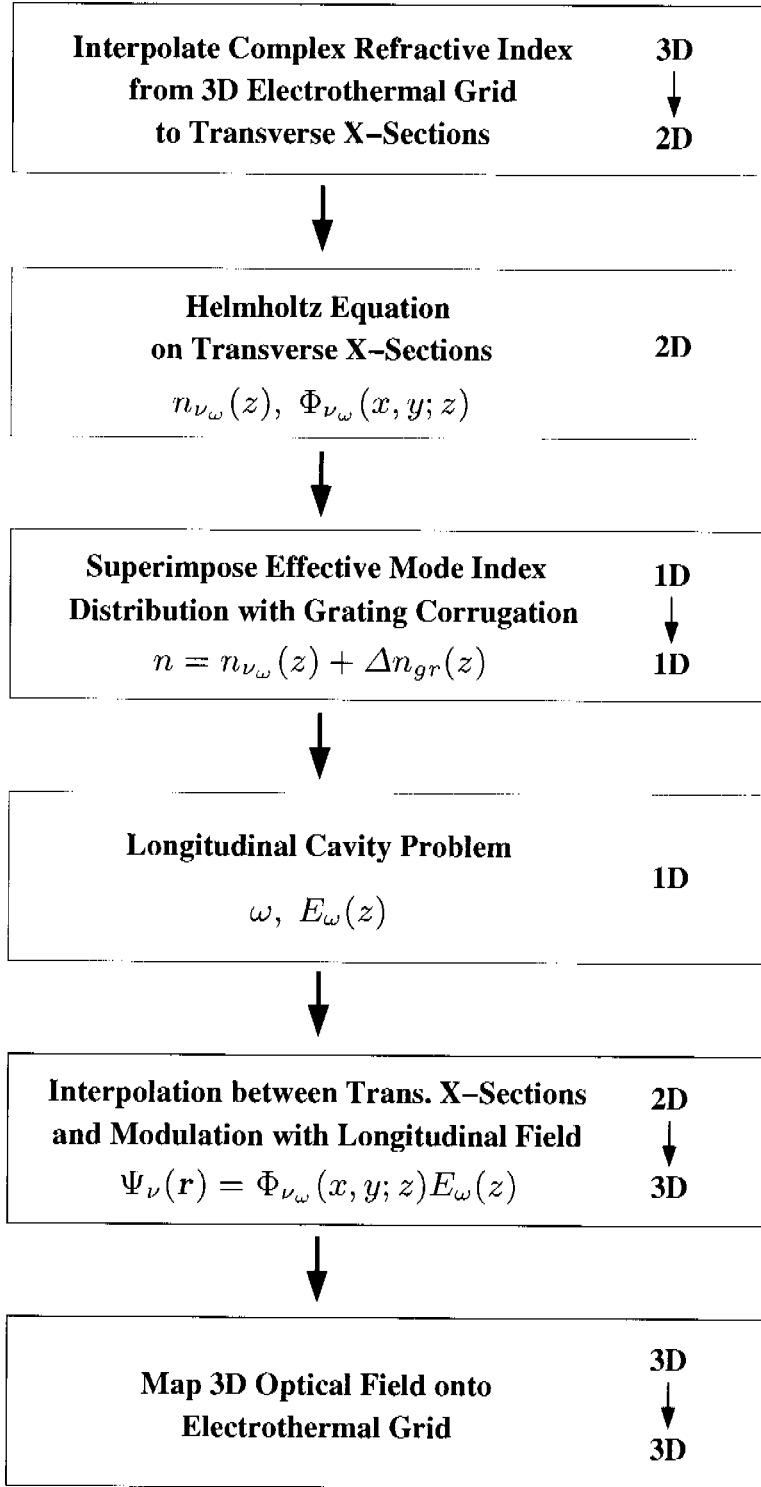


**Figure 3.3:** Flowchart of 3D optics solver: Boxes shaded in red require the solution of an optical equation, whereas gray shaded boxes stand for interpolation tasks. The position of the optics solver in the full simulation flow can be seen in Fig. 3.4.

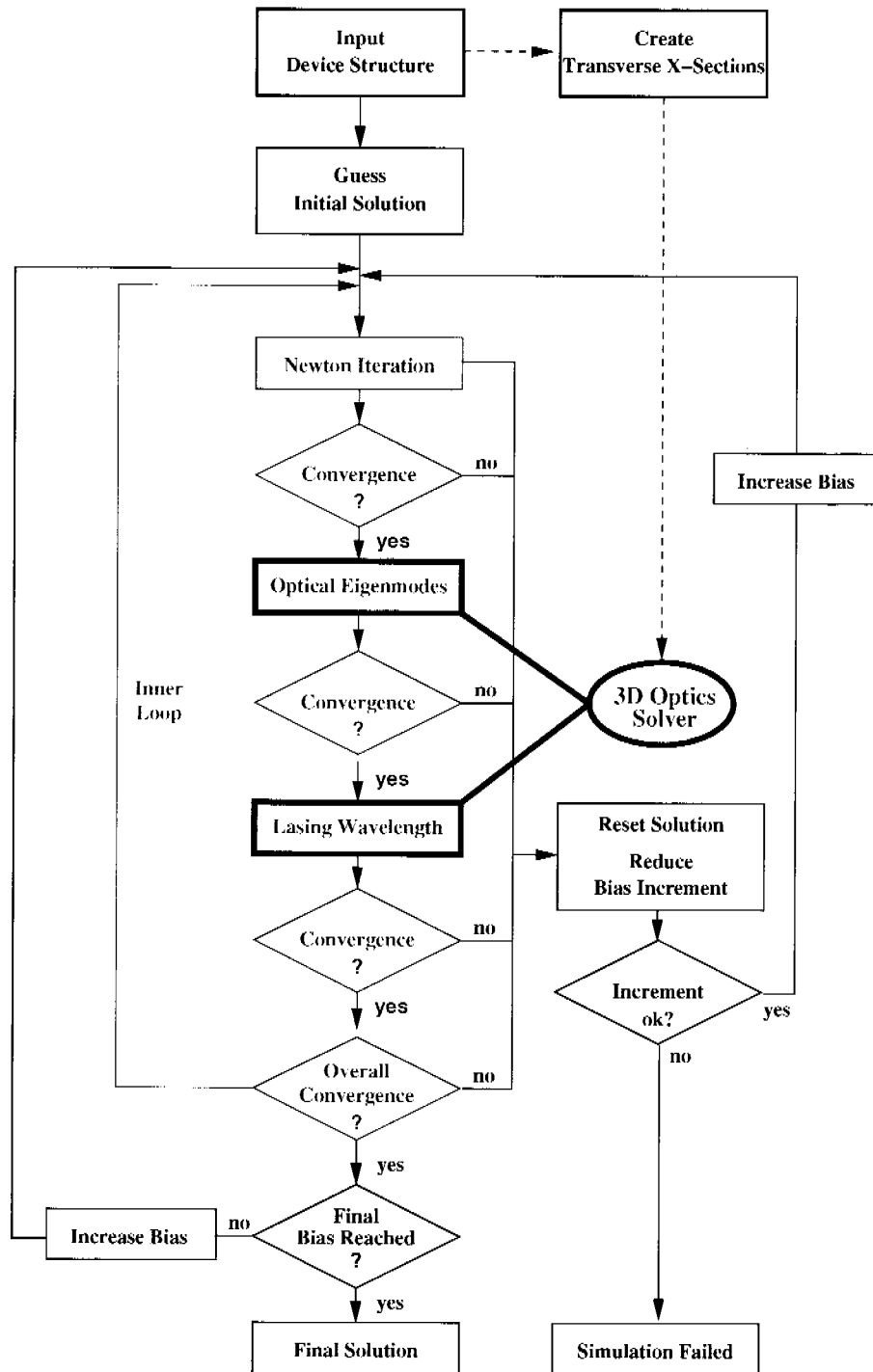


**Figure 3.4:** Simulation flow for a self-consistent simulation of tunable multisection DBR lasers in three dimensions. The flowchart of the 3D optics solver is shown in Fig. 3.3.

errors with respect to the last Newton iteration in the case of the coupled PDEs and to the respective solution of the previous Gummel-type iteration step for the other parts.

### 3.4 Problem-Specific Adjustments

In this section, some issues are addressed, which arise in the simulation of the tuning behavior of specific laser structures. As mentioned earlier, several currents have to be controlled simultaneously to achieve optimal device performance. How this can be handled in device simulations that are to be compared to measurements is discussed in the first part. What follows is a short review of the numerical difficulties involved and how they can be overcome. At last, a *resonance tracking* scheme is summarized that can speedup the solution of the longitudinal cavity problem in consecutive iterations within the inner loop shown in Fig. 3.4 and in successive bias points.

#### Mode Control and Tuning

While the solution scheme described in the previous section works well for many laser structures, tunable multisection DBR-type lasers sometimes require a modified solution strategy. They are different in that the lasing wavelength is determined not only by the effective cavity mode with the highest gain, as in Fabry–Perot lasers, but also by the overlap with the continuous grating reflectivity spectrum. In this mechanism, the waveguide phase plays a crucial role. Therefore, DBR lasers usually contain a phase-shifter section, which allows for the independent control of the cavity mode locations and, hence, a quasi-continuous tuning behavior.

In order to exploit the optimal wavelength tuning behavior, careful adjustment of the phase section current is necessary. In real-world applications, this can be done either interactively or by an electronic control loop calibrated through an extensive device characterization process. For obvious reasons, neither of them is an option for a device simulator. The approach chosen in this work involves the following tasks at each bias step:

- Calculate the front and rear mirror reflectivity spectra  $r_0(\omega)$  and  $r_1(\omega)$ .
- Determine the frequency  $\omega_0$  for which the product of the mirror reflectivities  $R(\omega) = r_0(\omega) \cdot r_1(\omega)$  has a global maximum.

- Take the frequency  $\omega_0$  as input to Eq. (2.29) and perform a two-dimensional root search with respect to  $(\Delta n'_{ph}, \Delta\alpha)$ , where  $\Delta n'_{ph}$  denotes the real part of the refractive index change in the phase section.
- Keep  $\Delta n'_{ph}$  fixed and calculate the remaining longitudinal side modes.

This ensures the alignment of the comb-mode spectrum with the reflectivity peak. The required index change in the phase section that is calculated can then be used to extract the corresponding change in the injection current.

In three-section DBR lasers, a suitable change in both the Bragg wavelength and the phase simultaneously enables tuning the emission wavelength continuously, while maintaining the same longitudinal mode [91]. This operating scheme can be put into practice by applying the injection current from a single source through an appropriate dividing resistor to each electrode. Since the device simulator DESSIS also supports mixed-mode simulations, a single device with a circuit netlist, it is possible to match the exact experimental setup for this case. A corresponding simulation example can be found in Section 4.3.

For widely tunable lasers such as the SGDBR, the external circuits are usually more complex and often rely on some feedback mechanism. For example, the optical output power can be monitored in order to adjust the gain section current for smooth, constant-power tuning operation. The implementation of these schemes, however, goes beyond the scope of this thesis.

### Damped Gummel-Type Iteration

The standard Gummel-type iterations as described in Section 3.3 do not always succeed and a modification to the existing scheme had to be implemented to ensure numerical stability. In certain simulation configurations of SGDBR lasers, the sensitivity of the waveguide phase with respect to the carrier density and temperature distributions can cause an oscillation between either adjacent cavity modes or adjacent channel modes<sup>10</sup> in consecutive iterations of the Gummel loop. This effect is due to numerical errors, for example, interpolation errors, and can be alleviated with a damping of the optical modes in the iteration scheme when the relative error has decreased to the point where the oscillatory behavior begins. Earlier on it is referred

---

<sup>10</sup>For a description of possible competing modes in an SGDBR laser, see [85].

to this as a *modified* Gummel-type iteration. The approach has proven to be very robust, and only three inner loop iterations per bias point on average are necessary until convergence is reached. Without this adjustment, the average number of iterations when injecting current into the mirror sections approximately doubles at best and, at numerically critical points, simulations will fail.

### Resonance Tracking

As described in Section 3.2.2, the solution of the longitudinal cavity problem by means of a transfer-matrix method (TMM) results in a complex root search. In typical DBR-type lasers, many closely spaced resonances can be found. For a multimode simulation, usually only two side-modes are relevant owing to the high loss of the remaining modes. Since there is no efficient method available that can directly solve for the  $n$  lowest-loss resonances, an accurate initial guess of the frequency has to be provided. Specifying a target loss is less crucial because there are no pairs of resonances that have the same frequency.

With no prior knowledge about the locations of the relevant resonances, one has no choice but to *scan* the frequency range of interest by using densely spaced starting points and then select the eigenvalues with the lowest loss—a procedure common to all root-finding methods including the nonlinear simplex method [88] used here.<sup>11</sup> It can be accelerated if it is assumed that the system to be solved is only slightly perturbed with respect to the one from the previous Gummel-type iteration or even the one from the previous bias point.

Under this condition, it is possible to restrict the starting points to neighborhoods of the previous solutions, thus drastically reducing the total number of search instances. In defining a strict acceptance criteria for the thereby found solutions, one can prevent nonphysical mode hops. In this work, a relative error criterion for the frequency and loss for each mode has to be met; otherwise, the solutions are discarded and a full scan is triggered.

Typically, the error criteria are met during successive Gummel-type iterations and between bias points where lasing occurs at the same cavity mode. Therefore, the more time-consuming full scan mode only needs to be

---

<sup>11</sup>Due to its geometrical foundation, this algorithm actually requires three starting points, which form the initial simplex in two dimensions. In practice, only one is needed as the others are generated automatically.

applied in wavelength regions where cavity-mode and channel-mode transitions occur, which keeps the computational effort of the longitudinal mode solver to a minimum for both the three-section DBR and the SGDBR laser.

Seite Leer /  
Blank leaf



# Chapter 4

## Simulation Examples and Calibration

### 4.1 Overview

The physical models and their numerical implementation in the general-purpose device simulator DESSIS, described in the previous two chapters, allow for the comprehensive simulation of a wide range of semiconductor lasers. In the following, three representative tunable laser structures from Table 1.1 on p. 10 are discussed in more detail. Simulations are carried out in one, two and three spatial dimensions depending on the complexity of the underlying device structure and the respective goal of the analysis.

In the first example, the efficiency of 2D isothermal simulations for the design and optimization of a tunable twin-guide (TTG) DFB laser is demonstrated. Several different device structures are investigated with respect to their maximum tuning range and output power, and the results are compared to experimental data. This example underlines the need for the self-consistent reiteration of the electro-optical equations and the calculation of the optical eigenmodes even in 2D simulations.

A tunable three-section DBR laser is the subject of the subsequent example, which outlines a multidimensional calibration approach. By performing electrothermo-optical simulations of a transverse cut through the gain section, a calibrated/consistent set of material parameters is obtained, which

is then used in 3D simulations to explore the wavelength tuning behavior. Computationally challenging thermal simulations in three dimensions are also covered in that section.

The most complex device structure covered in this thesis—a widely tunable sampled-grating distributed Bragg reflector (SGDBR) laser—is investigated in the last example. First, the simulator is benchmarked with measurements and another simulator. Then, the characteristic tuning behavior is demonstrated in 3D simulations and compared to experimental data<sup>1</sup>. At the end of each of the three examples, a short summary of the simulation statistics is given.

All of the examples mentioned above show that the simulator is capable of qualitatively predicting the respective device behavior. In certain cases even a quantitative agreement with measurements is reached, which is a challenging task especially due to the time- and memory-consuming nature of 3D simulations.<sup>2</sup>

Finally, the last section in this chapter is dedicated but not limited to the potential user of the simulator presented in this thesis. A practical guide to 3D simulation of multisection lasers for both isothermal and non-isothermal analyses discusses issues related to the simulation setup. These include structure and mesh generation as well as input files and performance optimization.

## 4.2 Tunable Twin-Guide DFB Laser

In the following, a 2D analysis of a transversely integrated tunable laser diode, first proposed by Amann and coworkers [12], is performed. Several aspects of device optimization are highlighted by simulations, which reproduce experimental data. This example illustrates the power of numerical device modeling in the development and optimization process: The effect of varying the thickness and doping concentration of several layers simultaneously can be studied in a matter of hours.

---

<sup>1</sup>The SGDBR structure and measurements are provided by courtesy of the University of California, Santa Barbara (UCSB).

<sup>2</sup>For extensive calibration efforts of other types of laser using the device simulator DESSIS, the reader is referred to published work of collaborators [43, 92, 93].

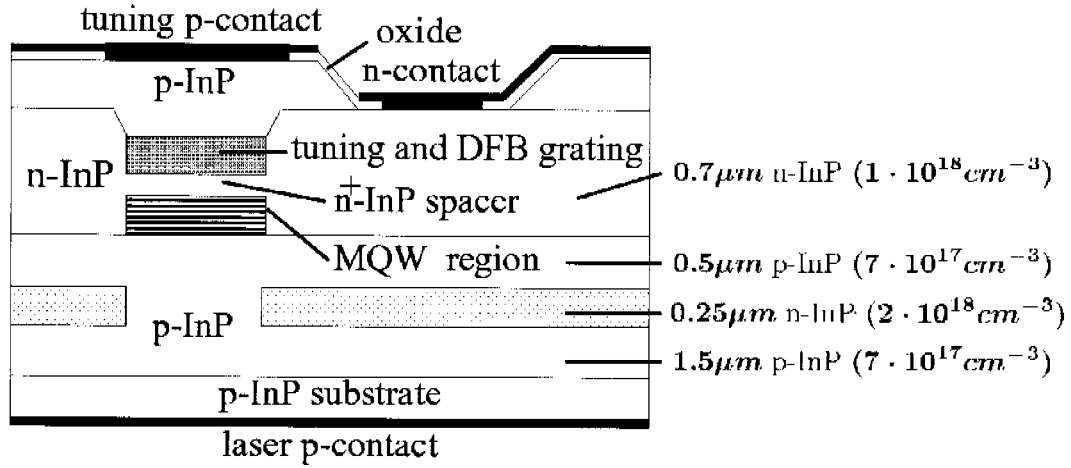


**Figure 4.1:** Schematic cross-section of the buried-heterostructure (BH) ridge TTG laser diode for  $1.55\mu\text{m}$  wavelength emission [13].

### 4.2.1 Introduction

The TTG DFB laser discussed in this example is based on the structure presented in [13, 94, 95]. Fabricated in the InGaAsP–InP material system, it emits light in the  $1.55\mu\text{m}$  telecommunications wavelength range. A buried pnp-heterostructure whose highly doped n-layer is laterally connected to an n-contact characterizes the electronic behavior of the device. The hole currents originating from the p-contacts at the top and bottom, as shown in Fig. 4.1, control the electron flow into the intrinsic low-bandgap active and tuning regions. In this way, it is possible to bias the active and tuning pn-heterojunction diodes independently and, thus, decouple the control of the lasing action from the tuning behavior.

The high-index twin-guide is responsible for the strong optical coupling between the active and tuning regions. By changing the refractive index in the tuning region, the lasing mode can be influenced. To guarantee longitudinal single-mode operation, a distributed feedback (DFB) grating is incorporated into the top guide. As a result, the lasing wavelength is given by<sup>3</sup>

$$\lambda = \lambda_B = 2\Lambda n_{\text{eff}}, \quad (4.1)$$

<sup>3</sup>Lasing is assumed to occur at the Bragg wavelength.

where the effective mode index

$$n_{\text{eff}} = \Delta n_{\text{eff},a} + \Delta n_{\text{eff},t} \quad (4.2)$$

can be thought to have two components: one is attributed to the refractive index change in the active region,  $\Delta n_{\text{eff},a}$ , and the other is due to the index change in the tuning region,  $\Delta n_{\text{eff},t}$ . The weight of the respective index change is given by the optical confinement factor of the corresponding region. As can be seen later, it is essentially the ratio between the two confinement factors,  $\Gamma_a$  and  $\Gamma_t$ , which determines if the laser has been optimized with respect to maximum tuning range or maximum output power.

The TTG DFB structure allows for both electronic and thermal tuning depending on whether the tuning contact is operated under forward or reverse bias. A total continuous tuning range in the order of 10nm has been achieved [13, 94]. Here, we consider only the former since it is generally preferred due to its faster tuning speed and better power efficiency. The electronic tuning mechanism is based on the change in refractive index due to carrier injection into the tuning region [60] which leads to a decrease in laser wavelength. To prevent stimulated recombination in the tuning region, its bandgap wavelength is chosen at  $\lambda_g = 1.3\mu\text{m}$ , well below the wavelength of the laser light.

At increased laser currents and temperatures, common TTG laser diodes without blocking regions suffer from current leakage around the active region especially due to the wide pn-homojunction underneath the n-contact [95]. This limitation can be overcome by introducing a pnpn-blocking region laterally aligned with the active region as shown in Fig. 4.1.

A detailed description of the device fabrication and its parameters is given in [94]. The active multi-quantum-well region consists of seven 0.8% compressively strained InGaAsP quantum wells and is embedded between p-doped separate confinement heterostructure (SCH) layers. All simulations assume a cavity length of  $400\mu\text{m}$  and a stripe width of  $1.5\mu\text{m}$ .

### 4.2.2 Tuning Range versus Output Power

Inherent to the TTG design is that the tuning range and the output power cannot be optimized independently. The tuning range can be extended by increasing the tuning layer thickness. However, this implies a reduction of the optical confinement factor of the active region and, ultimately, limits the output power.

Laser Diode	no. 1	no. 2	no. 3
Tuning Region Thickness[ $\mu\text{m}$ ]	0.3	0.15	0.3
$n^+$ -InP Spacer Thickness[ $\mu\text{m}$ ]	0.1	0.16	0.1
BBR Technology	no	no	yes
Tuning Range (Forward Bias) [nm]	4.5	1.5	4.5

**Table 4.1:** Laser simulation parameters for three representative structures, which are optimized with respect to maximum tuning range (diode no. 1) and maximum output power (diode no. 2). Laser diode no. 3 excels in both fields due to the incorporation of a buried blocking region.

Simulations of laser diodes with different thicknesses of tuning and  $n^+$ -InP spacer layers ranging from 0.15–0.3  $\mu\text{m}$  and 0.1–0.16  $\mu\text{m}$ , respectively, have been performed. Two representative structures as specified in the parameter Table 4.1 demonstrate this behavior. The simulation results are shown in Figs. 4.2 and 4.3. Laser diode no. 1 (blue and black curves) has a wide tuning range but the slope of the light output power is reduced, whereas the opposite holds for laser diode no. 2 (green curves). The resulting tuning ranges of 4.5nm for diode no. 1 and 1.5nm for diode no. 2 closely match measurements given in [94]. The same also holds for the respective threshold currents, while the slope efficiencies are slightly overestimated especially at higher injection currents.

The discrepancy between the measured and simulated output power can be explained by self-heating effects, which are present in a continuous wave (CW) measurement setup but cannot be analyzed in isothermal simulations. For a more accurate comparison, pulsed instead of CW measurements should be used<sup>4</sup>. However, thermal effects arising under CW operation are best analyzed in non-isothermal simulations using the thermodynamic model. Furthermore, technological effects such as the sidewall roughness of the stripe due to the etching and regrowth process are difficult to determine on a microscopic level and are generally hard to quantify. The associated recombination leads to a further reduction of the output power compared with an ideal structure underlying the simulations.

---

<sup>4</sup>Pulsed measurements were not available at the time of publications.

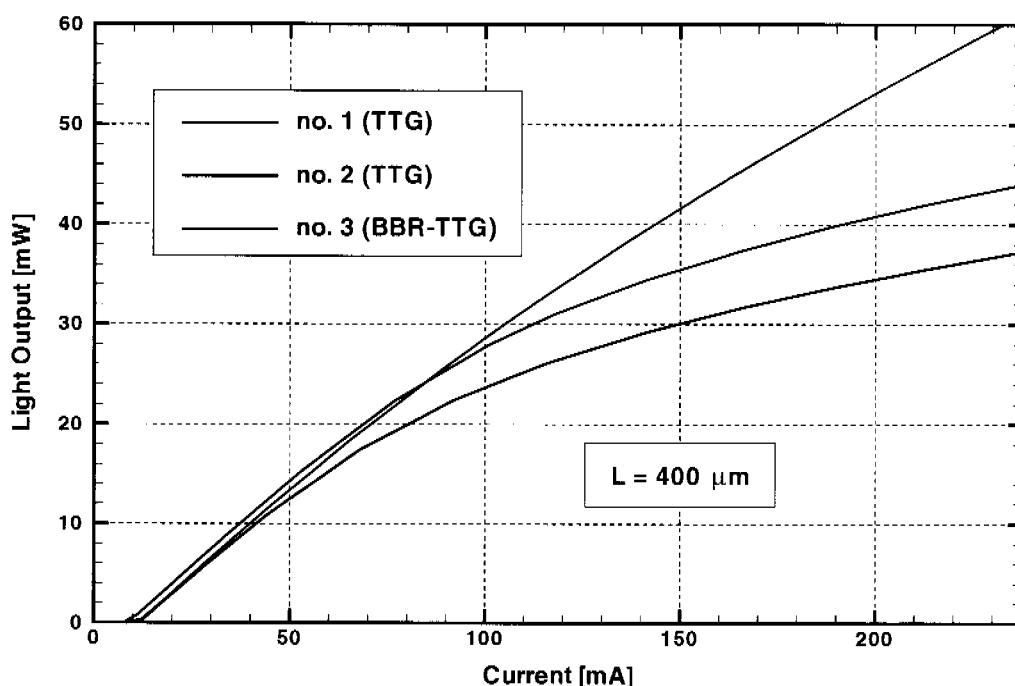


**Figure 4.2:** Light output versus laser current characteristics of three different BH TTG laser diodes specified in Table 4.1 with emission wavelength around  $1.55\mu\text{m}$ .

### 4.2.3 Power Optimization

Crucial to good device performance is the confinement of the injection current to the active quantum-well region. It should be noted that the slope efficiency for laser diode no. 1 and no. 2 decreases for injection currents above 60 mA. The authors of [13, 94] have reported that the TTG laser diode suffers from current leakage through the pn-homojunction underneath the n-contact.

As a remedy, a pnpn buried current-blocking region has been successfully incorporated into the TTG design [13, 94], as illustrated in Figs. 4.1 and 4.4. The maximum output power of the buried blocking region (BBR) TTG laser is increased by approximately 150% with almost constant slope efficiency of  $0.18\text{ W/A}$ . The effect of current leakage (suppression) is shown in the top (bottom) current flow plot of Fig. 4.4. The streamtraces of the current density vector field illustrate the influence of the current blocking region. For the BBR TTG structure (bottom), the current flow is mainly directed into the active region while it is split into two equally weighted branches for the TTG laser diode no. 1 (top). Note that the resulting current

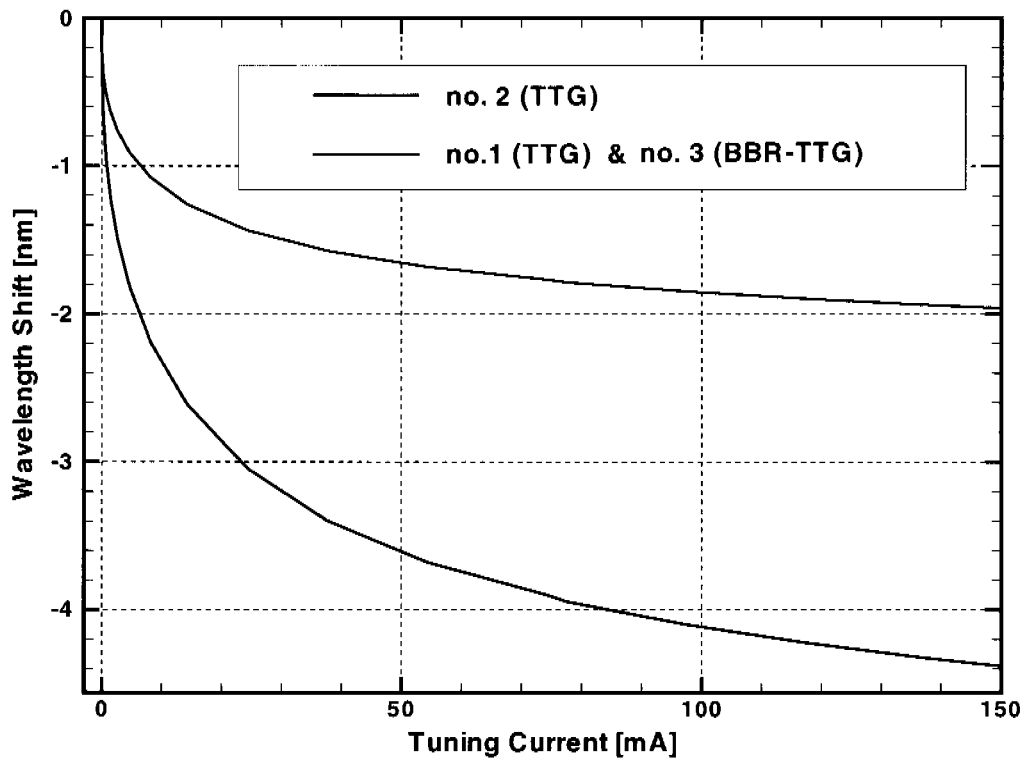


**Figure 4.3:** Wavelength tuning characteristics under forward bias of TTG lasers no. 1, 2 and BBR TTG laser no. 3. The reduced optical confinement factor of the tuning region in diode no. 2 leads to an increase of the output power at the cost of a smaller tuning range compared to diode no. 1.

crowding around the blocking region of the BBR TTG laser is clearly visible in the bottom plot.

It has been observed that an exact lateral alignment between the active region and the current confinement structure is necessary to realize TTG laser diodes with improved performance [13]. Figure 4.5 shows the LI-curve for three different distances  $\Delta$  from the ridge sidewall to the n-blocking region, which indicate that tendency. For low current densities, the slope efficiency is independent of  $\Delta$ . At elevated current densities, however, the blocking structure becomes less effective for  $\Delta > 0$ .

#### 4.2.4 Discussion

##### Optical Near and Far Field

Since the optical field pattern is updated self-consistently in the presented simulation methodology, simulations reveal the response of the fundamental transverse mode pattern to the refractive index change induced by the injection of the electron and hole plasma into the tuning region. It can be seen from Fig. 4.6 that during the tuning operation the transverse near-field distribution is displaced from the tuning layer towards the active layer. This is due to the reduction of the refractive index in the former layer under forward bias, which leads to a change of the ratio of the active and tuning region confinement factors  $\Gamma_a$  and  $\Gamma_t$ . At threshold,  $\Gamma_a/\Gamma_t = 0.18$ , and at maximum tuning current,  $\Gamma_a/\Gamma_t=0.19$ . Figure 4.7 shows the lateral and transverse far-field pattern, whose full-width half-maximum (FWHM) values range between  $38^\circ$  and  $40^\circ$  at an emission wavelength of  $1.55\mu\text{m}$ . The values for the optical twin-guide structure are larger than for standard BH lasers because of the increased total thickness of the waveguide layers and the resulting higher effective mode index. Simulations closely match measurements reported in [94, 96].

##### Auger Recombination in the Tuning Region

A major limitation to the maximum tuning range is the heat generation in the tuning region, which results in an increase of the laser wavelength and counteracts the intended negative wavelength shift caused by carrier injection. For improving the tuning efficiency  $\eta_t = |d\lambda/dI_t|$ , it is necessary to obtain a maximum change of the charge carrier density with minimum tun-



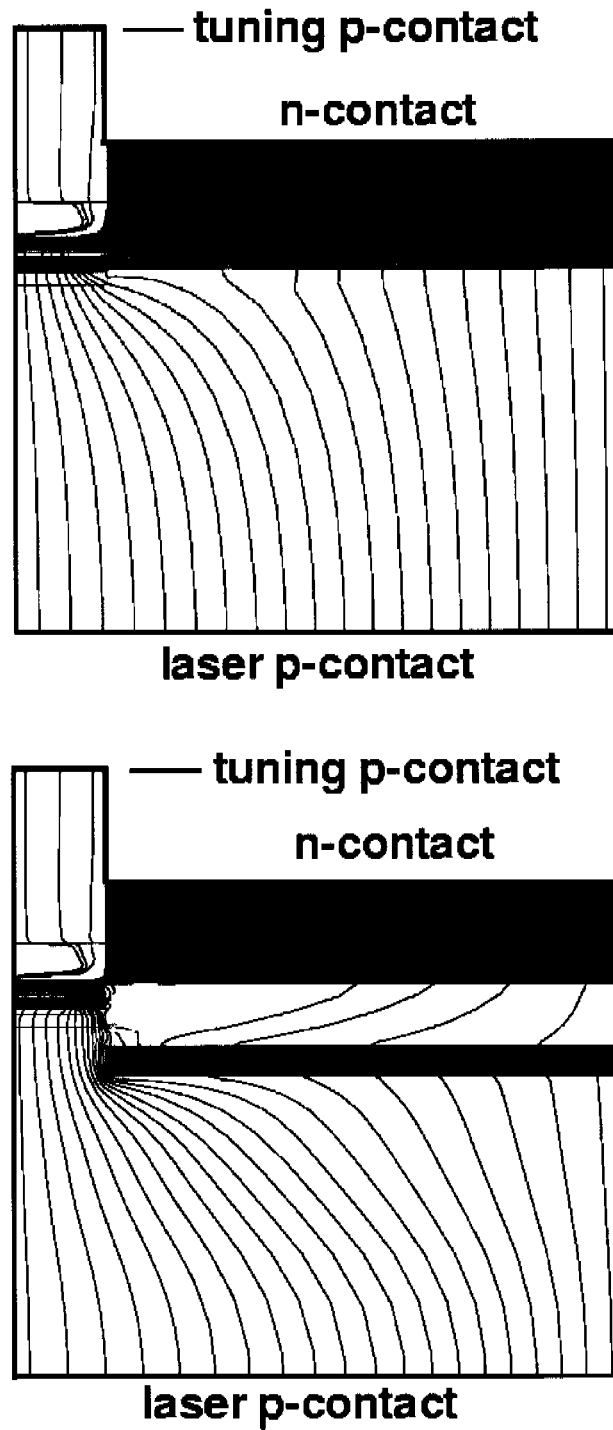


**Figure 4.4:** Comparison of the current density vector flow between TTG laser diode no. 1 (top) and BBR TTG laser diode no. 3 (bottom) at bias condition  $I_{\text{Laser}} = 150\text{mA}$ . The streamtraces of the current density vector field illustrate the effect of the current blocking region.

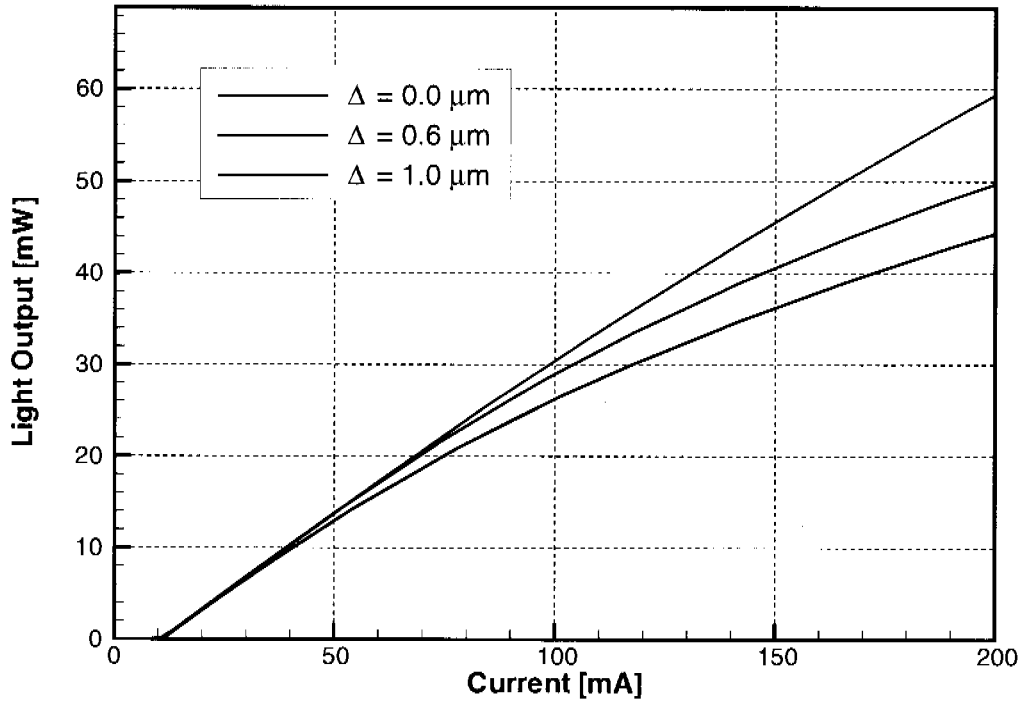


**Figure 4.5:** Dependence of the light output power on the displacement  $\Delta$  of the n-blocking region from the ridge sidewall.

ing current. However, the nonlinear recombination law, especially Auger recombination, makes this difficult. In Fig. 4.8, Auger recombination is shown along a vertical cut through the ridge for very low and high tuning currents.<sup>5</sup> It is evident that the tuning region experiences a dramatic increase in Auger recombination. To overcome this limitation, a type-II superlattice to spatially separate electrons and holes from each other has been proposed [97].

## Conclusions

In conclusion, a 2D analysis of a continuously tunable BH TTG DFB laser diode has been carried out to optimize the device structure with respect to maximum tuning range and light output power. The importance of the exact lateral alignment of the current blocking region and the limitation to the tuning efficiency due to Auger recombination has been demonstrated. Moreover, the influence of tuning on the optical far field has been investigated. Overall, several different representative structures have been dis-

<sup>5</sup>The Auger coefficient in the simulation was chosen as  $C = 2 \cdot 10^{-29} \text{cm}^6/\text{s}$ .

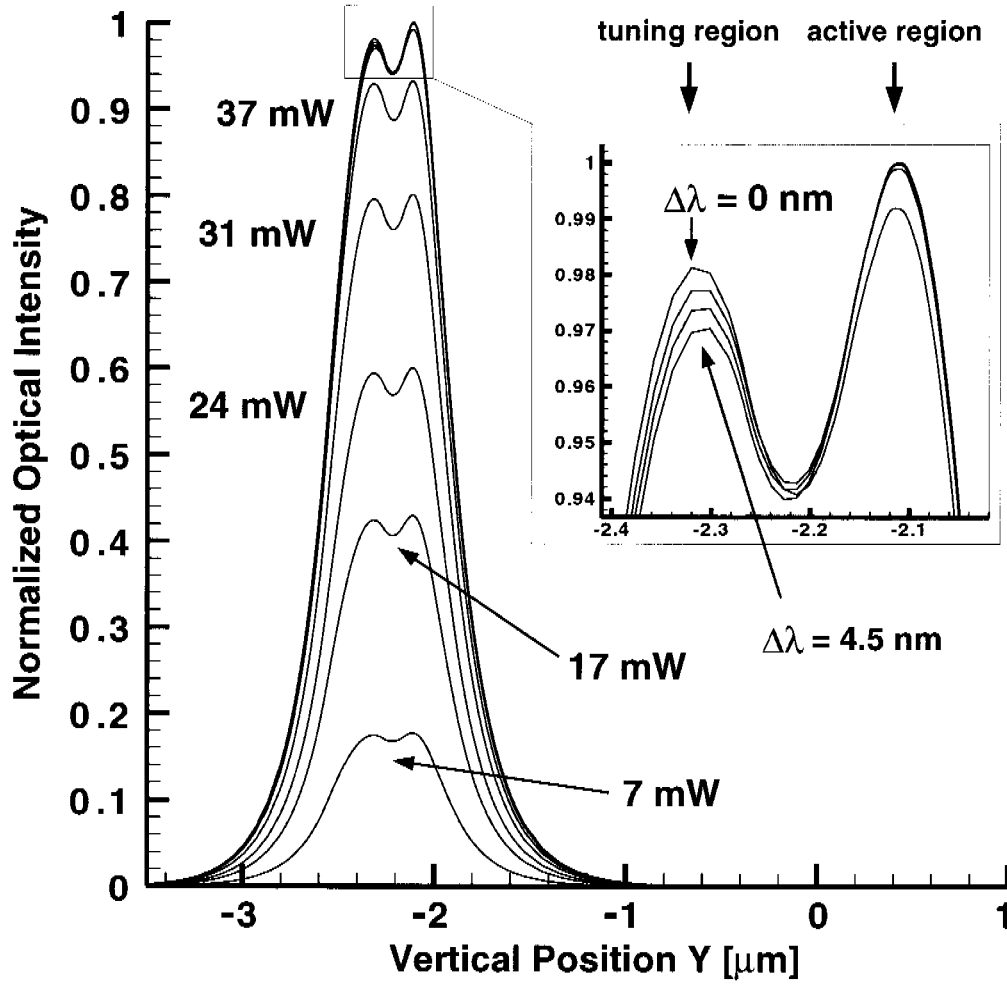


**Figure 4.6:** Transverse optical near-field distribution for BBR TTG laser diode no. 3 at different laser and tuning biasing conditions. The inset shows the displacement of the field distribution from the tuning towards the active layer during tuning.

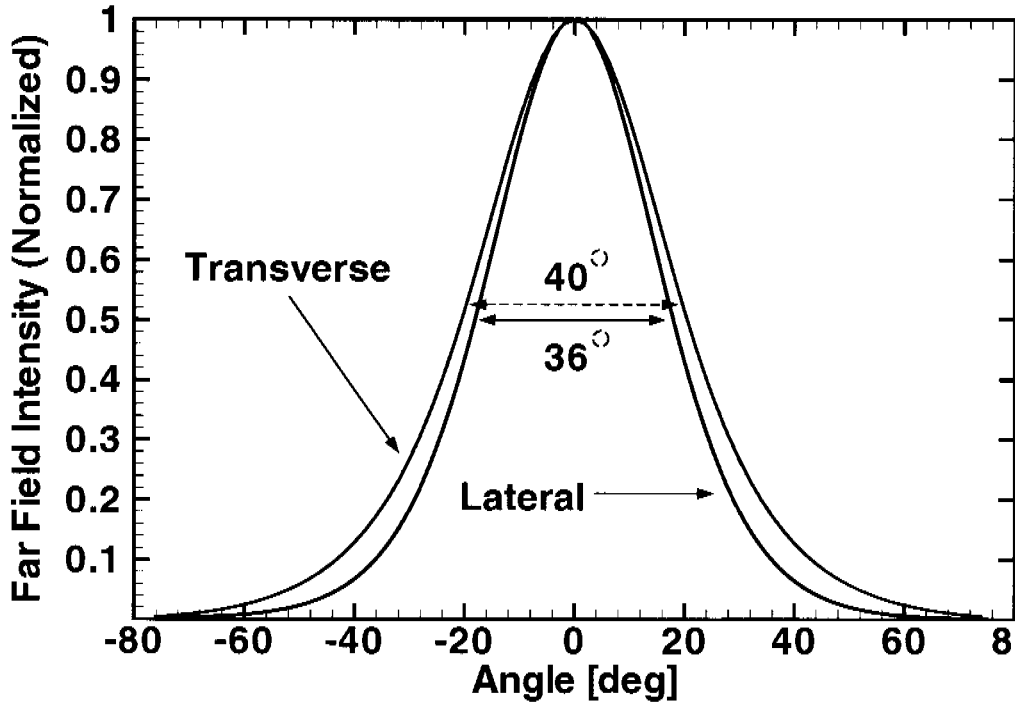


**Figure 4.7:** Transverse optical far-field distribution for BBR TTG laser diode no. 3 at maximum light output power.

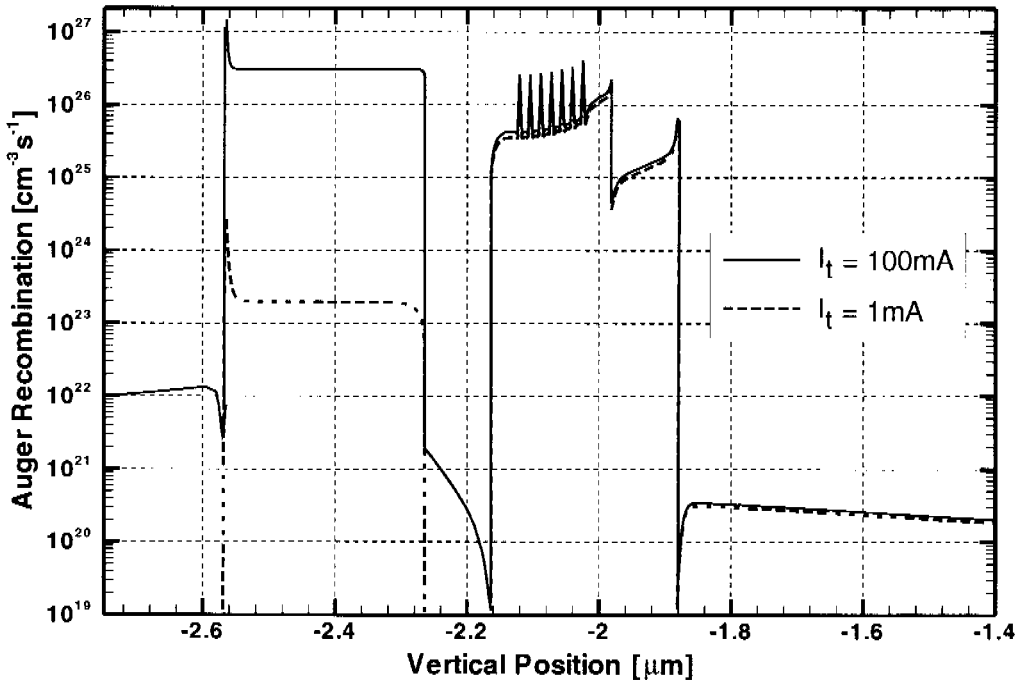


**Figure 4.8:** Auger recombination along a vertical cut through the ridge for tuning currents  $I_t = 1\text{mA}$  (blue curve) and  $I_t = 100\text{mA}$  (red curve). The graph shows a zoom into the tuning (left) and active (right) regions.

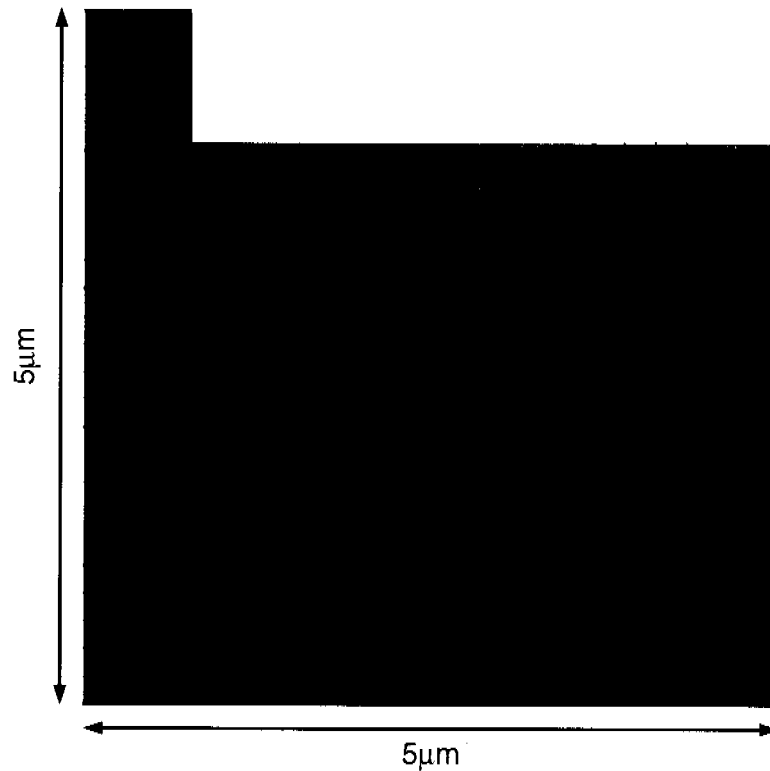


**Figure 4.9:** Simulation mesh of a BBR TTG laser.

cussed and the simulation results closely reproduce experimental characteristics. A thermal analysis is still outstanding and would be particularly interesting in a 3D study of the SG TTG laser—the widely tunable successor of the TTG DFB laser.

#### 4.2.5 Simulation Statistics

Compared with standard FP edge-emitting lasers, the epitaxial layer structure of TTG lasers is complex. Resolving the optical twin-guide, the buried-stripe sidewall and the pnpn blocking region as shown in Fig. 4.9 leads to approximately 12k mesh vertices, which is at the high end for typical two-dimensional simulations. To obtain the laser characteristics presented in Figs. 4.2 and 4.3, 500MB of memory and approximately 30min CPU time are required on a SuperMicro 6022CB, 2.2 GHz Intel Xeon.

### 4.3 Three-Section DBR Laser

Comprehensive multidimensional DBR laser simulations are presented in the following as part of a hierarchical calibration approach. It consists of a 2D analysis to calibrate simulation parameters that are related to the transverse epitaxial layer structure. These parameters are then used in isothermal 3D simulations to investigate the characteristic tuning behavior of three-section DBR lasers. The highest hierarchy level—non-isothermal simulations in full three dimensions—demonstrates the potential of this calibration approach.

#### 4.3.1 Introduction

The DBR laser under investigation consists of three longitudinally integrated waveguide sections: an active section provides the optical gain for the laser operation, a passive phase shift section, which contains neither gratings nor active material, and a DBR mirror section. As such, this structure is one of the simplest representatives for longitudinally integrated devices such as widely tunable laser diodes.

To illustrate the calibration approach, one of the the early successful realizations of a tunable multisection DBR laser [18, 91, 98, 99, 100] is chosen as shown schematically in Fig. 4.10. It consists of gain, phase and Bragg sections with respective lengths of  $400\mu\text{m}$ ,  $60\mu\text{m}$  and  $350\mu\text{m}$ , which are separated by  $20\mu\text{m}$  isolation grooves. The lateral structure is the semi-insulating planar buried-heterostructure (SIPBH) geometry described in [101], and the transverse and longitudinal designs follow the device investigated in [99]. However, the active InGaAsP MQW region had to be replaced by a bulk active region according to [101]. At the time of this project, the 3D module of the mesh engine was not capable of fulfilling the constraints imposed by the three-point model for quantum wells<sup>6</sup>.

#### 4.3.2 Calibrated Electrothermo-Optical Simulation

One of the major building blocks of the multisection DBR laser introduced in Section 4.3.1 is the  $400\mu\text{m}$  long gain section. Before proceeding to three

---

<sup>6</sup>In the course of this thesis, a special module, which overcomes this problem, has been implemented in the mesh generator *Noffset3D* by the author of [102]. It enables general 3D simulation of tunable MQW lasers as presented in Section 4.4 and Section 4.5.

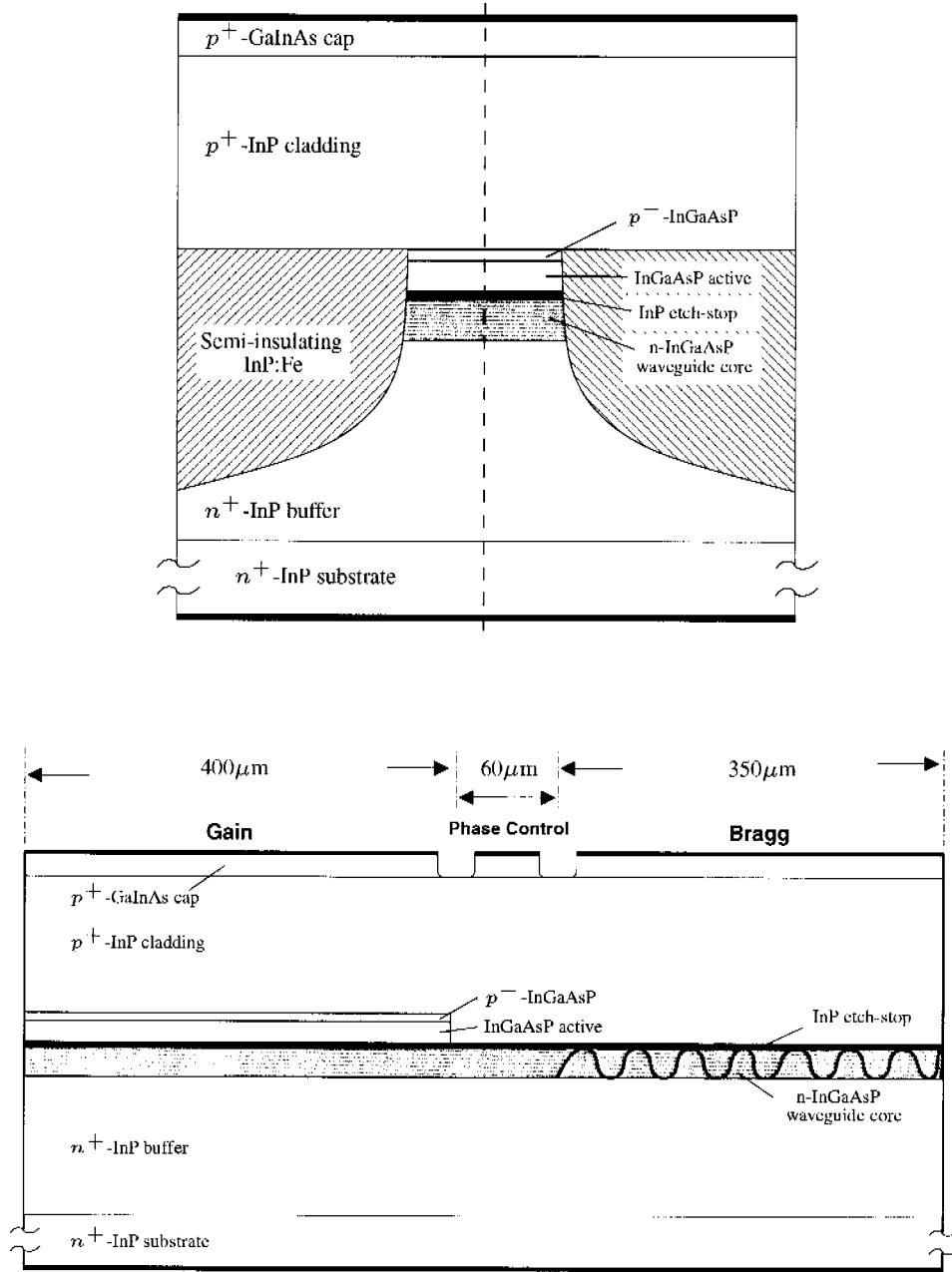


**Figure 4.10:** Schematic views of the transverse (top) and longitudinal (bottom) cross section of the multisection DBR laser investigated in this section. As shown on the top, the lateral structure is a semi-insulating planar buried-heterostructure (SIPBH) InGaAsP/InP geometry [99, 101]. The periodic corrugation of the waveguide core layer in the Bragg section is indicated by the wave train.

dimensions, a thorough understanding of the device characteristics can be obtained by performing 2D simulations of a transverse cut through the active section as depicted in Fig. 4.10. Assuming a Fabry–Perot cavity of length,  $L = 300\mu\text{m}$ , a comparison to the measurements shown in [101] is possible. Figure 4.11 shows the result of such a comparison for the light output power versus terminal current characteristics. The red curve has been obtained from a fully coupled electrothermo-optical simulation, where the internal loss  $\alpha_i$  and the temperature-dependent Auger coefficients  $C_{n,p}$  are assumed to be fitting parameters. The latter coefficients are modeled by a Taylor expansion up to second order in the scaled local temperature according to

$$C_{n,p} = A_{n,p} + B_{n,p} \frac{T}{T_0} + C_{n,p} \left( \frac{T}{T_0} \right)^2, \quad (4.3)$$

with  $T_0$  being the ambient temperature. Out of a large number of simulations, the best fit to experimental data [101] is shown in Fig. 4.11, with parameters  $A_{n,p}$ ,  $B_{n,p}$ ,  $C_{n,p}$  and  $\alpha_i$  taking values within the respective ranges reported in literature. These values were also taken to simulate the output power versus current characteristics of the laser at various ambient temperatures. The array of curves is shown in Fig. 4.12 and confirms the typical temperature dependence of the threshold current and the output power including the thermal rollover. The active region self-heating observed at an ambient temperature of  $15^\circ\text{C}$  at maximum power is  $\Delta T_{\text{active}} = 64\text{K}$ .

### 4.3.3 Wavelength Tuning and Thermal Analysis in 3D

Some unwanted effects such as longitudinal current leakage and the influence of the transition regions between the different sections of a multi-electrode DBR laser cannot be analyzed in two dimensions. In this simulation of the full three-dimensional structure, current is first injected into the gain section to drive the laser to its operating point. Then, current is injected into the Bragg and phase sections to tune the lasing wavelength.

#### Wavelength Tuning Behavior

In the previous example of the TTG DFB laser in Section 4.2, the tuning behavior could be approximated by assuming that lasing is to occur at the



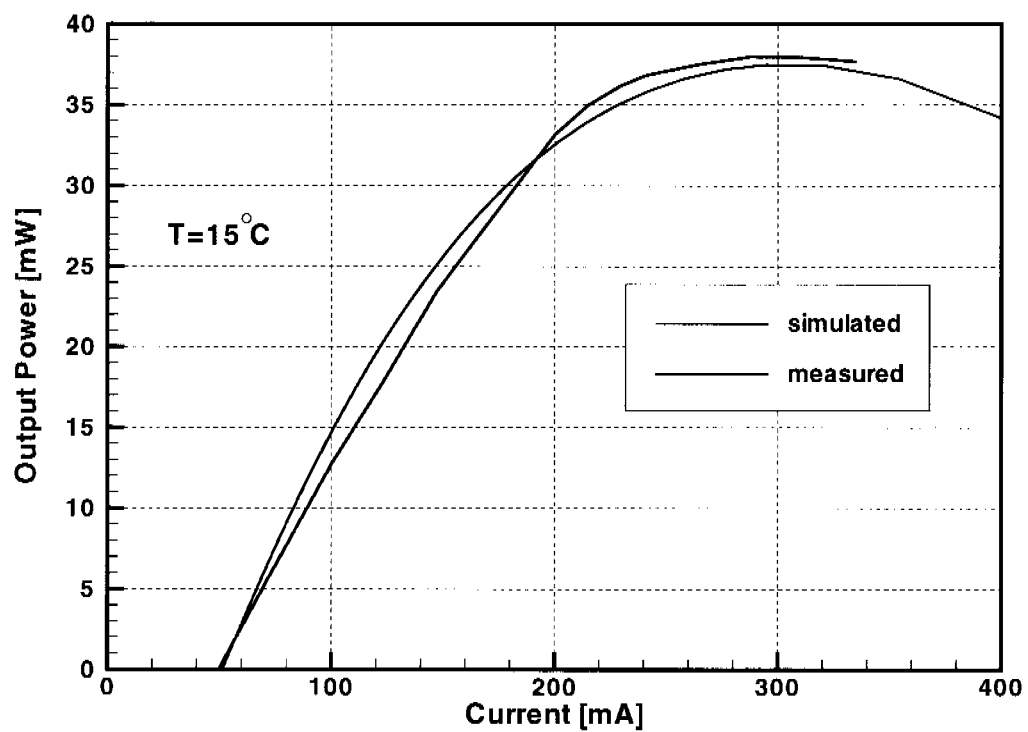


**Figure 4.11:** Simulated and measured optical output power versus terminal current characteristics. Simulations are in agreement with measurements [101].

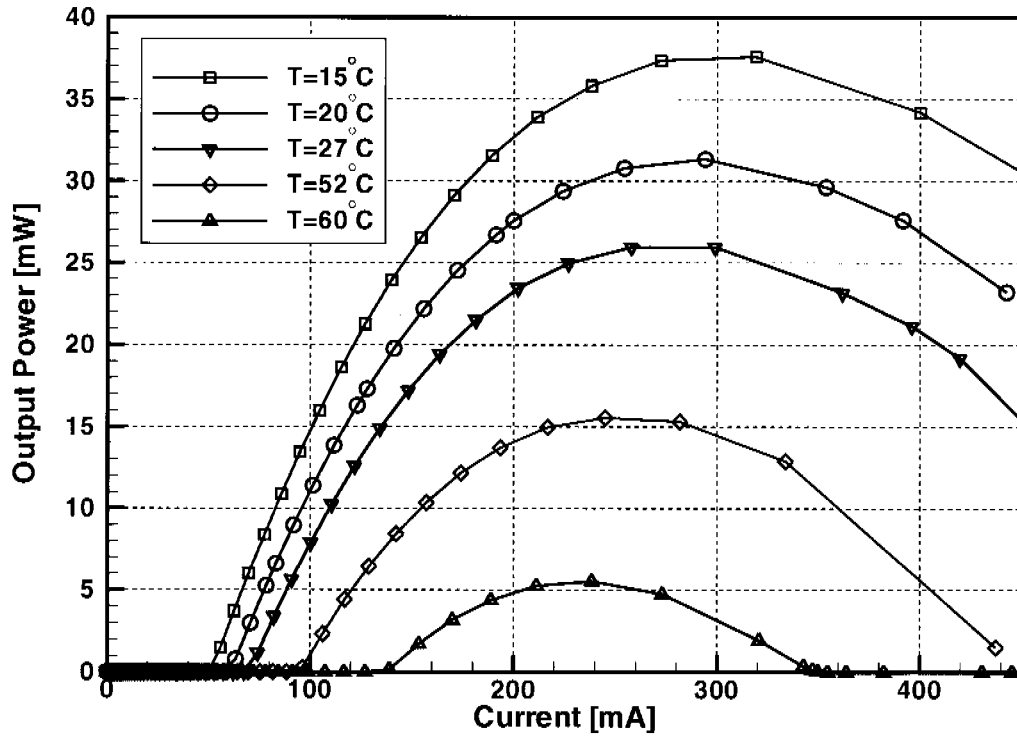


**Figure 4.12:** Optical output power versus terminal current characteristics for laser operating at various ambient temperatures. All results were obtained from fully self-consistent electrothermo-optical simulations of the gain cross section. The markers are placed at the positions where self-consistency has been achieved. Note the large step size even across the thermal rollover, which is due to the excellent numerical convergence.

Bragg wavelength,  $\lambda_B = 2n_{\text{eff}}\Lambda$ , where the effective mode index is determined by a volume integration<sup>7</sup> of the refractive index weighted with the optical mode pattern. This is possible because the grating extends through the whole cavity. In a multisection laser, the volume integration would have to be restricted to the Bragg section, which is feasible in 3D but not in 2D simulations, since in the latter only a transverse cut through the active region is calculated. However, even in three dimensions, the influence of the active and phase section on the lasing wavelength via the phase of the laser light traveling through the entire cavity would be neglected within this approximation.

In extending the simulation domain to three dimensions, it is possible to describe realistically the tuning behavior and to allow for a one-to-one comparison between model and experiment. Figure 4.13 shows the simulated light output and voltage as a function of the active region current  $I_a$  with no currents being injected into the remaining sections. Note that the reduced threshold current compared with the two-dimensional simulation in Fig. 4.11, at an ambient temperature of 27°C, is mainly due to the increased gain section length  $L_G = 400\mu\text{m}$ . The corresponding external quantum efficiency is 35%.

For wavelength tuning an operating point with current  $I_a = 100\text{mA}$  and output power  $P = 16\text{mW}$  is chosen. Figure 4.14 shows the simulated tuning characteristic when current is injected into the Bragg region only. As the DBR current is increased, the wavelength undergoes a blue shift with the characteristic periodic mode jumps. The simulation exhibits a total tuning range of approximately 10nm for a maximum tuning current of 150mA. With increasing tuning current, the wavelength plateaus become longer since a larger current change is needed to shift the effective mode index by an equal amount. Eventually, the tuning efficiency  $\eta_t = |d\lambda/dI_t|$  decreases significantly due to the nonlinear relationship between the tuning current and the carrier density.

A continuous tuning range can be realized by additionally controlling the phase section current. Whenever a mode jump is about to occur, current is injected into the phase section and the Bragg region current is held constant. In that way, the mode jumps can be bridged if the ratio of the section

---

<sup>7</sup>Volume integration is to be understood in the mathematical sense and, therefore, applies to two and three dimensions:  $n_{\text{eff}}^{2D} = \int_V n(x, y) |\Phi(x, y)|^2 dx dy$  and  $n_{\text{eff}}^{3D} = \int_V n(x, y, z) |\Phi(x, y, z)|^2 dx dy dz$ .

lengths and the Bragg grating are properly designed.

The above procedure is demonstrated in Fig. 4.15. In the simulation, the current in the DBR region is ramped up to 20mA during which the laser undergoes six mode jumps. At that point current is injected into the phase section. A maximum current of about 7mA is then needed to blue-shift the lasing wavelength by 1nm—a shift that is sufficiently large compared to the mode jump. The small negative value of  $I_p$  is due to the leakage current between the neighboring sections.

As the real part of the refractive index changes under current injection according to the free-carrier plasma effect, so does the imaginary part. The latter is tantamount to an additional optical loss, which affects the output power of the laser besides the decrease of the power reflectivity. Controlling a third current—the gain section current—the output power variation depicted in the bottom of Fig. 4.15 can also be compensated for [91]. Figure 4.15 also shows the slight decrease of the output power as the Bragg peak is detuned from the cavity mode.

To simplify the control of the tuning behavior, a circuit that connects the phase and DBR contact with fixed resistances can be applied to the device. As a result, only one tuning current needs to be controlled apart from the gain section current. Since the device simulator DESSIS supports a general circuit interface, it is also possible to perform a comprehensive device simulation with a control circuit configuration.

The injection of current into the three device sections causes carrier leakage into the adjacent regions as well as thermal crosstalk at elevated currents. The three-dimensional optical intensity and current density distribution resulting from an isothermal simulation is illustrated in Fig. 4.16. A zoom into the central region of the laser highlights inhomogeneities in the transition regions between the three device sections. Non-isothermal simulations revealing thermal effects are discussed in the following section.

### Thermal Analysis

Many important properties of common edge-emitting lasers can be studied reliably in one or two spatial dimensions, where the simulation domain usually represents the full transverse or longitudinal device cross section or a specific part thereof. Several authors have shown calibrated simulation results that included the study of thermal effects [103, 104, 105, 106].

The inclusion of thermal physics is computationally more demanding

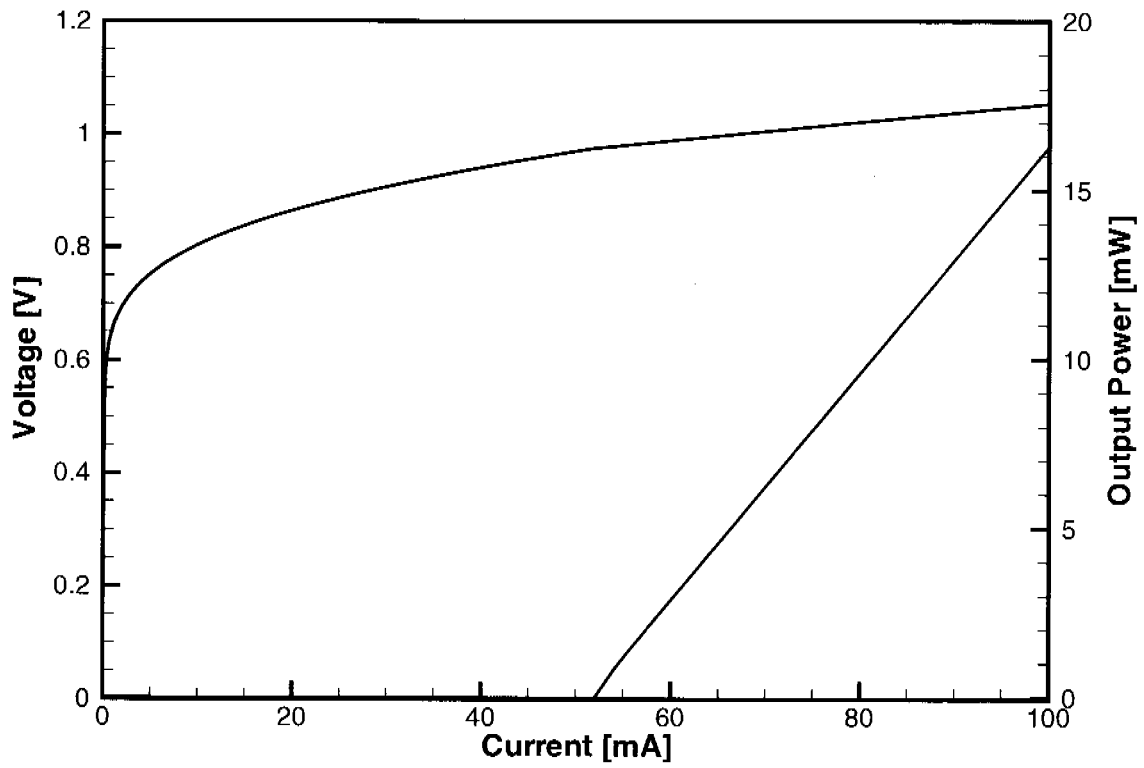


**Figure 4.13:** Voltage and output power versus current characteristics from a full-3D simulation of a three-section DBR laser at an ambient temperature of 27°C. At a gain section current  $I_g = 100\text{mA}$ , the wavelength of the laser is tuned as shown in Figs. 4.14 and 4.15.

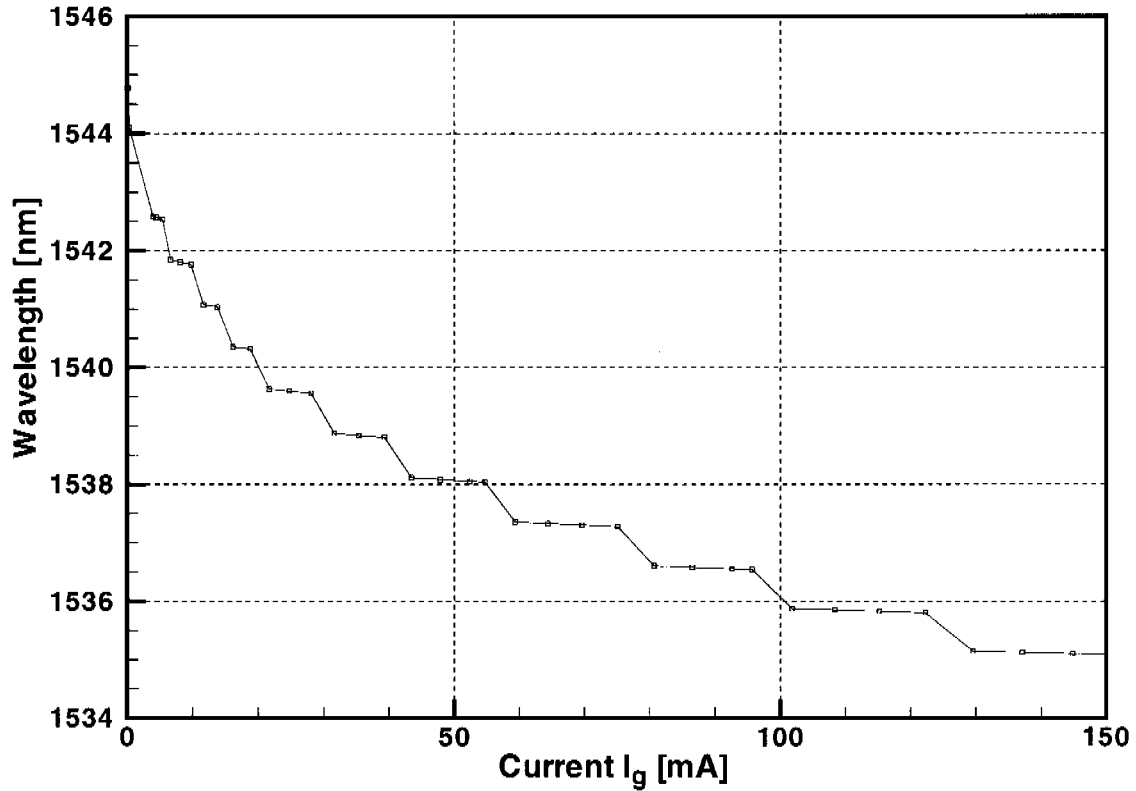


**Figure 4.14:** Simulated wavelength tuning behavior as current is injected into the DBR grating section. The periodic mode jumps are due to the Bragg peak being shifted across the cavity-mode spectrum. Self-consistent solutions of the quasi-stationary electro-optical laser equations at several bias points are indicated by markers.

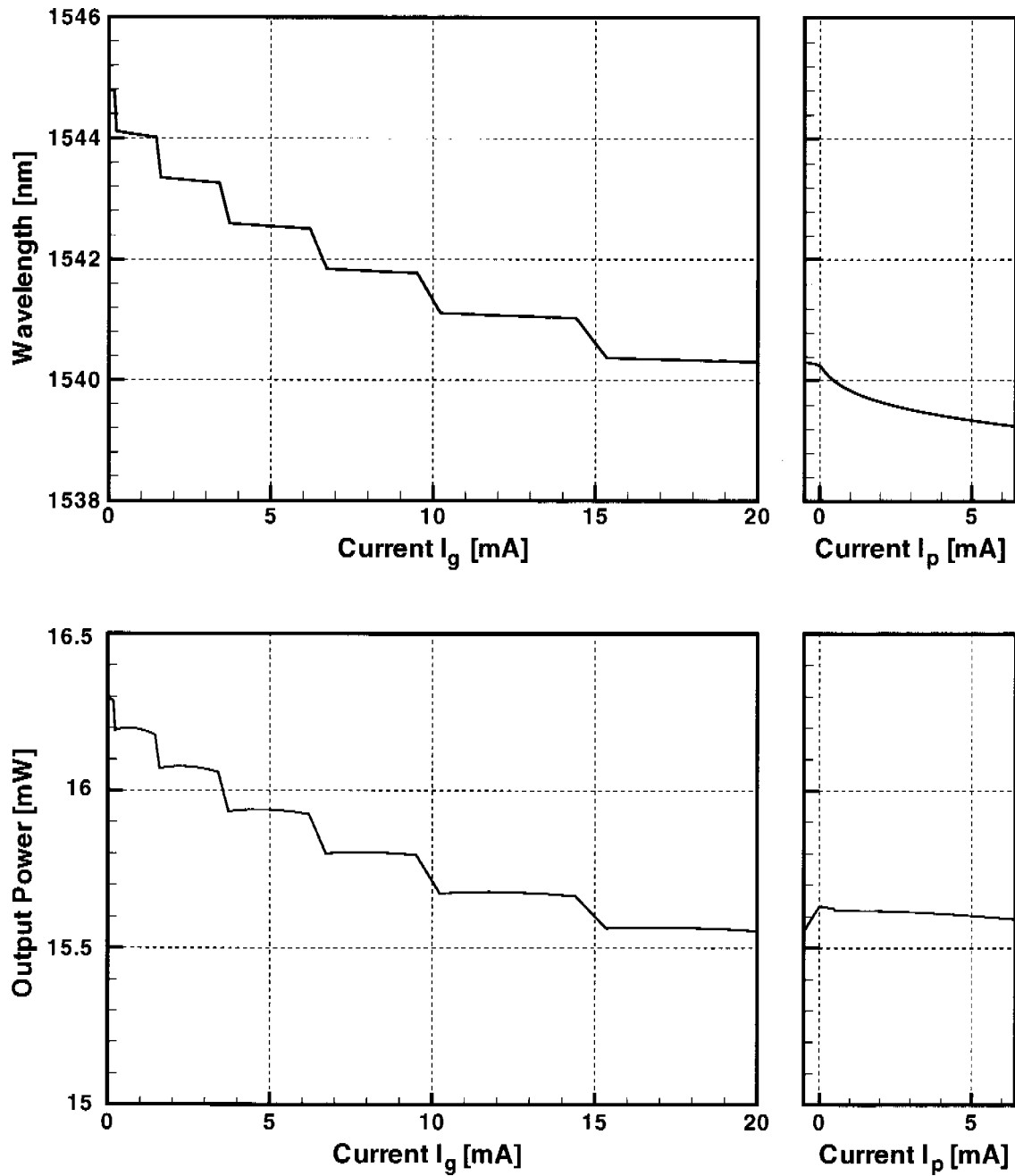


**Figure 4.15:** Realization of a continuous tuning scheme for a three-section DBR laser. Mode jumps can be bridged by injecting current into the phase section while keeping the current of the grating section constant. Simulated wavelength (top) and output power (bottom) versus injection currents demonstrate the experimentally observed behavior. The small negative value of the phase section current  $I_p$  is due to the leakage current between the neighboring device sections.

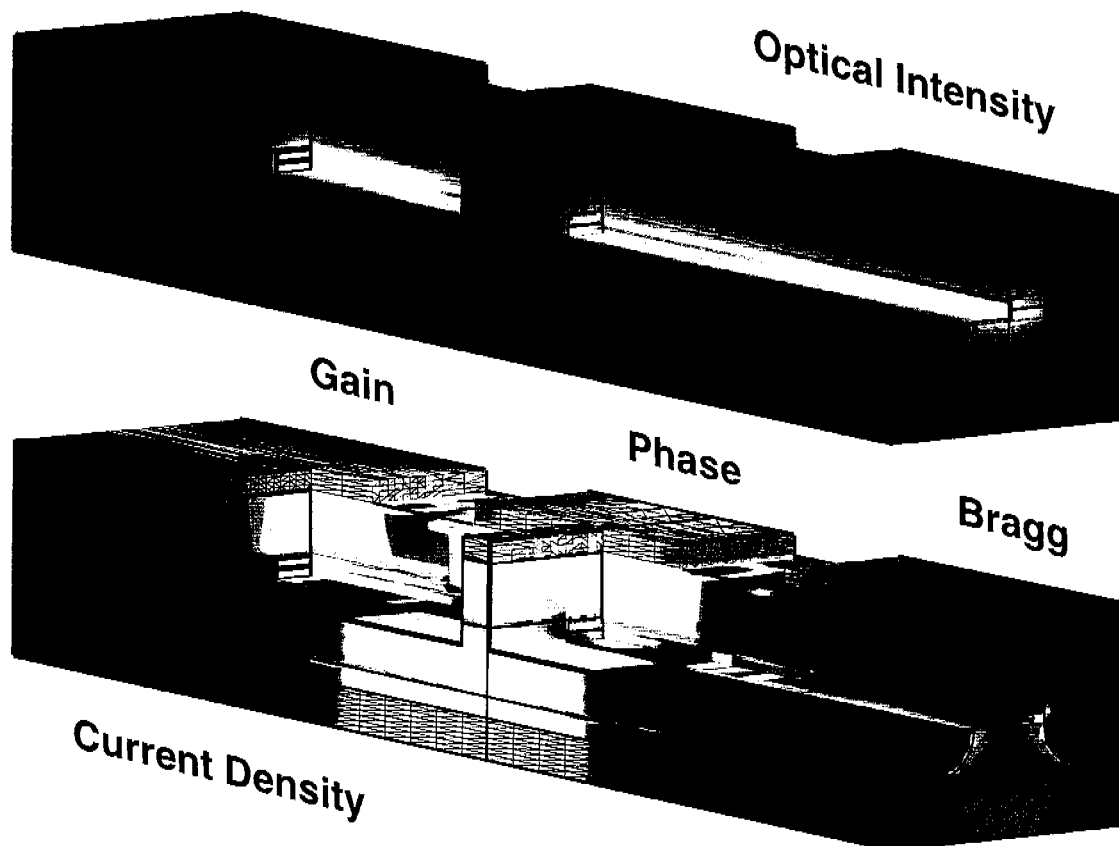


**Figure 4.16:** Zoom into the central region of the device to show transverse and longitudinal effects. Top: Optical intensity distribution. Note that the optical intensity decays in the Bragg section. Bottom: Current density distribution. The different current injection levels of the gain, phase and Bragg sections separated electrically by isolation grooves result in a longitudinally inhomogeneous current distribution. The lateral current confinement due to the semi-insulating blocking region is also visible.



not only because at least one additional equation needs to be solved self-consistently within the Newton–Raphson scheme. Since most variables are subject to either explicit or implicit temperature dependence, the sparsity of the resulting linear system is reduced. As a consequence, the complexity of the core numerical task increases significantly. From a calibration point of view, an extra degree of freedom is introduced in the models of the material parameters, which makes the calibration process more difficult and time consuming.

Certain laser devices are strongly 3D in nature and so is their thermal behavior. The previous discussion of the wavelength-tuning characteristics extracted from full-3D simulations neglected self-heating effects. However, to gain full insight into the device operation, it is desirable, if not indispensable, to take these effects into account, despite the enormous computational task. Moreover, with packaging becoming increasingly important also in the area of optoelectronics, the inclusion of the package into the simulation domain could become important in the future.

At present non-isothermal simulations in full three dimensions, especially of multisection lasers, may not yet meet the requirements of a device engineer in the industry in terms of computational scope. However, as the computing power has been increasing rapidly over the last years, the hardware-related constraints—mainly a fast CPU with a high performance memory subsystem—are expected to ease. The goal of the following is to demonstrate the feasibility of electrothermo-optical simulations of multisection lasers in full three dimensions and to give some examples of the additional information that can be gained from such an effort. The results presented here intend to set the groundwork for future efforts.

For the solution of the local heat flux  $\mathbf{S}$  in Eq. (2.4), appropriate boundary conditions have to be applied. At thermally conducting interfaces, non-homogeneous Neumann boundary conditions are imposed, which imply the specification of the respective thermal resistance for the contact between adjacent materials. In this simulation the thermal resistance of the top air–insulator interface and the air–semiconductor interface at the front and rear of the device has been chosen a factor of one hundred higher than that of the air–substrate interface and the air–insulator interface at the side of the laser. This takes into account that the substrate and width of the device are usually much larger than that covered in the simulation.

To reduce the importance of the exact value for the thermal-resistance component that lies external to the usual electrical simulation domain, as

much of the thermal environment as possible is included. In general, this allows for more accurate modeling of self-heating effects and, hence, results in a realistic picture of the temperature distribution. The thermal simulation domain is highlighted in Fig. 4.17 by the translucent, beige region featuring the simulation mesh. Current density and optical intensity distribution are depicted in the electrical domain for a steady-state situation of the active section current around 100mA and moderately biased phase and grating section. For this operating point, the electrical isolation by means of ion implantation between the respective sections is in effect, which can be seen in the bottom of Fig. 4.17.

Contrary to the current density, a look at the simulated temperature distributions in Fig. 4.18 shows that heat generated in either section has an influence on the neighboring sections. This illustrates the potential of non-isothermal simulations in full three dimensions where such effects can be investigated in detail. The temperature distribution of the DBR laser is shown in Fig. 4.18 for three different operating points. From top to bottom, the individual sections are successively biased to their maximum values, representing the typical device operation of a tunable three-section DBR laser. As a result, the maximum temperature in the active and grating sections increases between 60°C and 80°C, while the temperature rise in the phase section is lower than 40°C.

Figure 4.19 indicates that the temperature profile in all but the phase section is dominated by self-heating due to current injection above 100mA. In the phase section, however, the profile is clearly a result of crosstalk heating as its bias current is usually at least one order of magnitude smaller. Both heating effects can play an important role in device operation because the temperature rise leads to a refractive index shift, which affects the tuning behavior.

Generally, the ratio between self-heating and crosstalk heating depends on the design and type of tunable laser, which determine the typical operating regime. In SGDBR or SSGDBR lasers, for example, the passive front and rear mirror sections only need to be biased very moderately, thus, crosstalk heating from the neighboring sections is the dominant contribution [107].

Another issue that is related to the design of the tunable laser and its material system concerns the relative weight of the various heat sources: Joule heat, electron–hole recombination heat and Thomson/Peltier heat. Especially in InGaAsP–InP lasers, recombination heat, mainly due to Auger recombination, can be comparable to Joule heat and is therefore not negli-

ble. Figure 4.20 shows the recombination heat of the DBR laser as a result of forward biasing the active and grating sections. It can be seen that the major heat contributions stem from the active region and the waveguide core in the rear mirror section. A transverse cut through the active section, shown in Fig. 4.21, suggests where Joule heating is expected to be strong. The current streamtraces indicate current crowding in the proximity of the interface between the active region and the semi-insulating current blocking region. In this example, the temperature profile reveals that Joule heat does not dominate over recombination heat. Exact quantitative results would have to be obtained from simulations, which are calibrated with experimental data.

#### 4.3.4 Simulation Statistics

In the preceding sections, the simulation results obtained from a multidimensional modeling approach for a three-section DBR laser have been presented. Table 4.2 summarizes the computational scope, which is characterized by the dimensionality of the simulation domain, the mesh size and the physical equations to be solved.

For the two-dimensional simulations discussed in Section 4.3.2, 4k vertices are sufficient to resolve the layer structure adequately. It can be seen from Fig. 4.22 that curved interfaces lead to a higher vertex count than straight interfaces. However, in two dimensions, the mesh size is not as critical as in higher dimensions. A non-isothermal simulation of a full laser characteristic shown in Fig. 4.12 typically requires 250MB of memory and around 15min CPU time on a SuperMicro 6022CB, 2.2 GHz Intel Xeon.

Extended 2D simulations take into account the vertical and longitudinal structure of the three-section DBR laser but only contain one cell in the lateral direction, which is depicted in Fig. 4.23. Since the grid size can be restricted to 12k vertices—comparable to a complex 2D simulation (see Fig. 4.9)—they are well suited to the efficient simulation of the tuning behavior and longitudinal spatial hole-burning effects. An isothermal simulation of the tuning characteristics consists of driving the laser to its operating point well above threshold, followed by current injection into the grating section. This requires less than 2GB of memory and around 1.5h CPU time on a Dalco r2164ia, 2.4GHz AMD Opteron\_250.

In going to full three dimensions, the mesh size increases significantly, resulting in a vertex count of around 65k and 83k for isothermal and non-isothermal simulations, respectively. Despite the fact that the addition of

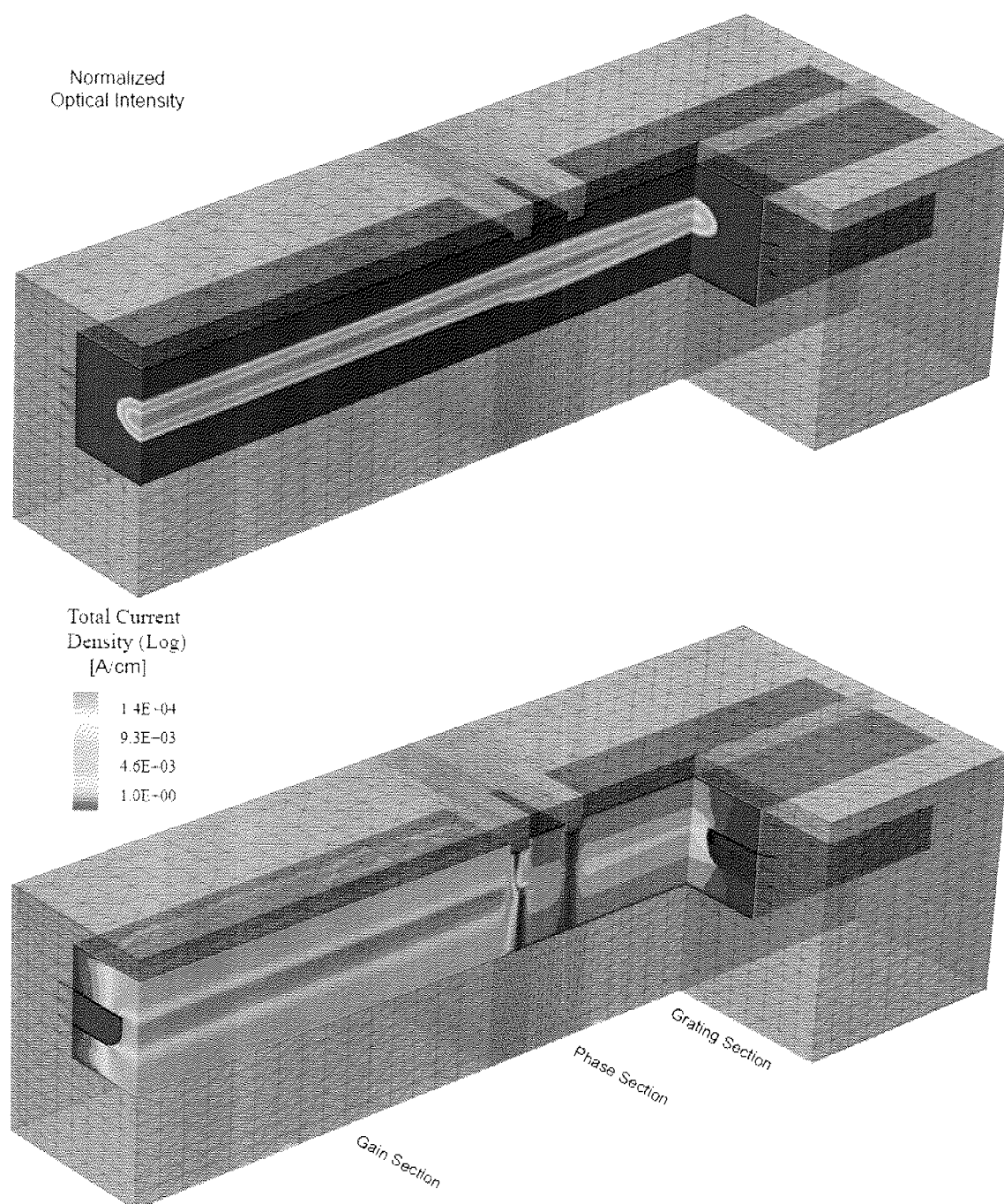


**Figure 4.17:** Normalized optical intensity (top) and total current density (bottom) distribution resulting from coupled electrothermo-optical simulation of three-section DBR laser. The translucent beige region depicting the simulation mesh consists of insulating material and has been added to the electronic simulation domain for more realistic thermodynamic modeling.

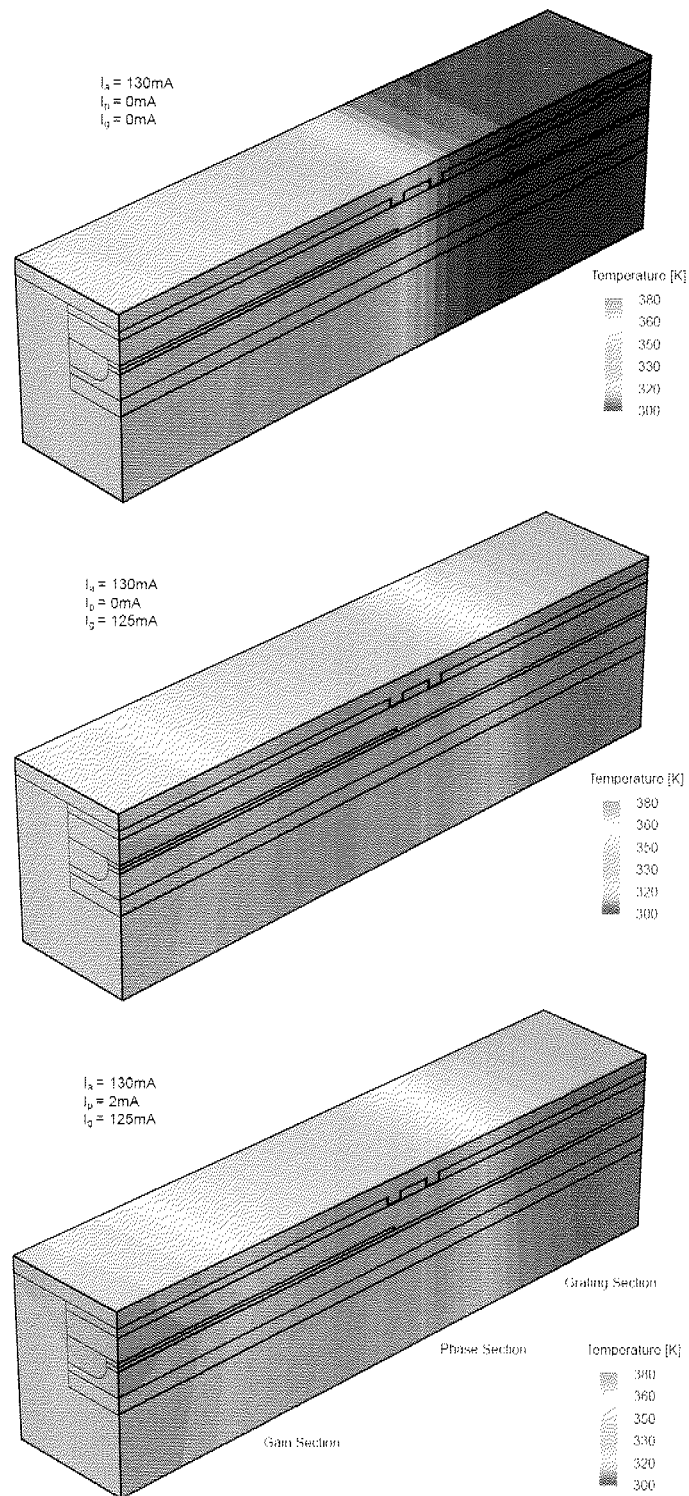


**Figure 4.18:** Temperature distribution of DBR laser for three different operating points. Top: Current injection into active section only. Middle: Current injection into active and grating section. Bottom: Current injection into all three sections.

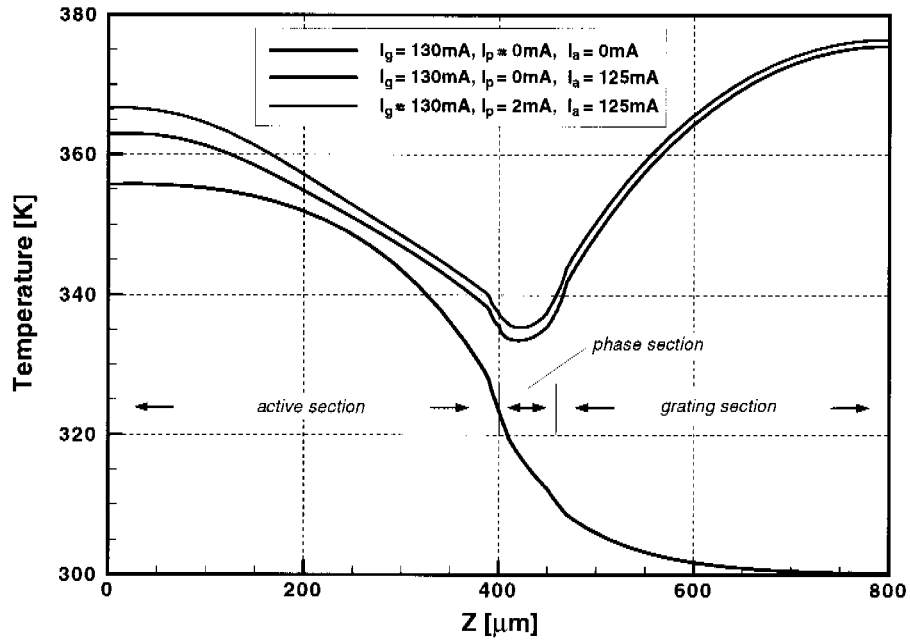


**Figure 4.19:** Longitudinal temperature profiles for three characteristic operating conditions. The profiles have been extracted from the DBR laser shown in Fig. 4.18 at the height of the active region in the center of the device.

a thermal domain more than triples the total volume, the increase in mesh vertices is moderate due to the coarseness of the grid permissible in the thermal region. Figure 4.24 shows that up to 40% of the total number of mesh vertices is used in the central transition region between the three device sections in order to ensure accurate simulation results. A typical self-consistent electro-optical simulation in full three dimensions requires 6GB of memory and around 8h CPU time, whereas a non-isothermal simulation consumes 8GB of memory and takes up to one day.

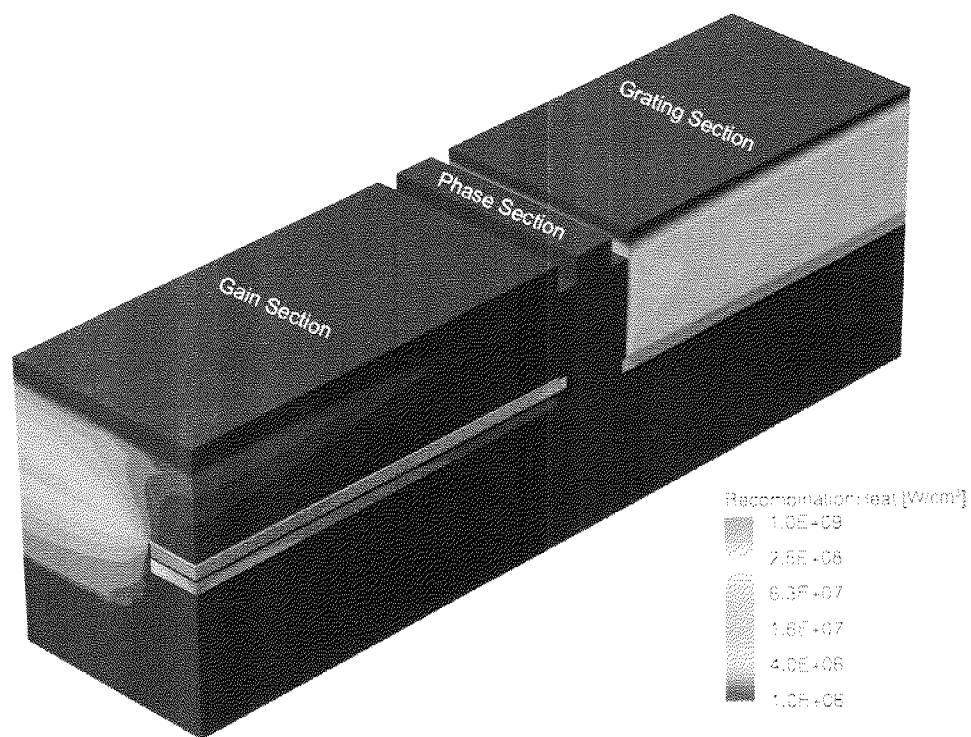


**Figure 4.20:** Heat generation caused by SRH and Auger recombination in DBR laser when current is injected into active and grating sections.

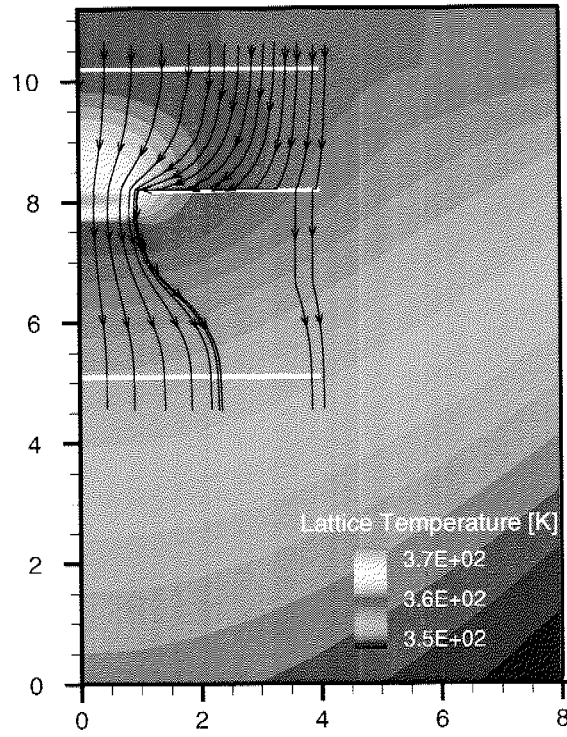


**Figure 4.21:** Transverse cut through the active section of a DBR laser showing temperature distribution and current streamtraces. The effect of the semi-insulating current confinement region is clearly visible.

Simulation Domain	Mesh Vertices	Iso-Thermal	Architecture	RAM [GB]	CPU Time
2D	4k	no	SuperMicro 6022CB, 2.2 GHz Intel Xeon	0.25	15min
extended 2D	12k	yes	Dalco r2164ia, 2.4GHz AMD Opteron250	1.8	1.5h
full-3D	65k	yes	Dalco r2164ia, 2.4GHz AMD Opteron250	6	8h
full-3D	83k	no	Dalco r2164ia, 2.4GHz AMD Opteron250	8	24h

**Table 4.2:** Simulation statistics of the DBR laser comparing the computational scope of multidimensional modeling.



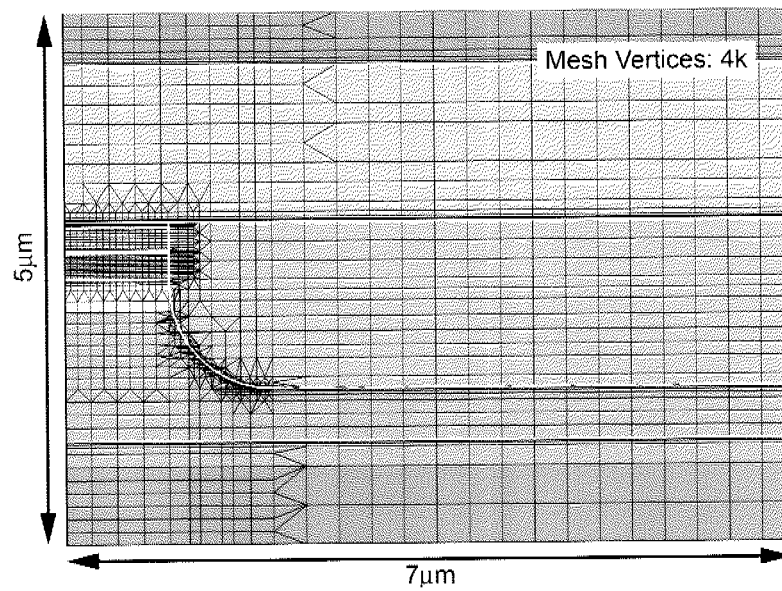


**Figure 4.22:** Illustration of simulation mesh for a transverse cross section representing the active section of a DBR laser.

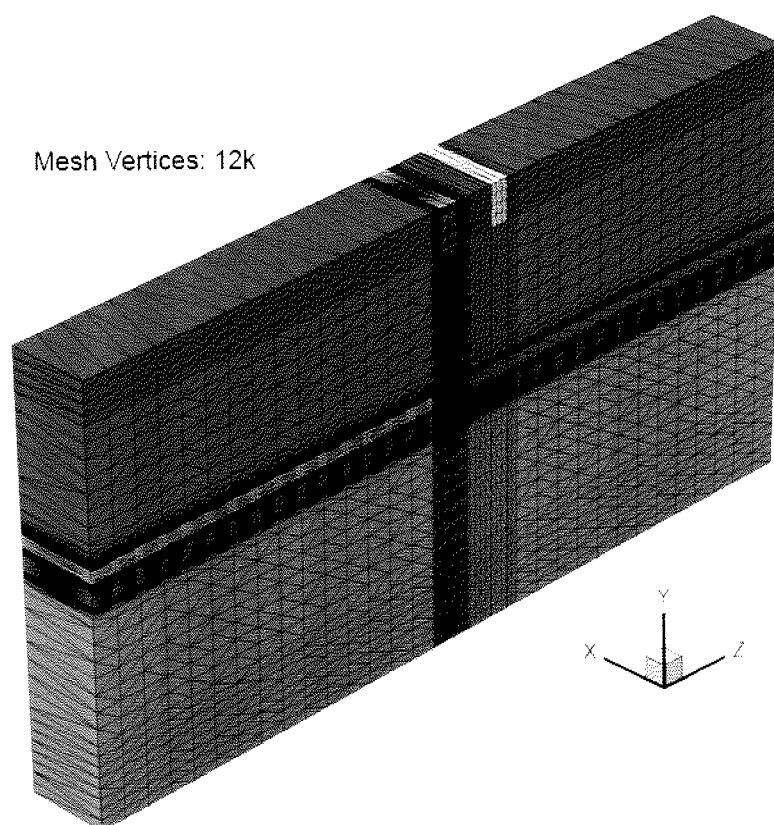


**Figure 4.23:** Illustration of extended 2D simulation mesh of three-section DBR laser. The active region is shown in yellow in the front section of the device.

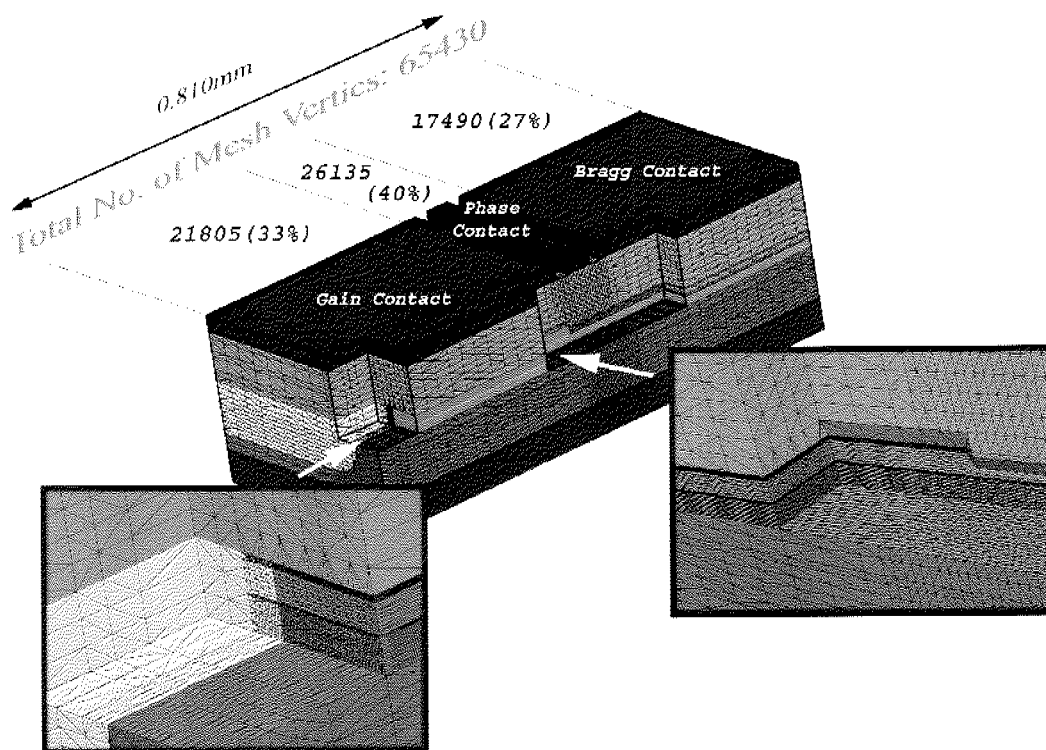


**Figure 4.24:** Statistics for 3D simulation mesh. A strongly inhomogeneous mesh is needed to resolve the characteristic device features. A comparatively large number of mesh vertices in the transition regions ensures accurate simulation results.

## 4.4 Widely Tunable Sampled-Grating DBR Laser

The last simulation example presented in this work belongs to the class of widely tunable integrated semiconductor lasers. It is the most complex device from both a modeling and an experimental perspective treated within the framework outlined in Chapters 2 and 3. The focus is directed at the wavelength tuning behavior and the simulation of its characteristics in three dimensions. To support the simulation results, the simulator has been benchmarked against another high-end software package in one and two dimensions, using the same simulation parameters that have later been used in the comparison to measurements.

### 4.4.1 Introduction

The SGDBR laser simulated in this work has been designed as a component of a widely tunable wavelength converter/transponder reported in [108]. Besides the SGDBR laser integrated with a semiconductor optical amplifier (SOA) shown in Fig. 4.25, the module includes another SOA, a waveguide photodetector and an electro-absorption modulator. Apart from the solution of the combined waveguide problem depicted in Fig. 4.26, the SOA is assumed to be at transparency and only the SGDBR laser is simulated. The accurate description of the integrated device would require a model for the amplified spontaneous emission in the SOA and is beyond the scope of this work. The detailed epitaxial layer structure of the SGDBR laser under investigation, which has been fabricated at the University of California, Santa Barbara (UCSB), is summarized in Table 4.3. The MQW active region consists of seven compressively strained quantum wells with a gain-peak wavelength of  $1.53\mu\text{m}$ . A thin etch-stop layer separates the active region from the 1.3Q waveguide core, which extends through the entire length of the device.

Details of the longitudinal structure including the design of the sampled gratings are given in Table 4.4. A proton-implanted channel between each of the different device sections is formed in order to reduce current leakage across section boundaries. In the simulation, the proton implant is simply modeled by reduced carrier mobilities in the respective regions. Etched grooves make sure that the various contacts are electrically isolated from each other.

A research visit at the University of California, Santa Barbara, where the SGDBR laser has been invented and advanced research devices are being fab-

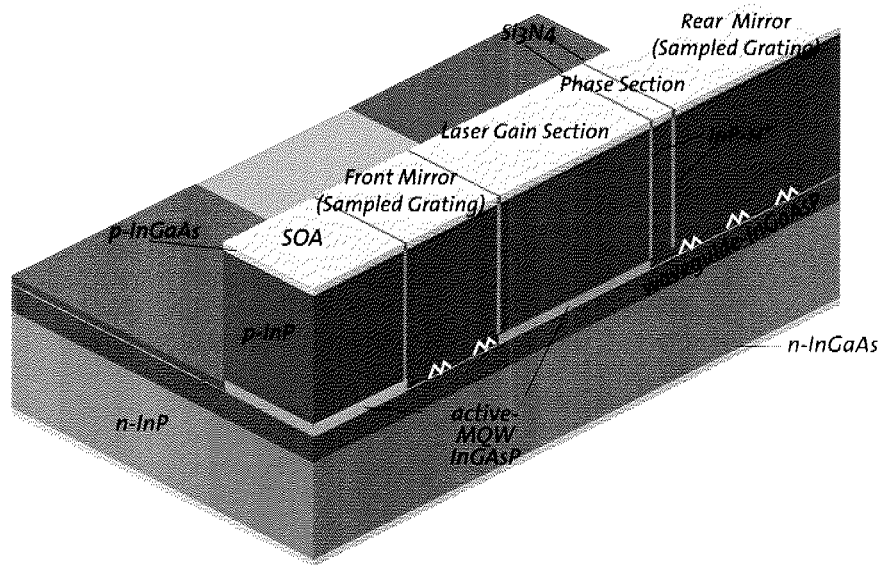


**Figure 4.25:** Schematic illustration of an SGDBR laser integrated with an SOA that has been used as a component in a wavelength converter/transponder [108]. To simplify its modeling, the SOA is assumed to be at transparency and, to a good approximation, can be truncated in the simulation.

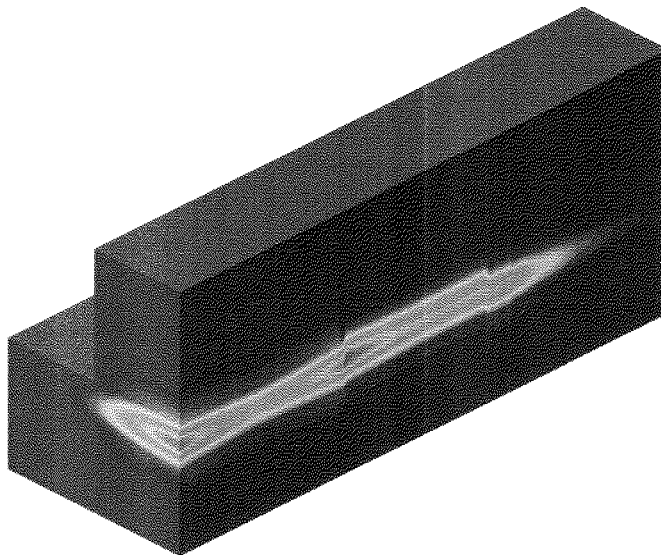


**Figure 4.26:** Optical mode pattern of an SGDBR laser integrated with an SOA, which is above transparency.

Layer	Material	Thickness [nm]	Doping [ $10^{18}\text{cm}^{-3}$ ]
p-contact	InGaAs	100	30(p)
upper cladding	InP	1500	1(p)
upper cladding	InP	200	0.3(p)
SCH	$\text{InGa}_{0.218}\text{As}_{0.508}\text{P}$	25	$\langle 10^{-3}(\text{n}) \rangle$
doping setback	InP	50	$\langle 10^{-3}(\text{n}) \rangle$
quantum barrier ( $8\times$ )	$\text{InGa}_{0.265}\text{As}_{0.513}\text{P}$	8.27	$\langle 10^{-3}(\text{n}) \rangle$
quantum well ( $7\times$ )	$\text{InGa}_{0.265}\text{As}_{0.845}\text{P}$	6.72	$\langle 10^{-3}(\text{n}) \rangle$
etch stop	InP	10	$\langle 10^{-3}(\text{n}) \rangle$
waveguide	$\text{InGa}_{0.368}\text{As}_{0.778}\text{P}$	352.5	0.1(n)
lower cladding	InP	1300	1(n)
n-contact	InGaAs	100	1(n)

**Table 4.3:** Epitaxial layer structure of the SGDBR laser simulated in this work. The doping concentrations in angle brackets indicate an intrinsic level, which is represented by the specified values in the simulation.

Section	Length [ $\mu\text{m}$ ]	$\kappa$ [1/cm]	Sampled Grating DBR
Front Mirror	307.5	250	$5\times 4\mu\text{m}$ grating bursts with $46\mu\text{m}$ period
Gain	500	—	—
Phase	75	—	—
Rear Mirror	552	250	$12\times 6\mu\text{m}$ grating bursts with $65.5\mu\text{m}$ period

**Table 4.4:** Details of the longitudinal structure of the SGDBR laser including the specification of the sampled gratings.

ricated, allowed for the benchmarking of the simulator against another high-end software package<sup>8</sup> in one and two dimensions.<sup>9</sup> Using essentially the same input parameters,<sup>10</sup> the study showed a close match between the two simulators for a number of fundamental properties: current-voltage characteristics, bound states in the active region, optical gain, optical confinement factor and light-current characteristics. These parameters were then used in the three-dimensional simulation setup.

#### 4.4.2 Three-Dimensional Simulation of Wavelength Tuning Characteristics

In this section, the wavelength tuning characteristics of the ridge waveguide SGDBR laser specified by Tabs. 4.3 and 4.4 are investigated using self-consistent simulations in three dimensions. The results show that physics-based device simulation can accurately predict not only the wavelength change with respect to the tuning sources, but also its feedback on the light output power and the gain section voltage. The latter plays an important role in controlling the lasing mode—a challenge that all tunable lasers face.

The SGDBR laser owes its wide wavelength tunability to a pair of slightly different sampled gratings located in the front and back end of the device. As current is injected into the grating sections, the corresponding reflectivity spectra are shifted with respect to each other. The overlap between the two spectra as shown in Fig. 4.27 determines the filter wavelength. If current is injected into one grating section only, the wavelength changes are subject to periodic mode jumps. On the other hand, a continuous tuning regime is obtained by simultaneously biasing the mirror sections. Figure 4.28 shows the product of the reflectivity spectra depicted in the top graph of Fig. 4.27 and the calculated resonances of the multisection laser cavity, which determine the lasing wavelength in the self-consistent simulations.

The general design and performance of sampled gratings can be studied efficiently in one dimension using analytical expressions derived from coupled-mode theory or the transfer-matrix method [85]. In going to three dimensions, the current density distribution and the resulting effective index distribution for a given bias point, which are the input to these methods,

<sup>8</sup>Crosslight Software Inc., Canada.

<sup>9</sup>The results of this benchmark are partly documented by the 4<sup>th</sup> Deliverable to the Semiconductor Research Corporation, Award Number 2001-NJ-968, Task ID: 968.001.

<sup>10</sup>The material parameters and their compositional dependence have been taken from [109].

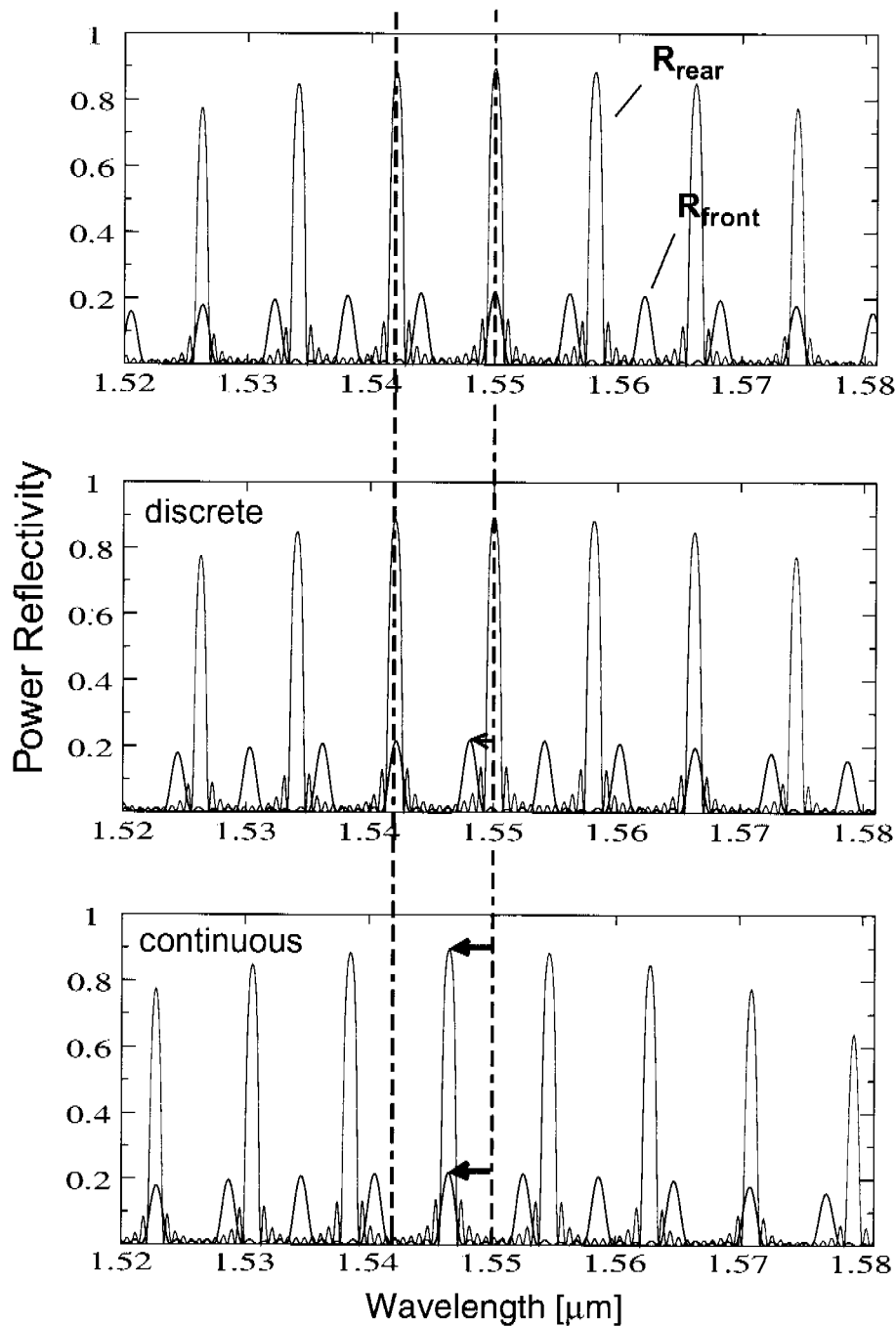


**Figure 4.27:** Reflectivity spectra of sampled gratings in front and rear mirror sections of an SGDBR laser. Top: Center peaks are perfectly aligned. Middle: Current is injected into front mirror section shifting its spectrum to shorter wavelengths. The result is a mode jump due to the maximum overlap between the neighboring peaks. Bottom: Current is injected into both mirrors simultaneously shifting both spectra by the same amount. This leads to a continuous blue shift of the lasing wavelength.



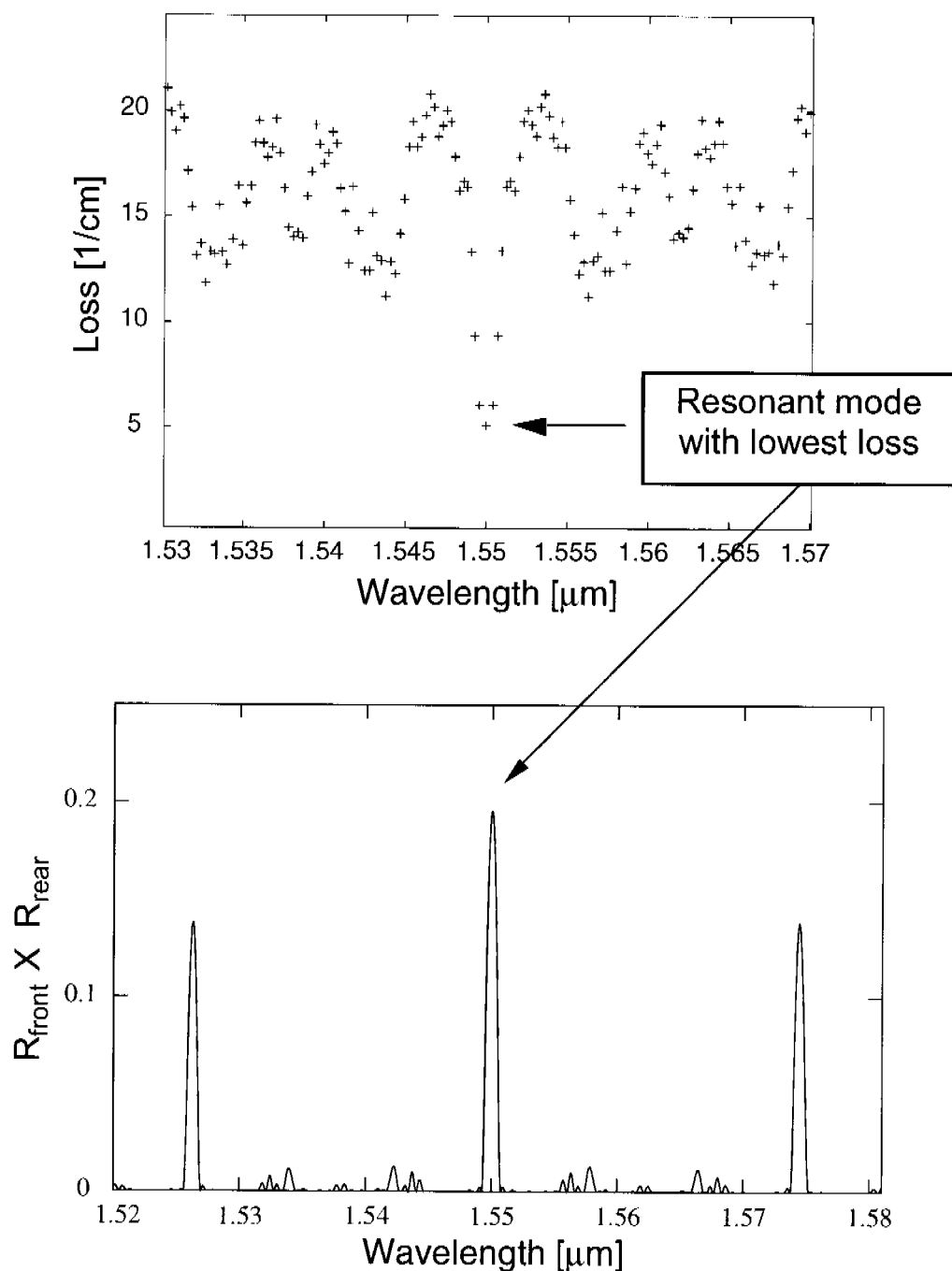


**Figure 4.28:** Top: Resonant longitudinal modes of SGDBR cavity. Bottom: Product of front and rear mirror reflectivities indicating the main mode together with the dominant side-modes when the mirrors are perfectly aligned with respect to their center-peaks as shown in the top graph of Fig. 4.27.

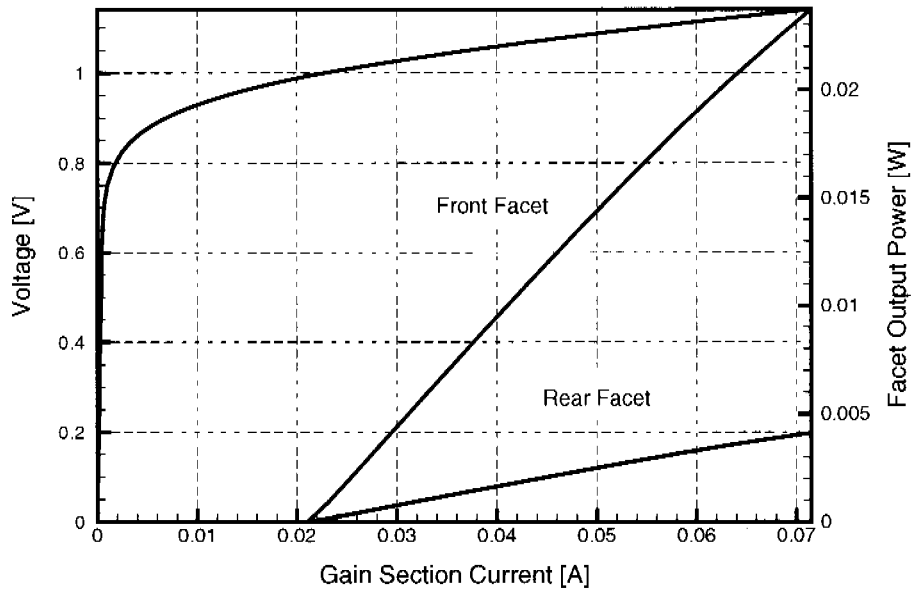


**Figure 4.29:** Facet output power and gain section voltage as a function of gain section current as obtained from full-3D simulation.

can be modeled accurately. Therefore, inhomogeneities related to the device structure or operation condition can be accounted for and the feedback of the optics to the electrothermal system can be treated in a self-consistent manner.

A map that shows the lasing wavelength as a function of the front and rear mirror currents has been created as follows. In an initial simulation step, the laser is ramped to the operation point, as shown in Fig. 4.29, whose state can be saved and reloaded as an initial solution in other simulations. Then, for example, the front mirror current is incremented to a fixed value and the rear mirror current is swept. During the tuning operation, the phase section has been adjusted as described in Section 3.4 to guarantee the highest possible side-mode suppression ratio and to compare it to measurements. In this way, the wavelength tuning map shown in Fig. 4.30 was generated. It was obtained by sweeping the rear mirror current for 40 different values of the front mirror current. The simulated tuning map is in good agreement with experimental data from the University of California, Santa Barbara, shown in Fig. 4.31. Its characteristic staircase shape reflecting the continuous and discontinuous tuning regimes is clearly visible. Further improvement can be achieved by a better calibration of the carrier dependence in the refractive index model, which essentially determines the scaling of the tuning map

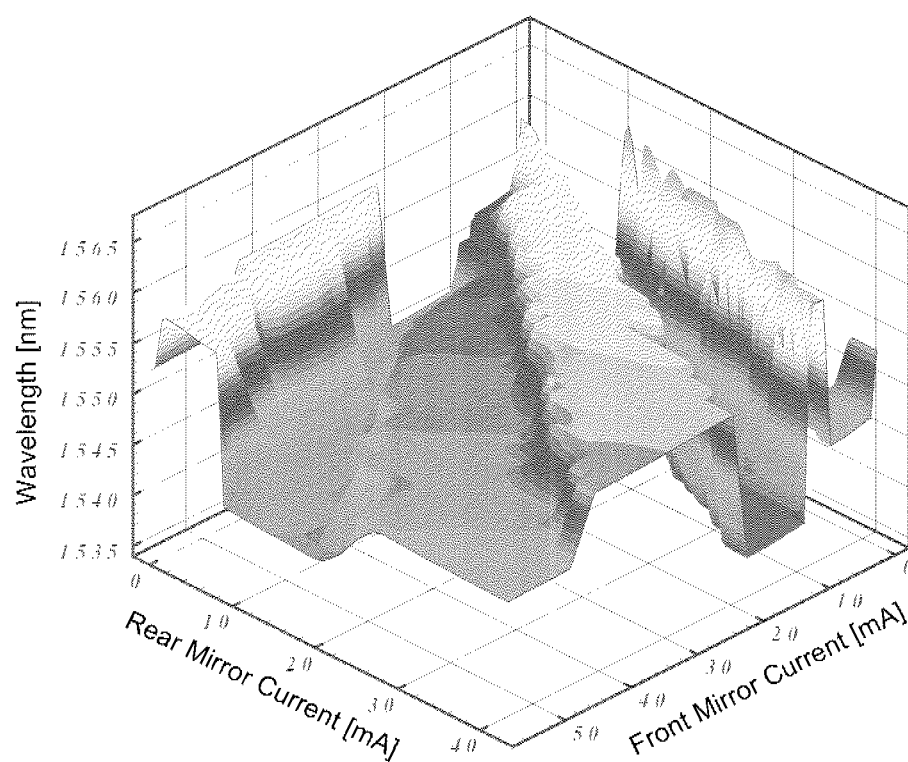


**Figure 4.30:** Wavelength tuning map of SGDBR laser obtained from 3D simulation.

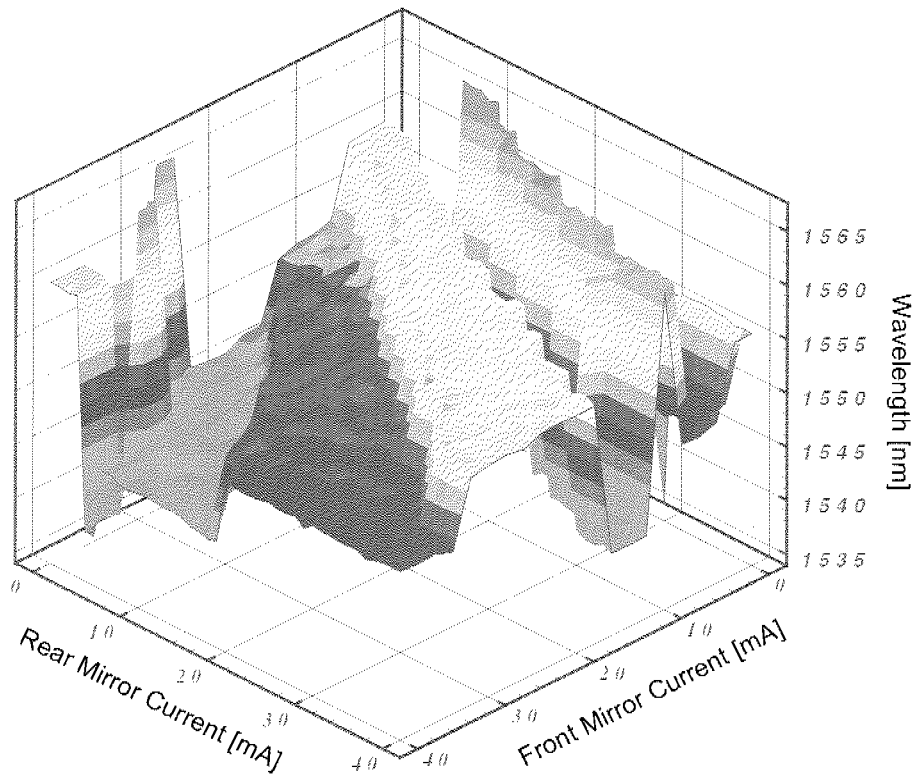


**Figure 4.31:** Measured wavelength tuning map of SGDBR laser.

with respect to the injection currents.

In addition to the wavelength tuning map, the corresponding maps for the optical output power, loss and active section voltage can be analyzed. These properties are of importance to developing mode control algorithms, that is, finding the optimal section currents for each wavelength channel. Furthermore, the output power is also a system criterion, which vendors of tunable lasers have to meet. Usually, the packaged device is integrated in a module, which includes the control electronics and firmware for maintaining a reliable operation over the entire lifetime of the device. A wavelength lookup table generated at the time of calibration alone is not sufficient due to device aging, and a number of control strategies have been developed to adjust the settings accordingly. These strategies are based on operating the laser either at a saddle point of the output power surface [110] or at an extremum of the surface of the gain section voltage [33, 111, 112].

Figure 4.32 shows the facet output power surface as the SGDBR laser is tuned over a wavelength range of approximately 30nm. Distinct saddle points can be identified, which are located in the continuous regions of the

wavelength surface. They correspond to peak reflectivity states, in which the cavity mode is aligned with the reflection peaks of both sampled gratings [110].

The optical output power varies for several reasons. First, current injection into the tuning sections leads to carrier-induced losses. Second, since the envelope of the sampled-grating reflectivity peaks decreases on both sides of the center peak, the effective mirror loss increases. The extent of this change depends on the specific peaks that are aligned in order to tune to a given wavelength. Third, as the wavelength is tuned, the nonflat and usually asymmetric gain spectrum is sampled. All of these effects are considered in the simulation, and Fig. 4.33 shows the contour of the net loss as an overlay on the wavelength surface.

For a more accurate modeling of the contribution stemming from the specific gain spectrum, more advanced gain models are available in the simulator and would best be calibrated in a preprocessing step. In this analysis, the standard free-carrier gain model calibrated with respect to the gain peak and its position has been employed to limit the computational task.

Since the saddle points in the optical output power may not appear for higher tuning currents due to the absorption losses [112], the mode control scheme, which relies on the active section voltage, is usually preferred. By perfectly aligning the front and back reflector peaks, a local minimum in threshold gain and carrier density is reached. At fixed bias current, this translates into a minimum in the gain section voltage, which is shifted towards lower currents if carrier-induced losses are present. However, the effect is sufficiently small so that the voltage minima remain within the mode boundaries even for increased tuning currents where the other control method would fail. Figure 4.34 shows the contour of the simulated gain section voltage as an overlay on the wavelength surface. The colormap clearly indicates the voltage minima corresponding to stable mode regions.

The simulation results and their comparison to experimental data presented in this section demonstrate that—despite the numerical difficulties related to discontinuous changes in a solution variable—a robust self-consistent solution scheme is capable of reproducing the full device behavior in three dimensions.

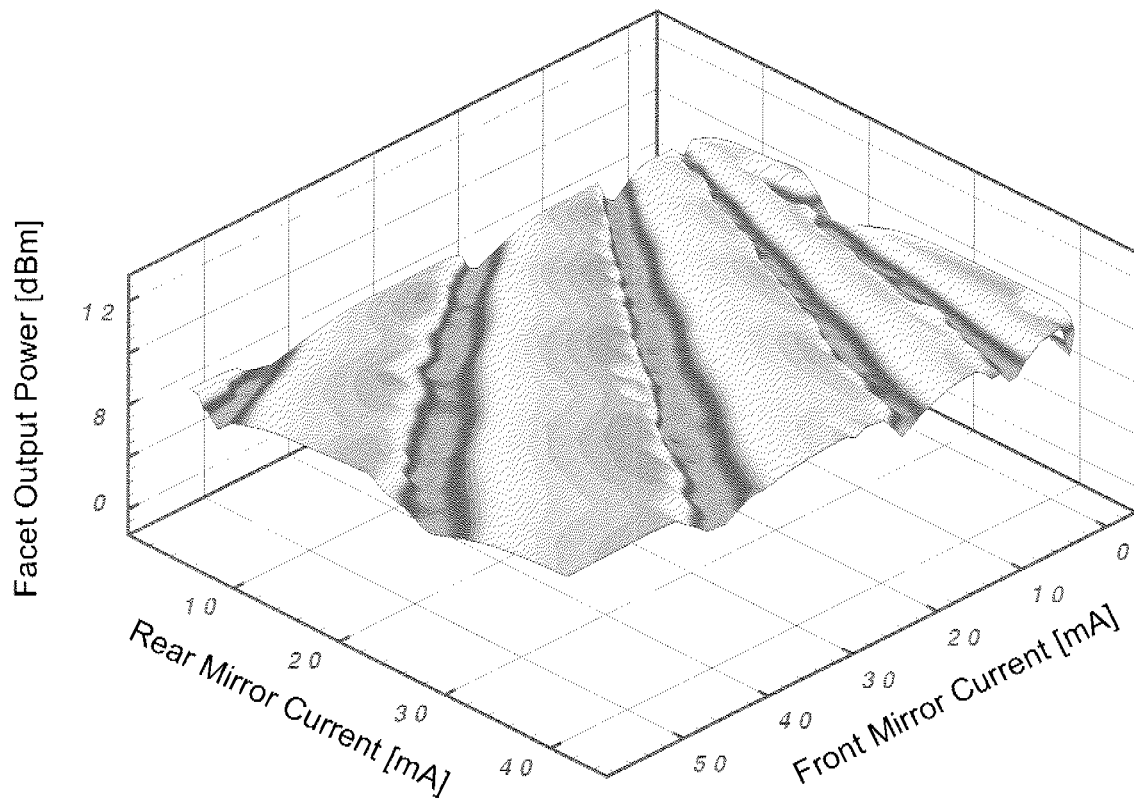


**Figure 4.32:** Facet output power of SGDBR laser under tuning operation.

### Spatial Hole-Burning

The spatial hole-burning (SHB) effect can have a detrimental influence on the single-mode behavior of a laser. An inhomogeneous power distribution at elevated power levels of a laser results in an inhomogeneous carrier density distribution: Carriers are depleted faster at the maxima of the wave, which leads to a decrease in the modal gain. Since the refractive index depends on the carrier density, the optical properties of the laser also change.

Figs. 4.35 and 4.36 show the longitudinal and lateral SHB effect for the SGDBR laser obtained from an eletro-optical simulation in full three dimensions. While SHB can crucially influence single-mode operation in DFB lasers, its impact is less severe in DBR-type lasers, since the grating is separated from the gain region. However, the influence on the laser linewidth can be observed in both.

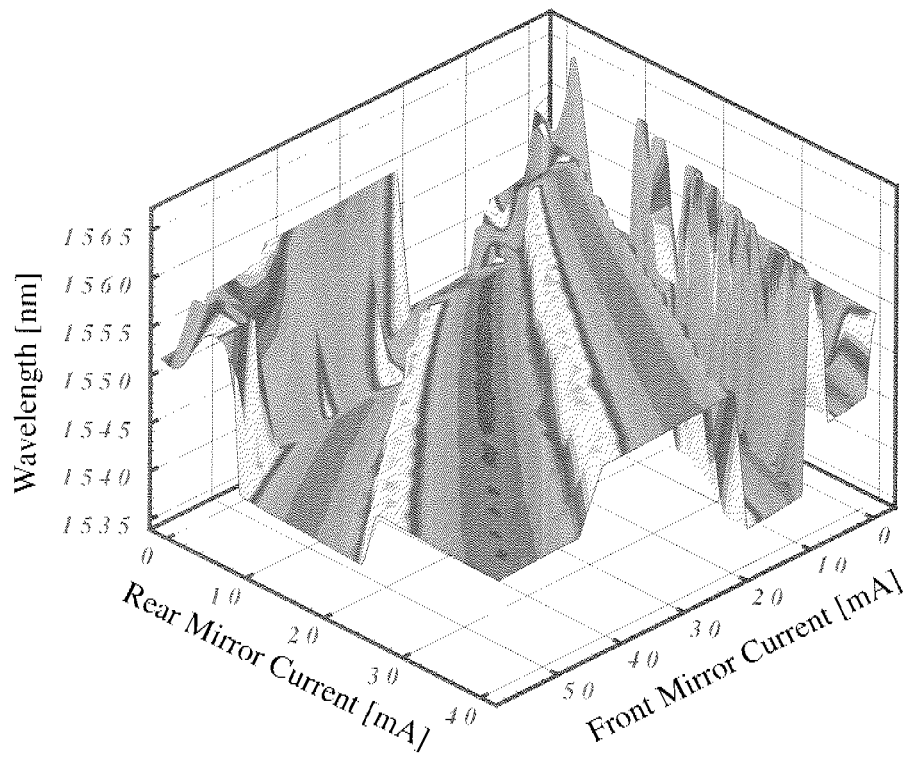


**Figure 4.33:** Optical mode loss (shown as colormap on the wavelength surface) under tuning operation.

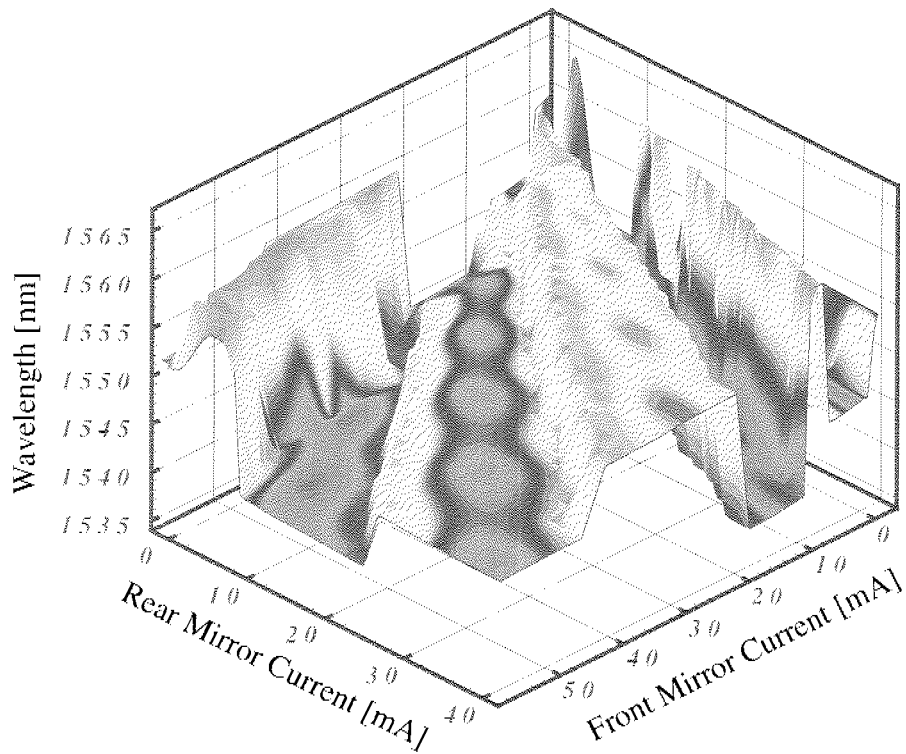


**Figure 4.34:** Active section voltage (shown as colormap on the wavelength surface) under tuning operation.

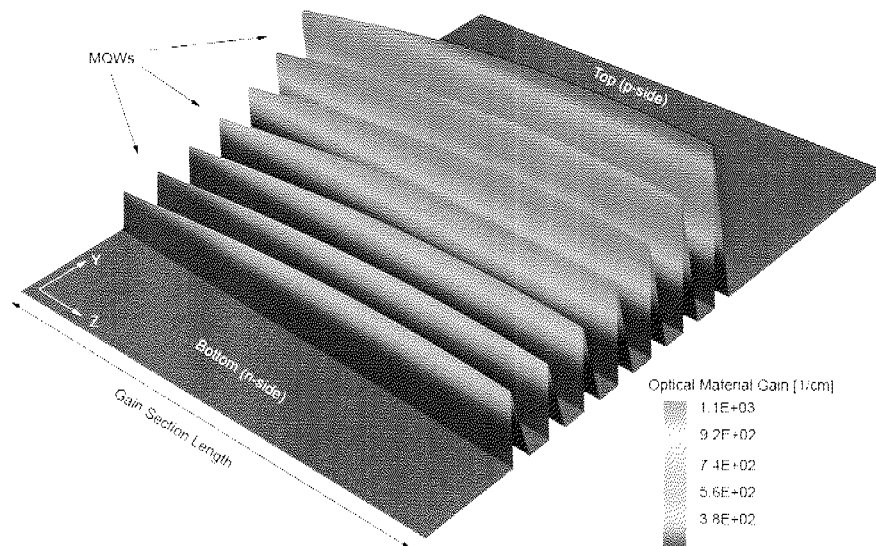


**Figure 4.35:** Longitudinal spatial hole-burning across MQW region.



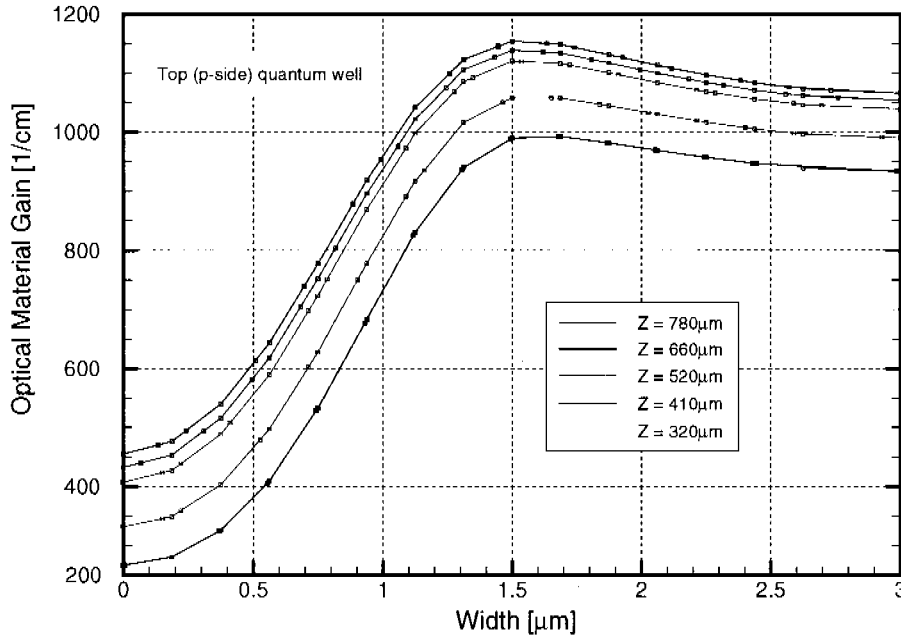


**Figure 4.36:** Lateral spatial hole-burning at various positions along the active section of the SGDBR laser at 10mW output power.

### 4.4.3 Simulation Statistics

The simulation of the tuning maps presented in Section 4.4.2 lends itself to be distributed over a computer cluster. Each node is assigned the calculation of the tuning characteristics for a given front-mirror current as a function of rear-mirror current or vice versa. On a Linux cluster consisting of 20 nodes, each featuring a Dalco r2164ia, 2x2.4 GHz AMD Opteron\_250/1MB Cache CPU, the wall clock time for the entire task is around 5h if extended 2D simulations are performed.<sup>11</sup> To simulate the same tuning map in full three dimensions, the wall clock time is almost five times longer. This is due to the large number of mesh vertices ( $\sim 72\text{k}$ ) shown in Fig. 4.37, which requires about 7GB of memory.

<sup>11</sup>Each simulation requires about 2GB of memory.

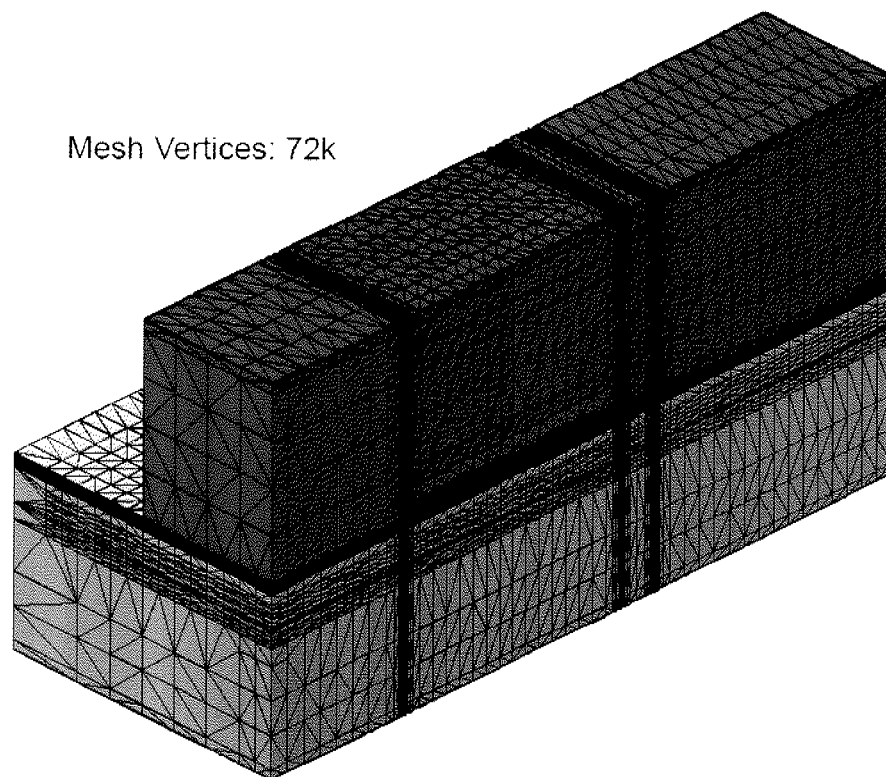


**Figure 4.37:** Simulation mesh of the SGDBR laser. Note the refinement of the mesh in the transition regions between neighboring device sections.

## 4.5 A Guide to 3D Laser Simulation

Having discussed the physical models and their implementation together with results for several tunable lasers, let us conclude with some practical aspects of full-3D semiconductor laser simulation. The following focuses on the simulator presented in this thesis; however, several issues are of general significance and apply to any comparable optoelectronic device simulator.

### Structure Generation and Meshing

Conceptually, there is little difference between 2D device simulation, which is well established both in research and development, and its generalization to three dimensions. The starting point of any device simulation is the generation of the device structure including the doping profiles. The preferred way for this task would be through process simulation. While known as a standard in the silicon world, process simulation for III–V compound semiconductors is still in its infancy and a great challenge, especially in three dimensions. As a result, a combined structure and doping editor is commonly used instead.<sup>12</sup>

The next step is considerably more challenging and greatly influences the simulation with regards to accuracy, convergence behavior and computational task in terms of memory and CPU time. Generating the simulation mesh requires a careful choice of refinement regions to resolve all device features and the involved physical quantities—such as current paths and large gradients—while keeping the vertex count as low as possible. The Debye length, which is the distance in a semiconductor over which the local electric field affects the distribution of free charge carriers, gives a clue to the minimum mesh point separation. It is given by  $L_D = \sqrt{(\epsilon U_T)/(qC)}$ , where  $U_T$  is the thermal voltage and  $C$  is the doping concentration.

For typical laser devices with doping concentrations of  $10^{15}$ – $10^{18}\text{cm}^{-3}$ , the Debye length is of the order of 10nm or less. With a simulation domain size of  $\sim 0.01\mu\text{m}^3$ , the resulting grid size would be orders of magnitude too large to fit on present computer hardware. Fortunately, good simulation results can be achieved on considerably coarser grids [114]. However, even in coarse grids, finely meshed regions to resolve heterojunctions and quantum wells are necessary and cannot be avoided.

---

<sup>12</sup>In this work, the 3D structure and doping editor *DEVISE* has been used [113].

Figure 4.38 shows the specific tool flow followed in this work. After the structure generation, it branches out for the meshing of the 2D cuts, which are required for the solution of the optical problem, and the meshing of the actual 3D structure. The latter involves two steps due to the three-point model used for the treatment of quantum wells. First, the device structure is meshed after the MQW region has been collapsed to a virtual contact layer. In the second step, the discretized MQW stack is inserted with the number of grid planes in the barriers defined by the user. The embedding of a local, specialized grid in the global Delaunay mesh is particularly complex if the MQW region does not extend through the entire device in the lateral and longitudinal directions.<sup>13</sup>

Regarding the structure generation for non-isothermal simulations, the region of thermal interest usually exceeds the simulation domain required for accurate electro-optical modeling. In principle, this can be accounted for by the right choice of thermal boundary conditions. However, best results from both a physical and numerical point of view are obtained if as much as possible of the thermally relevant region such as heat sinks, substrate and packaging material is included in the simulation domain. Since the thermal diffusion length in this region is usually large compared with the grid spacing required in the electro-optical domain, the effect on the total number of mesh points is relatively small.

To simplify the simulation setup, the tool sequence can be automated and their respective input files parameterized using the common application framework GENESIS<sub>E</sub> [71].

## Device Simulation Setup

The device simulator DESSIS is driven by a single command file, in which the user can specify input and output file names, physical models, numerical parameters and the equations to be solved together with the desired bias conditions. For a better understanding of the representation of three-dimensional laser simulation in the command file, a brief background is given here.

The software implementation of DESSIS follows an object-oriented approach [38]. All properties of a laser and its state are contained in the class

---

<sup>13</sup>Further details can be found in the manual of *Noffset3D* [115]. The embedding of a tensor grid in a global Delaunay mesh is also discussed in [116].

Device. These include the geometry of the device and its material composition as well as properties relevant to the actual simulation such as mesh information, material and physical model parameters, and equations to be solved. In the conceptually simplest simulation, a single instance of the class `Device` is created. Due to the original design goals of DESSIS,<sup>14</sup> it is also possible to connect multiple devices of different dimensionality—each with its own mesh and other distinct information—in a SPICE-like circuit. Recently, this feature has been exploited to perform dual-grid simulations of optoelectronic devices, where electrothermal problems and optical problems impose different constraints on the discretization of the respective simulation domains [36, 43]. More details on implementation issues can be found in the cited work.

In this thesis, an extension based on the dual-grid approach has been implemented, which reflects the solution strategy of the three-dimensional optical problem described in Chapters 2 and 3. As a minimum requirement, for each structurally unique device cross-section a separate device, an `OpticalSolver Device`, has to be defined—typically no more than five to seven for tunable lasers covered in this work. This is shown in the command file excerpt in App. A. If needed, it is also possible to define one for every transverse cut, allowing for maximum flexibility regarding the mesh and type of two-dimensional optical subsolver to be used. For the longitudinal cavity problem, a one-dimensional `OpticalSolver Device` has to be defined, for which a transfer-matrix solver is chosen per default. The definition of the grating structure along the waveguide, namely, the  $z$ -dependent values for the pair  $(\Delta n', \Delta \alpha)$  are read from an extra input file.

The actual three-dimensional device is defined in a separate section and contains the usual specification of physical models as shown in App. A.<sup>15</sup> In the `System` section, the interconnection of the different `Devices` is laid out. For each transverse cut needed by the three-dimensional optical solver, an instance of the appropriate `OpticalSolver Device` is instantiated by specifying its longitudinal location as an argument. Sometimes, AR or HR coatings need to be included in the simulation. Transverse cuts representing these coatings do not allow for the calculation of optical modes and, therefore, an optional argument can be given, which triggers the copying

---

<sup>14</sup>DESSIS has been designed as a combined silicon device and circuit simulator [38].

<sup>15</sup>Region-dependent molefraction composition can be specified either in the respective physics section in the command file or in the data file corresponding to the simulation grid.

from neighboring cuts.

As a general rule, transverse cuts should be made every  $5\mu\text{m}$  along the device except near active–passive or other structural interfaces where the intercut spacing should be adjusted to smaller values. However, performing a test run of the simulation can yield better information about simulation domains in which crucial quantities such as carrier densities and temperature distribution vary significantly and, hence, require an adequate resolution.

In the remainder of the *System* section, the equations to be solved together with the respective drive currents or voltages are specified. The example excerpt in App. A shows the procedure for creating the tuning map of an SGDBR laser.

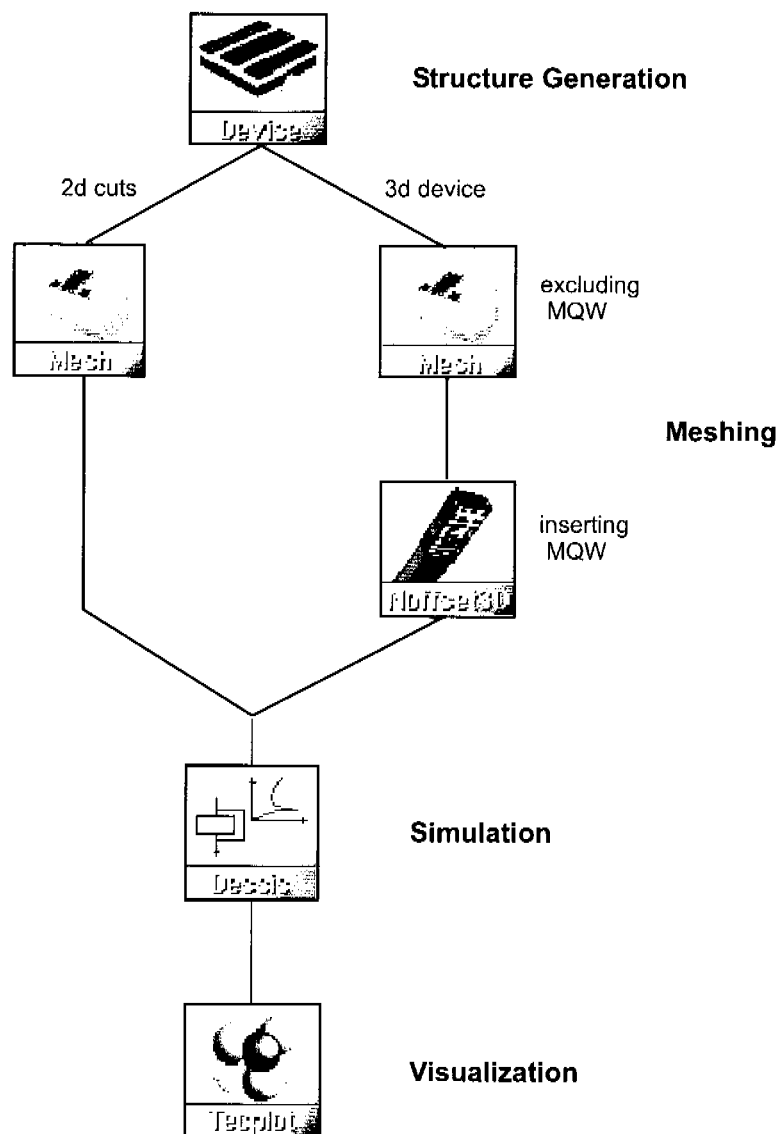


**Figure 4.38:** Tool flow for typical 3D simulation of multisection laser.

Seite Leer /  
Blank leaf



# Chapter 5

## Conclusion and Outlook

### 5.1 Major Achievements

A multidimensional modeling approach to the simulation of complex wavelength-tunable semiconductor lasers has been presented. With the implementation of an efficient optical mode solver based on a parametric separation ansatz, it has been possible, for the first time, to perform simulations of multisection devices in full three dimensions, where the electrothermal and optical problem are coupled self-consistently. The latter is indispensable if the physics underlying the tuning behavior is to be captured accurately. Moreover, for certain types of tunable lasers exhibiting large mode jumps, a modified Gummel-type iteration scheme has been introduced to overcome numerical oscillations related to these critical operating points.

In view of the challenging computational task, several performance enhancements, such as parallelization, iterative solver tuning and optical resonance tracking, have been made to bring three-dimensional simulation of realistic tunable laser structures into the scope of device engineers. In contrast to standard one-dimensional and two-dimensional simulations, structure and mesh generation in three dimensions can be an ambitious task in itself. This thesis addresses the necessary steps to set up a successful simulation.

To demonstrate the capabilities of the simulator, three types of tunable laser, all different in device structure and geometry, and tuning behavior, have been investigated in more detail. The simulation results are shown

to be in good agreement with experimental data. In particular, the simulated tuning maps of a sampled-grating DBR laser—representing the new generation of widely tunable lasers—prove the robustness and power of the simulator presented in this work. Besides comparing the respective terminal characteristics, it is possible to virtually *look inside* the device to analyze, for example, the local temperature distribution or spatial hole-burning effects. This has the potential of giving device designers the competitive edge.

## 5.2 Further Opportunities and Outlook

In this thesis the foundation for the robust and efficient simulation of multisection tunable lasers in full three dimensions has been presented and its potential for device design and optimization has been demonstrated. As the presented framework is compatible with other recent developments in the Computational Optoelectronics Group, it is possible to advance  $k \cdot p$  band structure and manybody gain calculation. Furthermore, the possible inclusion of dynamic and noise properties would allow for a comprehensive calibration effort. In any application, the influence of temperature effects on the tuning behavior is of practical importance. This simulator offers the unique opportunity of realistically studying thermal cross-talk effects.

It was shown that a wide range of tunable lasers is covered by the underlying physical models. Since most of the latest widely tunable lasers rely on an integrated and sometimes tapered semiconductor optical amplifier to reach the required levels of light output power, it would be desirable to simulate the whole device, helping to understand possible feedback effects. Hence, an important extension for the future is the incorporation of a rigorous treatment of amplified spontaneous emission in the current simulator.

As the monolithic integration of further functions such as Mach–Zehnder interferometers or electro-absorption modulators continues, feeding an equivalent optical circuit simulator with data from physics-based 3D simulation could be a successful approach—linking the accuracy of a 3D model with the efficiency and flexibility of a circuit model.

# Appendix A

## Command File Excerpts

### Example of 3D SGDBR Laser Simulation

```
#####
# Specify linear solver:
#####
Math {
    ...
    Method = blocked
    #if extended 2D
    Submethod=pardiso
    #else if full 3D
    SubMethod=ils
    #end
    ...
}

#####
# Define 2D optical subsolver devices:
#####

OpticalSolver OptDev0 {
    File {
```

```
        Grid    = "FrontMirrorSection.grd"
        Doping  = "FrontMirrorSection.dat"
    }
}

OpticalSolver OptDev1 {
    File {
        Grid    = "Channel_FrontMirror_Gain.grd"
        Doping  = "Channel_FrontMirror_Gain.dat"
    }
}

OpticalSolver OptDev2 {
    File {
        Grid    = "GainSection.grd"
        Doping  = "GainSection.dat"
    }
}

OpticalSolver OptDev3 {
    File {
        Grid    = "Channel_Gain_Phase.grd"
        Doping  = "Channel_Gain_Phase.dat"
    }
}

OpticalSolver OptDev4 {
    File {
        Grid    = "PhaseSection.grd"
        Doping  = "PhaseSection.dat"
    }
}

OpticalSolver OptDev5 {
    File {
        Grid    = "Channel_Phase_RearMirror.grd"
        Doping  = "Channel_Phase_RearMirror.dat"
    }
}
```

```

}

OpticalSolver OptDev6 {
  File {
    Grid    = "RearMirrorSection.grd"
    Doping  = "RearMirrorSection.dat"
  }
}

OpticalSolver OptDevTMM {
  File {
    Grid =    "1D.grd"
    Doping = "1D.dat"
  }
}

#####
# Define 3D device:
#####

Device LaserDiode {

  Electrode {
    { Name = "GainContact"           Voltage = 0.0 }
    { Name = "FrontMirrorContact" Voltage = 0.0 }
    { Name = "PhaseContact"          Voltage = 0.0 }
    { Name = "RearMirrorContact"      Voltage = 0.0 }
    { Name = "n-Contact"              Voltage = 0.0 }
  }

  File {
    Grid          = "3D.grd"
    Doping         = "3D.dat"
    Parameters    = "3D.par"
    ...
  }

  Physics {

```

```

...
Laser (
  Optics (
    FEScalar (
      EquationType          = Waveguide
      Symmetry              = Symmetric
      TargetEffectiveIndex  = 3.5
      TargetLoss            = 0.0
      Polarization          = TE
      LasingWavelength     = 1550
    )
  )
  ...
)
}
}

System {
  LaserDiode d1 (
    "GainContact"= vdd
    "FrontMirrorContact"= fm
    "RearMirrorContact"= rm
    "PhaseContact"= ph
    "n-Contact"= gnd
  ){
    Physics {
      OptSolver = [ "Lumi0" ... "Lumi25" "TMM" ]
    }
  }
}

Vsource_pset drive(vdd gnd){ dc = 0.0 }
Vsource_pset tune_fm(fm gnd){ dc = 0.0 }
Vsource_pset tune_rm(rm gnd){ dc = 0.0 }
Vsource_pset tune_ph(ph gnd){ dc = 0.0 }
Set ( gnd = 0.0 )

OptDev0 Lumi0 (CutPosition = 0.0)      # Front M.

```

```

...
OptDev0 Lumi5 (CutPosition = 301)      # Front M.
OptDev1 Lumi6 (CutPosition = 305)      # Channel
OptDev2 Lumi7 (CutPosition = 315)      # Gain
...
OptDev2 Lumi12 (CutPosition = 792)     # Gain
OptDev3 Lumi13 (CutPosition = 810)     # Channel
OptDev4 Lumi14 (CutPosition = 815)     # Phase
...
OptDev4 Lumi16 (CutPosition = 875)     # Phase
OptDev5 Lumi17 (CutPosition = 883)     # Channel
OptDev6 Lumi18 (CutPosition = 889)     # Rear M.
...
OptDev6 Lumi25 (CutPosition = 1434.5) # Rear M.
OptDevTMM InPlaneTMM ()
}

```

```

Solve {
  Optics
  Wavelength
  Poisson
  Coupled { Poisson Electron Hole
            QWhScatter QWeScatter
            PhotonRate
  }
}

```

```

#####
# Drive laser to operating point
#####
Quasistationary (
  ...
  Goal { Parameter=drive.dc Value=1.3 }
){
  Plugin {
    Coupled { Electron Hole Poisson
              QWeScatter QWhScatter
              PhotonRate P
              Contact Circuit
    }
  }
}

```

```

    }
    Optics
    Wavelength
  }
}

#####
#  Rear mirror tuning
#####
  Quasistationary (
    ...
    Goal { Parameter=tune_rm.dc Value=1.2 }
  ){
    Plugin {
      Coupled { Electron Hole Poisson
                  QWeScatter QWhScatter
                  PhotonRate
                  Contact Circuit
            }
      Optics
      Wavelength
    }
  }
}

```

## ILS Configuration File

```

set(1) {
  iterative( bicgstab, tolrel=1e-8,
             tolunprec=1e-4, maxit=400 );
  preconditioning( ilut(0.00005,1) );
  ordering( symmetric=nd, nonsymmetric=mpsilst );
  options( compact=yes, verbose=2 );
}

```



# List of Abbreviations

<b>AR</b>	antireflection
<b>BBR</b>	buried blocking region
<b>BH</b>	buried-heterostructure
<b>BiCGStab</b>	biconjugate gradients stabilized method
<b>BPM</b>	beam-propagation method
<b>CPU</b>	central processing unit
<b>CWDM</b>	coarse wavelength-division multiplexing
<b>CW</b>	continuous wave
<b>DBR</b>	distributed Bragg reflector
<b>DFB</b>	distributed feedback
<b>DFM</b>	design-for-manufacturing
<b>DSDBR</b>	digital-supermode distributed Bragg reflector
<b>DS</b>	digital supermode
<b>DWDM</b>	dense wavelength-division multiplexing
<b>ECL</b>	external cavity laser
<b>EEL</b>	edge-emitting laser

<b>EIM</b>	effective index method
<b>ETHZ</b>	Eidgenössische Technische Hochschule Zürich
<b>FEM</b>	finite-element method
<b>FP</b>	Fabry–Perot
<b>FWHM</b>	full-width half-maximum
<b>GCSR</b>	grating-coupled sampled-reflector
<b>HR</b>	high reflection
<b>ILUT</b>	threshold-based incomplete LU factorization
<b>ITU</b>	International Telecommunication Union
<b>JDQZ</b>	Jacobi–Davidson QZ
<b>LASER</b>	light amplification by stimulated emission of radiation
<b>MEMS</b>	micro-electro-mechanical systems
<b>MG–Y</b>	modulated-grating Y-branch
<b>MMI</b>	multimode interference
<b>MPS</b>	maximize product on diagonal with scalings
<b>MQW</b>	multi quantum-well
<b>ND</b>	nested dissection
<b>PBH</b>	planar buried-heterostructure
<b>PDE</b>	partial differential equation
<b>PIC</b>	photonic integrated circuit
<b>PMI</b>	physical model interface
<b>QW</b>	quantum well
<b>RAM</b>	random access memory

<b>ROADM</b>	reconfigurable optical add/drop multiplexer
<b>RW</b>	ridge waveguide
<b>SCH</b>	separate confinement heterostructure
<b>SEM</b>	scanning electron micrograph
<b>SG</b>	sampled grating
<b>SGDBR</b>	sampled-grating distributed Bragg reflector
<b>SHB</b>	spatial hole-burning
<b>SIPBH</b>	semi-insulating planar buried-heterostructure
<b>SMSR</b>	side-mode suppression ratio
<b>SOA</b>	semiconductor optical amplifier
<b>SRH</b>	Shockley–Read–Hall
<b>SSG</b>	superstructure grating
<b>SSGDBR</b>	superstructure-grating distributed Bragg reflector
<b>TCAD</b>	technology computer-aided design
<b>TE</b>	transverse electric
<b>TMM</b>	transfer-matrix method
<b>TM</b>	transverse magnetic
<b>TTG</b>	tunable twin-guide
<b>UCSB</b>	University of California, Santa Barbara
<b>VCSEL</b>	vertical-cavity surface-emitting laser
<b>VMZ</b>	vertically integrated Mach–Zehnder
<b>WDM</b>	wavelength-division multiplexing
<b>WT</b>	wavelength-tunable

Seite Leer /  
Blank leaf

# Bibliography

- [1] F. J. Duarte. *Tunable Lasers Handbook*. Academic Press Inc., 1995.
- [2] I. Moerman, P. P. Van Daele, and P. M. Demeester. A review on fabrication technologies for the monolithic integration of tapers with III-V semiconductor devices. *IEEE Journal of Selected Topics in Quantum Electronics*, 3(6):1308–1320, 1997.
- [3] Y. Kawamura, K. Wakita, Y. Yoshikuni, Y. Itaya, and H. Asahi. Monolithic integration of a DFB laser and an MQW optical modulator in the 1.5  $\mu\text{m}$  wavelength range. *IEEE J. Quantum Electron.*, QE-23(6):915–918, 1987.
- [4] H. Soda, M. Furutsu, K. Sato, N. Okazaki, Y. Yamazaki, H. Nishimoto, and H. Ishikawa. High-power and high-speed semi-insulating BH structure monolithic electroabsorption modulator/DDB laser light source. *Electronic Letters*, 26:9–10, 1990.
- [5] R. Nagarajan and et al. Large-scale photonic integrated circuits. *IEEE Journal of Selected Topics in Quantum Electronics*, 11(1):50–65, 2005.
- [6] Y. Abe, K. Kishino, Y. Suematsu, and S. Arai. GaInAsP/InP integrated laser with butt-jointed built-in distributed-Bragg-reflection waveguide. *Electronics Letters*, 17(25):945–947, 1981.
- [7] Y. Tohmori, Y. Suematsu, H. Tsushima, and S. Arai. Wavelength tuning of GaInAsP-InP integrated laser with butt-jointed built-in distributed Bragg reflector. *Electronics Letters*, 19(17):656–657, 1983.

- [8] L. A. Coldren. Monolithic tunable diode lasers. *IEEE Journal on Selected Topics in Quantum Electronics*, 6(6):988–999, 2000.
- [9] A. Witzig, M. Pfeiffer, V. Laino, L. Schneider, and B. Witzigmann. Device simulation and statistical analysis in industrial laser design. In *Proceedings of SPIE Volume: 5722 Physics and Simulation of Optoelectronic Devices XIII*, 2005.
- [10] J. Buus, M.-C. Amann, and D. Blumenthal. *Tunable Laser Diodes and Related Optical Sources*. John Wiley & Sons, Inc., 2005.
- [11] L. A. Coldren and S. W. Corzine. *Diode Lasers and Photonic Integrated Circuits*. Wiley series in microwave and optical engineering. John Wiley & Sons Inc., New York, 1995.
- [12] M. C. Amann, S. Illek, C. Schanen, and W. Thulke. Tunable twin-guide laser: A novel laser diode with improved tuning performance. *Appl. Phys. Lett.*, 54:2532–2533, 1989.
- [13] B. Schmidt, S. Illek, R. Gessner, and M. C. Amann. Design and realization of a buried-heterostructure tunable-twin-guide laser diode with electrical blocking regions. *IEEE J. Quantum Electron.*, 35:794–802, 1999.
- [14] R. Todt, R. Jacke, T. and Meyer, and M.-C. Amann. High output power tunable twin-guide laser diodes with improved lateral current injection structure. *Electronics Letters*, 41(4):190 – 191, 2005.
- [15] R. Todt, T. Jacke, R. Meyer, R. Laroy, G. Morthier, and M.-C. Amann. Wide wavelength tuning of sampled grating tunable twin-guide laser diodes tod, r.; jacke, t.; meyer, r.; laroy, r.; morthier, g.; amann, m.-c.; electronics letters volume 40, issue 23, 11 nov. 2004 page(s):1491 - 1493. *Electronics Letters*, 40(23):1491 – 1493, 2004.
- [16] B. Borchert, S. Illek, T. Wolf, J. Rieger, and M.-C. Amann. Vertically integrated Mach-Zehnder interferometer (VMZI) widely tunable laser diode with improved wavelength access. *Eelectronics Letters*, 30(24):2047–2049, 1994.
- [17] T. Jacke, R. Todt, M. Rahim, and M.-C. Amann. Widely tunable Mach-Zehnder interferometer laser with improved tuning efficiency. *Electronics Letters*, 41(5):253 – 254, 2005.

- [18] T. L. Koch, U. Koren, and B. I. Miller. High performance tunable  $1.5\mu\text{m}$  InGaAs/InGaAsP multiple quantum-well distributed Bragg reflector lasers. *Applied Physics Letters*, 53(12):1036–1038, 1988.
- [19] L. A. Coldren, G. A. Fish, Y. Akulova, J. S. Barton, L. Johansson, and C. W. Coldren. Tunable semiconductor lasers: A tutorial. *Journal of Lightwave Technology*, 22(1):193–202, 2004.
- [20] V. Jayaraman, A. Mathur, L. A. Coldren, and P. D. Dapkus. Extended tuning range in sampled grating DBR lasers. *IEEE Photonics Technology Letters*, 5(5):489–491, 1993.
- [21] B. Mason, J. Barton, G. A. Fish, and L. A. Coldren. Design of sampled grating DBR lasers with integrated semiconductor optical amplifiers. *IEEE Photonics Technology Letters*, 12(7):762–764, 2000.
- [22] A. J. Ward, D. J. Robbins, G. Busico, E. Barton, L. Ponnampalam, J. P. Duck, N. D. Whitbread, P. J. Williams, D. C. J. Reid, A. C. Carter, and M. J. Wale. Widely tunable DS-DBR laser with monolithically integrated SOA: Design and performance. *IEEE Journal of Selected Topics in Quantum Electronics*, 11(1):149:156, 2005.
- [23] Y. Tohmori, Y. Yoshikuni, H. Ishii, F. Kano, T. Tamamura, Y. Kondo, and M. Yamamoto. Broad-range wavelength-tunable superstructure grating (SSG) DBR lasers. *IEEE J. Quantum Electron.*, 29(6):1817–1823, 1993.
- [24] H. Ishii, Y. Tohmori, Y. Yoshikuni, T. Tamamura, and Y. Kondo. Multiple-phase-shift super structure grating DBR lasers for broad wavelength tuning lasers. *IEEE Photonics Technology Letters*, 5(6):613–615, 1993.
- [25] A. J. Ward, D. J. Robbins, G. Busico, N. D. Whitbread, P. J. Williams, D. C. J. Reid, and J. R. Rawsthorne. Modelling of phase-grating based wideband tuneable lasers with simplified quasi-digital wavelength selection. In *IEE Proceedings, Part J*, volume 150, pages 199–204, 2003.
- [26] M. Oberg, S. Nilsson, J. Streubel, K. Wallin, L. Backbom, and T. Klinga. 74 nm wavelength tuning range of an InGaAsP/InP vertical

- grating assisted codirectional coupler laser with rear sampled grating reflector. *IEEE Photonics Technology Letters*, 5(7):735–738, 1993.
- [27] P.-J. Rigole, S. Nilsson, S. Bäckbom, L. Klinga, J. Wallin, J. Stalnacke, B. E. Berglind, and B. Stoltz. 114 nm wavelength tuning range of a vertical grating assisted codirectional coupler laser with a super structure grating distributed bragg reflector. *IEEE Photonics Technology Letters*, 7(7):697–699, 1995.
- [28] Y. Gustafsson, S. Hammerfeldt, J. Hammersberg, M. Hassler, T. Horman, M. Isaksson, J. Karlsson, D.E. Larsson, O.D. Larsson, L. Lundqvist, T. Lundstrom, M. Rask, E. Rigole, P.-J. and; Runeland, A. Saavedra, G. Sarlet, R. Siljan, P. Szabo, L. Tjernlund, O. Traskman, H. de Vries, J.-O. Wesstrom, and C. Ogren. Record output power (25 mW) across C-band from widely tunable GCSR lasers without additional SOA. *Electronics Letters*, 39(3):292–293, 2003.
- [29] M. Chacinski, M. Isaksson, and R. Schatz. High-speed direct modulation of widely tunable MG-Y laser. *IEEE Photonics Technology Letters*, 17(6):1157–1159, 2005.
- [30] L. B. Soldano and E. C. M. Pennings. Optical multi-mode interference devices based on self-imaging: principles and applications. *Journal of Lightwave Technology*, 13(4):615–627, 1995.
- [31] C. J. Chang-Hasnain. Tunable VCSELs. *IEEE Journal on Selected Topics in Quantum Electronics*, 6(6):978–987, 2000.
- [32] P. Vankwikelberge, G. Morthier, and R. Baets. CLADISS-a longitudinal multimode model for the analysis of the static, dynamic, and stochastic behavior of diode lasers with distributed feedback. *IEEE J. Quantum Electron.*, 26(10):1728–1741, 1990.
- [33] G. Sarlet, G. Morthier, and R. Baets. Control of widely tunable SSG-DBR lasers for dense wavelength division multiplexing. *Journal of Lightwave Technology*, 18(8):1128–1138, 2000.
- [34] O. A. Lavrova and D. J. Blumenthal. Detailed transfer matrix method-based dynamic model for multisection widely tunable GCSR lasers. *Journal of Lightwave Technology*, 18(9):1274–1283, 2000.



- [35] J. Vuckovic and Y. Yamamoto. Photonic crystal microcavities for cavity quantum electrodynamics with a single quantum dot. *Appl. Phys. Lett.*, 82(15):2374–2376, 2003.
- [36] M. Pfeiffer. *Insutrial-Strength Simulation of Quantum-Well Semiconductor Lasers*. PhD thesis, Eidgenössisch Technische Hochschule (ETH) Zürich, Switzerland, 2004.
- [37] Synopsys Inc. (Former ISE Integrated Systems Engineering AG). 700 East Middlefield Road, Mountain View, CA 94043, USA.
- [38] S. Müller. *An object-oriented approach to multidimensional semiconductor device simulation*. PhD thesis, Eidgenössisch Technische Hochschule (ETH) Zürich, Switzerland, 1994.
- [39] K. Kells. *General Electrothermal Semiconductor Device Simulation*. PhD thesis, Eidgenössisch Technische Hochschule (ETH) Zürich, Switzerland, 1994.
- [40] B. Witzigmann. *Efficient Simulation of Quantum-Well Lasers*. PhD thesis, Eidgenössisch Technische Hochschule (ETH) Zürich, Switzerland, 2000.
- [41] B. Witzigmann, A. Witzig, and W. Fichtner. A multidimensional laser simulator for edge-emitters including quantum carrier capture. *IEEE Trans. ED*, 47:1926–1934, 2000.
- [42] M. Streiff, A. Witzig, M. Pfeiffer, P. Royo, and W. Fichtner. A comprehensive VCSEL device simulator. *IEEE Journal of Selected Topics in Quantum Eelectronics*, 9(3):879–891, 2003.
- [43] M. Streiff. *Opto-Electro-Thermal VCSEL Device Simulation*. PhD thesis, Eidgenössisch Technische Hochschule (ETH) Zürich, Switzerland, 2004.
- [44] G. Wachutka. An extended thermodynamic model for the simultaneous simulation of the thermal and electrical behavior of semiconductor devices. In *Proceedings of the Sixth International NASECODE Conference*, pages 409–414. Boole Press Ltd., 1989.
- [45] B. Witzigmann, A. Witzig, and A. Fichtner. A full 3-dimensional quantum-well laser simulation. In *Proceedings of LEOS*, 2000.

- [46] D. Schroeder. *Modelling of Interface Carrier Transport for Device Simulation*. Springer, Vienna, 1994.
- [47] G. Baraff. Semiclassical description of electron transport in semiconductor quantum-well devices. *Phys. Rev. B*, 55:10745–10753, Apr. 1997.
- [48] M. Hybertsen, M. Alam, G. Baraff, A. A. Grinberg, and R. Smith. Role of nonequilibrium carrier distributions in multi-quantum well InGaAsP based lasers. In *SPIE Proceedings Physics and Simulation of Optoelectronic Devices VI*, San Jose, California, 1998.
- [49] R. E. Bank, D. J. Rose, and W. Fichtner. Numerical methods for semiconductor device simulation. *IEEE Trans. Elec. Dev.*, 30(9):1031–1041, 1983.
- [50] G. Baraff and R. Smith. Nonadiabatic semiconductor laser rate equations for the large-signal, rapid-modulation response regime. *Phys. Rev. A*, 61:1–13, 2000.
- [51] X. Li, A. D. Sadovnikov, W.-P. Huang, and T. Makino. A physics-based three-dimensional model for distributed feedback laser diodes. *IEEE Journal of Quantum Electronics*, 34(9):1545–1553, September 1998.
- [52] S. L. Chuang. *Physics of Optoelectronic Devices*. John Wiley & Sons Inc., New York, 1995.
- [53] M. Luisier and S. Odermatt. Many-body effects in semiconductor lasers and carrier transport in quantum structures. Master's thesis, ETH Zürich, 2003.
- [54] R. Courant and D. Hilbert. *Methods of Mathematical Physics*, volume 2. Interscience Publishers, New York, 1962.
- [55] D. Marcuse. *Light Transmission Optics*. Robert E. Krieger Publishing Company, second edition edition, 1989.
- [56] D. Marcuse. *Theory of Dielectric Optical Waveguides*. Academic Press, 1974.

- [57] A Sommerfeld. *Partial Differential Equations in Physics*. Academic Press, 1949.
- [58] J. D. Jackson. *Classical Electrodynamics*. John Wiley & Sons, Inc., New York, second. edition, 1975.
- [59] C. H. Henry, R. A. Logan, and K. A. Bertness. Spectral dependence of the change in refractive index due to carrier injection in GaAs lasers. *Journal of Applied Physics*, 52:4457–4461, 1981.
- [60] B. R. Bennett, R. A. Soref, and J. A. Del Alamo. Carrier-induced change in refractive index of InP, GaAs, and InGaAsP. *IEEE J. Quantum Electron.*, 26:113–122, 1990.
- [61] J.-P. Weber. Optimization of the carrier-induced effective index change in InGaAsP waveguides - application to tunable Bragg filters. *IEEE J. Quantum Electron.*, 30(8):1801–1816, 1994.
- [62] S. Adachi. Material paramters of  $\text{In}_{1-x}\text{Ga}_x\text{As}_y\text{P}_{1-y}$  and related binaries. *J. Appl. Phys.*, 53(12):8775–8792, 1982.
- [63] P. Chandra, L. A. Coldren, and K. E. Strege. Refractive index data from  $\text{Ga}_x\text{In}_{1-x}\text{As}_y\text{P}_{1-y}$  films. *Electronics Letters*, 17(1):6–7, 1981.
- [64] B. Mason, G. A. Fish, S. Denbaars, and L.A. Coldren. Widely tunable sampled grating DBR laser with integrated electro-absorption modulator. *IEEE Photonics Technology Letters*, 11(6):638–640, 1999.
- [65] T. L. Koch, U. Koren, G. Eisenstein, M. G. Young, M. Oron, C. R. Giles, and B. I. Miller. Tapered waveguide InGaAs/InGaAsP multiple-quantum-well lasers. *IEEE Photonics Technology Letters*, 2(2):88–90, 1990.
- [66] M. Chien, U. Koren, B. I. Miller, M. Oron, M. G. Young, and J. L. Demiguel. Short-cavity distributed Bragg reflector laser with an integrated tapered output waveguide. *IEEE Photonics Technology Letters*, 3(5):418–420, 1991.
- [67] B. Witzigmann, A. Bregy, F. Michel, S. Odermatt, R. Santschi, and M. Streiff. A full three-dimensional microscopic simulation for vertical-cavity surface-emitting lasers. In *Proceedings of NUSOD*, 2005.

- [68] H. Shao. *Numerical Analysis of Meshing and Discretization for Anisotropic Convection-Diffusion Equations with Applications*. PhD thesis, Duke University, 1999.
- [69] M. A. Yerry and M. S. Shephard. A modified quadtree approach to finite element mesh generation. *IEEE Computer Graphics And Applications*, 3(1):39–46, 1983.
- [70] B. Schmithüsen. *Grid Adaptation for the Stationary Two-Dimensional Drift-Diffusion Model in Semiconductor Device Simulation*. PhD thesis, Eidgenössisch Technische Hochschule (ETH) Zürich, Switzerland, 2002.
- [71] Synopsys Inc. (Former ISE Integrated Systems Engineering AG), *Dessis Manual, ISE TCAD Release 10.0, 2004*.
- [72] D. L. Scharfetter and H. K. Gummel. Large-signal analysis of a silicon Read diode oscillator. *IEEE Trans. Elec. Dev.*, 16:64–77, 1969.
- [73] T.-W. Tang. Extension of the Scharfetter-Gummel algorithm to the energy-balance equation. *IEEE Trans. Elec. Dev.*, 31(12):1912–1914, 1984.
- [74] R. E. Bank, W. M. Coughran, W. Fichtner, E. H. Grosse, D. J. Rose, and R. K. Smith. Transient simulation of silicon devices and circuits. *IEEE Trans. Elec. Dev.*, 32(10):1992–2007, 1985.
- [75] R. E. Bank and D. J. Rose. Global approximate Newton methods. *Numerische Mathematik*, 37:279–295, 1981.
- [76] O. Schenk. *Scalable Parallel Sparse LU Factorization Methods on Shared Memory Multiprocessors*. Ph.D. dissertation, Eidgenössische Technische Hochschule Zürich, Zurich, Switzerland, 2000.
- [77] O. Schenk and K. Gärtner. Solving unsymmetric sparse systems of linear equations with PARDISO. *Journal of Future Generation Computer Systems*, 20(3):475–487, 2004.
- [78] S. K. Rölli. *Parallel iterative solvers in computational electronics*. PhD thesis, Eidgenössisch Technische Hochschule (ETH) Zürich, Switzerland, 2005.

- [79] A. Witzig. *Modeling the Optical Processes in Semiconductor Lasers*. PhD thesis, Eidgenössisch Technische Hochschule (ETH) Zürich, Switzerland, 2002.
- [80] J. Jin. *The Finite-Element Method in Electromagnetics*. Wiley, 1993.
- [81] D. R. Fokkema, G. L. Sleijpen, and H. A. van der Vorst. Jacobi-Davidson style QR and QZ algorithms for the reduction of matrix pencils. *SIAM J. Sci. Comput.*, 20(1):94–125, 1998.
- [82] M. Streiff, A. Witzig, and W. Fichtner. Computing optical modes for VCSEL device simulation. *IEE Proceedings Optoelectronics*, 149(4):166–173, 2002.
- [83] A. Yariv and Pochi Yeh. *Optical Waves in Crystals*. John Wiley & Sons Inc., 1984.
- [84] G. P. Agrawal and N. K. Dutta. *Long-Wavelength Semiconductor Lasers*. Van Nostrand Reinhold, 1986.
- [85] V. Jayaraman, Z.-M. Chuang, and L. A. Coldren. Theory, design and performance of extended tuning range semiconductor laser with sampled gratings. *IEEE J. Quantum Electron.*, 29(6):1824–1834, 1993.
- [86] H. Kogelnik and C. V. Shank. Coupled-wave theory of distributed feedback lasers. *J. Appl. Phys.*, 43(5):2327–2335, 1972.
- [87] M. Yamada and K. Sakuda. Analysis of almost-periodic distributed feedback lasers. *Applied Optics*, 26:3474–3478, 1987.
- [88] J. A. Nelder and R. Mead. A simplex method for function minimization. *Computer Journal*, 7:308–313, 1965.
- [89] C. H. Henry and R. F. Kazarinov. Quantum noise in photonics. *Reviews of Modern Physics*, 68(3):801–853, July 1996.
- [90] H. K. Gummel. A self-consistent iterative scheme for 1-dimensional steady state transistor calculations. *IEEE Trans. Elec. Dev.*, 11(10):455, 1964.
- [91] S. Murata, I. Mito, and K. Kobayashi. Over 720GHz (5.8nm) frequency tuning by a  $1.5\mu\text{m}$  DBR laser with phase and Bragg wavelength control regions. *Electronics Letters*, 23(8):403–405, 1987.

- [92] S. Odermatt, B. Schmithüsen, and B. Witzigmann. Comprehensive physics-based intensity noise simulation of VCSELs. In *Proceedings of NUSOD*, pages 57–58, 2004.
- [93] V. Laino, M. Pfeiffer, A. Witzig, and W.; Fichtner. A tcad calibration methodology. In *Proceedings of NUSOD*, 2003.
- [94] B. Schmidt. *Leistungsoptimierung abstimmbarer InGaAsP/InP Halbleiterlaser*. PhD thesis, Walter Schottky Institut, Technische Universität München, 1999.
- [95] B. Schmidt, S. Illek, B. Borchert, J. Rieger, and M. C. Amann. Tunable-twin-guide laser diode with high output efficiency fabricated by an improved reactive ion etching technique. *Semicond. Sci. Technol.*, 13:821–825, 1998.
- [96] W. M. Steffens, M. Nöding, S. Illek, J. Borchert, and M. C. Amann. Tuning dependent beam characteristics of continuously tunable laser diodes. *IEEE Electronics Letters*, 35:1102–1103, 1999.
- [97] S. Neber and M. C. Amann. Tunable laser diodes with type II superlattice in the tuning region. *Semiconductor Sci. Technol.*, 13:801–805, 1998.
- [98] S. Murata, I. Mito, and K. Kobayashi. Tuning ranges for  $1.5\mu\text{m}$  wavelength tunable DBR lasers. *Electronics Letters*, 24(10):577–579, 1988.
- [99] T. L. Koch, U. Koren, R. P. Gnall, C. A. Burrus, and B. I. Miller. Continuously tunable  $1.5\mu\text{m}$  multiple-quantum-well GaInAs/GaInAsP Distributed-Bragg-Reflector lasers. *Electronic Letters*, 24(23):1431–1433, 1988.
- [100] Y. Kotaki, M. Matsuda, H. Ishikawa, and H. Imai. Tunable DBR laser with wide tuning range. *Electronics Letters*, 24(8):503–505, 1988.
- [101] U. Koren, B. I. Miller, G. Eisenstein, R. S. Tucker, g. Raybon, and R. J. Capik. Semi-insulating blocked planar BH InGaAsP/InP laser with high power and high modulation bandwidth. *Electronic Letters*, 24(3):138–140, 1988.

- [102] J. Krause. *On boundary conforming anisotropic Delaunay meshes*. PhD thesis, Eidgenössisch Technische Hochschule (ETH) Zürich, Switzerland, 2001.
- [103] J. Piprek, P. Abraham, and J. E. Bowers. Self-consistent analysis of high-temperature effects on strained-layer multi-quantum-well InGaAsP InP lasers. *IEEE J. Quantum Electron.*, 36(3):366–374, 2000.
- [104] U. Bandelow, R. Huenlich, and T. Koprucki. Simulation of static and dynamic properties of edge-emitting multi quantum well lasers. *IEEE Journal of Selected Topics in Quantum Electronics*, 9:798–806, 2003.
- [105] M. Streiff, W. Fichtner, and A. Witzig. "Vertical-Cavity Surface Emitting Lasers: Single Mode Control and Self Heating Effects" , Chapter 8 in: *Optoelectronic Devices - Advanced Simulation and Analysis*. Springer Verlag, New York, 2004.
- [106] V. Laino, B. Witzigmann, M. Luisier, and M. Pfeiffer. TCAD simulation of optical far-field for an edge emitting semiconductor laser. In *Proceedings of NUSOD*, 2004.
- [107] P. Kozodoy, T. Strand, Y. Akulova, G. Fish, C. Schow, P. Koh, and B. Bian. Thermal effects in monolithically integrated tunable laser transmitters. In *Proceedings of 20th IEEE SEMI-THERM Symposium*, 2004.
- [108] M. N. Sysak, J. S. Barton, L. A. Johansson, J. W. Raring, E. J. Skogen, D. J. Masanovic, M. L. and Blumenthal, and L. A. Coldren. Single-chip wavelength conversion using a photocurrent-driven EAM integrated with a widely tunable sampled-grating DBR laser. *IEEE Photonics Technology Letters*, 16(9):2093–2095, 2004.
- [109] J. Piprek. *Semiconductor Optoelectronic Devices, Introduction to Physics and Simulation*. Academic Press, 2003.
- [110] H. Ishii. Mode stabilization method for superstructure-grating DBR lasers. *Journal of Lightwave Technology*, 16(3):433–442, 1998.
- [111] K. J. Ebeling and L. A. Coldren. Wavelength self stabilization of coupled-cavity semiconductor-lasers. *Electronics Letters*, 20(2):69–70, 1984.

- [112] G. Sarlet, G. Morthier, R. Baets, D. J. Robbins, and D. C. J. Reid. Optimisation of multiple exposure gratings for widely tunable lasers. *IEEE Photonics Technology Letters*, 11(1):21–23, 1999.
- [113] Synopsys Inc. (Former ISE Integrated Systems Engineering AG), *Devise Manual, ISE TCAD Release 10.0, 2004*.
- [114] S. Selberherr. *Analysis and Simulation of Semiconductor Devices*. Springer, Vienna, 1984.
- [115] Synopsys Inc. (Former ISE Integrated Systems Engineering AG), *Noffset3D Manual, ISE TCAD Release 10.0, 2004*.
- [116] F. O. Heinz. *Simulation Approaches for Nanoscale Semiconductor Devices*. PhD thesis, Eidgenössisch Technische Hochschule (ETH) Zürich, Switzerland, 2004.



# Curriculum Vitæ

Lutz Schneider was born in Konstanz, Germany, in 1974. He received his Masters Degree in Theoretical Physics at the Swiss Federal Institute of Technology (ETH), Zürich, in 2001. His diploma thesis on photonic-crystal lasers was carried out in the Computational Quantum Optoelectronics Group at NASA Ames Research Center, California, USA. During his studies, he spent one year (1997/98) at the University of Edinburgh, Scotland, as part of a student exchange program. From 1998 to 1999, he worked in the Theoretical Methods Group at the ABB Corporate Research Center, Baden-Dättwil, Switzerland, first as a trainee and later as a part-time employee. His work at ABB focused on the simulation of high-temperature superconductors. In 2001, he joined the Optoelectronics Modeling Group at the Integrated Systems Laboratory as a research and teaching assistant. He spent three months at the University of California, Santa Barbara, as a visiting researcher in 2003. His main research interests are in the field of numerical modeling and simulation of semiconductor optoelectronic devices.